THE COMPLEX DIELECTRIC PROPERTIES OF AQUEOUS AMMONIA FROM 2GHZ – 8.5GHZ IN SUPPORT OF THE NASA JUNO MISSION

A Master's Thesis
Presented to
The Faculty of the Division of Graduate Studies

By

Danny Duong
Advisor Dr. Paul Steffes

In Partial Fulfillment
of the Requirements for the Degree of
Master of Science in Electrical and Computer Engineering

Georgia Institute of Technology
December 2011

THE COMPLEX DIELECTRIC PROPERTIES OF AQUEOUS AMMONIA FROM 2GHZ – 8.5GHZ IN SUPPORT OF THE NASA JUNO MISSION

Approved by:

Professor Paul G. Steffes, Advisor
School of Electrical and Computer Engineering
Georgia Institute of Technology

Professor Andrew F. Peterson
School of Electrical and Computer Engineering
Georgia Institute of Technology

Professor Waymond R. Scott
School of Electrical and Computer Engineering
Georgia Institute of Technology

Date Approved: 11 November 2011

Tưởng nhớ đến
Ba, Dương Cao Triều
với cho
Mẹ, Dương Lê Sương

Acknowledgments

This work would not be possible without the guidance and support of a number of people to whom I am indebted to. I would like to first thank my advisor, Dr. Paul Steffes, whose great wealth of knowledge, constant support, and immense patience motivated me to complete this work. Very understanding of my own personal and academic issues, he allowed me the personal time when I needed it and, more importantly, the gentle pressure when necessary. Though electromagnetism, planetary remote sensing, and laboratory research are not fields I would have seen myself working with during my years as an undergraduate, Dr. Steffes, eased me into it in a way I feel allowed me to grow to enjoy it. I would also like to thank my thesis committee members Dr. Andrew F. Peterson and Dr. Waymond R. Scott, as well as Dr. Gregory D. Durgin, for providing me with their knowledge, resources, and time and effort in carefully reviewing my thesis work.

Within the lab I would like to thank Sahand Noorizadeh for introducing me to Dr. Steffes and his efforts on the MATLAB® code used for this work. Also I would like to thank Kiruthika Devaraj. She is one of the hardest workers I have had the pleasure of knowing, and seeing her dedication to her work and this lab was enough to inspire any graduate student – or scare them away in terms of work load! Congratulations on your

Ph.D., marriage, and new postdoctoral position; I wish you good luck on all of your future endeavors.

I would also like to thank the Juno mission who provided financial support for my experiments through the NASA Contract NNM06AA75C from the Marshall Space Flight Center supporting the Juno Science Team, under Subcontract 699054X from the Southwest Research Institute.

Lastly I would like to thank my friends and family, but I would like to thank my mother and father in particular. Ba – you taught me the importance of hard work, perseverance, temperance, and patience; I continue to strive to be the man you were. Mẹ – with the loss of Ba nothing has been easy, yet your support and motherly love has always helped me pull through. Cảm ơn Ba; con nhớ Ba nhiều. Cảm ơn Mẹ; con thương Mẹ nhiều.

Contents

List of Tables

List of Figures

List of Abbreviations

DI Water	Deionized water
Epsilon prime	Real component of the complex dielectric constant
Epsilon double prime	Imaginary component of the complex dielectric constant
Georgia Tech	Georgia Institute of Technology in Atlanta, GA
H_2O	Water
MUT	Material under test
NASA	National Aeronautics and Space Administration
NH_3	Ammonia
NH_4OH	Aqueous ammonia (ammonium hydroxide)
PAL	Planetary Atmospheres Laboratory at Georgia Tech
PTFE	Polytetrafluoroethylene, i.e., Teflon
RTM	Radiative transfer model
VNA	Vector network analyzer
ε'	See Epsilon prime
ε"	See Epsilon double prime

Summary

A new model for the complex dielectric constant, ε, of aqueous ammonia (NH_4OH) has been developed based on laboratory measurements in the frequency range between 2-8.5 GHz for ammonia concentrations of 0-8.5 $\%NH_3$/volume and temperatures between 277-297 K. The new model has been validated for temperatures up to 313 K, but may be consistently extrapolated up to 475 K and ammonia concentrations up to 20 $\%NH_3$/volume. The model fits 60.26 % of all laboratory measurements within 2σ uncertainty. The new model is identical to the Meissner and Wentz (2004) model of the complex dielectric constant of pure water, but it contains a correction for dissolved ammonia. A description of the experimental setups, uncertainties associated with the laboratory measurements, the model fitting process, the new model, and its application to approximating jovian cloud opacity for NASA's Juno mission to Jupiter are provided.

Chapter I

Introduction

The human nature is inquisitive and pioneering. With the advent of technology, it has become easier to learn and discover more about the world and those beyond. Microwave remote sensing is a tool that relates to our nature; it allows us to explore our world, our solar system, and even beyond. It is important to continually improve our technology, refine our knowledge of the planets and their processes, and thus continually learn about our origins and significance on a scale larger than ourselves. The NASA Juno mission to Jupiter will allow us to continue the quest for knowledge outside of our world by enabling us to look at Jupiter with unprecedented levels of detail. From this we can refine our jovian planetary model, answer and raise more questions on the origin of Jupiter, and thus continually learn more about our own origins.

1.1 Background and Motivation

First observed by Galileo Galilei in the 1610 (Stillman 1978), Jupiter is the largest planet in the solar system, yet in over 400 years much is still undiscovered about Jupiter. Ground based microwave remote sensing of Jupiter is largely inhibited by the synchrotron radiation belts around Jupiter, and although seven space probes have visited Jupiter, only the Galileo orbital probe has gone into orbit around the planet. What is known are approximate abundances of many constituents: hydrogen and helium with traces of methane, water vapor, ammonia, and other trace constituents; however,

the different models of the formation of Jupiter are dependent on knowing its composition with great accuracy (see e.g., Pollack *et al.*, 1996, for the core accretion model or Boss, 1992, 2002, for gravitational instability model).

One of the constituents which may have a key role in the microwave spectrum emitted from the jovian atmosphere is aqueous ammonia, or liquid water mixed with dissolved ammonia. Aqueous ammonia clouds are able to form in particular cloud layers of Jupiter near 10 bars based on current jovian atmospheric models (see e.g., de Pater *et al.* 2005, Karpowicz 2010). In previous radiative transfer models of the microwave emission from jovian atmospheres, for low concentrations of ammonia, the complex dielectric constant was assumed to be approximately that of water (see e.g., Janssen *et al.* 2005 or de Pater *et al.* 2005) since the ammonia concentration is relatively low. This assumption was made since no model existed for the complex dielectric constant for aqueous ammonia. In this work, a model for the complex dielectric constant of aqueous ammonia (NH_4OH) has been developed based on new laboratory measurements in the frequency range between 2 and 8.5 GHz. This new model is a significant step in better understanding the microwave properties of aqueous ammonia and is useful for characterizing cloud opacity of aqueous ammonia clouds under jovian conditions.

1.2 Organization

The objective of this research is to determine the complex dielectric properties of aqueous ammonia which relate to jovian ammonia cloud opacity at centimeter

wavelengths. These parameters are fit to a new model for cloud opacity that can be implemented in a microwave radiative transfer model (RTM) for Jupiter. It is noted that all instances of ε refer to the *relative* dielectric permittivity, ε_r, both real and imaginary, i.e., $\varepsilon \equiv \varepsilon_r = \varepsilon / \varepsilon_0$; this was done to simplify all equations. The thesis is organized as follows:

Chapter 2 provides an overview of previous research relating to the physical properties of aqueous ammonia. The physical structure of H_2O and NH_3 and their effects on microwave absorptivity are described. The Meissner and Wentz (2004) model for the complex dielectric constant of pure and sea water, which is the basis for this model of the complex dielectric constant of aqueous ammonia, is also described.

Chapter 3 provides a discussion of the theory behind measuring the complex dielectric constant of a liquid. A complete description of the measurement and calibration systems used for this work is presented. A presentation of the raw data collected during experimentation follows.

Chapter 4 begins with a description of the uncertainties involved in the experimental setups used for the laboratory measurements. An explanation of the data correction and calibration algorithms attempted and used follows. Finally the method for fitting the data to a new model and the nature of the new model are presented.

Chapter 5 summarizes the results of this work and presents suggestions for further investigations. An overview of this work's impact on the NASA Juno mission to Jupiter is provided.

Chapter II

Theoretical Basis and Previous Work

The microwave absorption spectra of aqueous ammonia or ammonium hydroxide (NH_3(aq) or NH_4OH) is dependent on the basic molecular properties of water (H_2O) and ammonia (NH_3). Descriptions of the geometric and electro-chemical properties of H_2O and NH_3 are given below. The Meissner and Wentz model of the complex dielectric constant of pure water is central to the new model for the complex dielectric constant of aqueous ammonia, and thus it is described in detail below.

2.1 Physical Structure of H_2O

The geometric structure of the H_2O molecule is such that it is a polar molecule with a permanent dipole moment. A diagram of the structure of an H_2O molecule is shown in Figure 1.

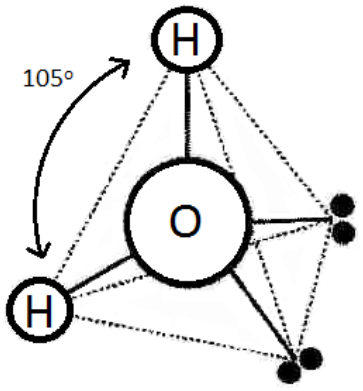

Figure 1. Diagram of the H_2O molecular structure. The black dots represent unbonded electrons.

The water molecule has two bound hydrogen ions (H^+), two pairs of unbonded electron pairs (e^-) in a tetrahedral structure, and an oxygen ion (O^{2+}) in the center. In an ideal tetrahedral molecular structure, the vertices are evenly spaced at 109.5°; however, due to the repulsive forces of the unbonded electron pairs, the hydrogen atoms are only spaced at 105° (King and Smith 1981, Kirkwood 1939). Without the additional unbonded electron pairs, a linear H-O-H structure would not produce a molecule with a permanent dipole moment.

Owing to the polar nature of its molecular structure, the water molecule is influenced by the presence of an electric field and absorbs electromagnetic energy. The liquid water absorption spectrum is shown in Figure 2 (Warren, 1984).

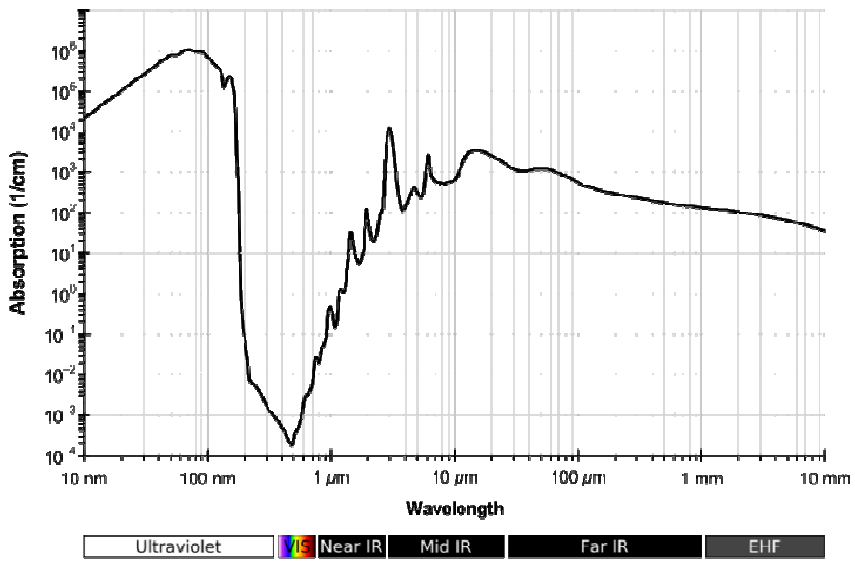

Figure 2. Liquid water absorption spectrum from 10 nm to 10 mm (Warren, 1984).

The absorptivity of liquid water is primarily due to the response of the polar water molecule in an electric field described as Debye relaxation (Debye 1929). When an

electric field is applied to liquid water in a given direction, the polar molecules tend to shift to align parallel to the direction of the electric field. This molecular torque is opposed by the interactions with neighboring molecules in liquid phase, and thus the alignment of the polar water molecules to the electric field does not happen instantaneously. This relaxation time τ_D, which is now known as the Debye relaxation time, is the primary form of interaction between electromagnetic radiation and polar molecules and described by the complex permittivity ε (Gaiduk 1999). This complex dielectric constant ε is frequency dependent and comprised of both a real component ε' and an imaginary component ε" related by

$$\varepsilon(\nu) = \varepsilon'(\nu) - j \cdot \varepsilon''(\nu), \tag{2.1}$$

where $j = \sqrt{-1}$ and ν is the frequency (Hayt and Buck 2006). The term ε" is particularly important concerning electromagnetic energy because it is most associated with energy loss in the dielectric medium.

Finally, electromagnetic radiation loss described by the complex dielectric permittivity, ε, and the intermolecular response of a liquid polar substance to an external electric field described by the Debye relaxation time, τ_D, are related by the Debye formula,

$$\varepsilon = \varepsilon' - j \cdot \varepsilon'' = \varepsilon_\infty + \frac{\varepsilon_s - \varepsilon_\infty}{1 + j \cdot \nu \cdot \tau_D}, \tag{2.2}$$

where $j = \sqrt{-1}$, ν is the frequency, ε_s is the static (zero frequency) dielectric constant, and ε_∞ is the dielectric constant at infinite frequencies (i.e., $\varepsilon_\infty = \lim_{\nu \to \infty} \varepsilon'(\nu)$) (Debye 1929, King and Smith 1981, Gaiduk 1999).

2.2 Physical Structure of NH_3

Like water, ammonia also has a permanent dipole moment due to its geometric molecular shape making ammonia sensitive to electromagnetic energy. The NH_3 molecule consists of three hydrogen ions (H^+), one pair of unbonded electrons (e^-) in a trigonal pyramidal shape, and one nitrogen ion in the center (N^{3-}) (Debye 1929). A schematic of the NH_3 molecule is shown in Figure 3.

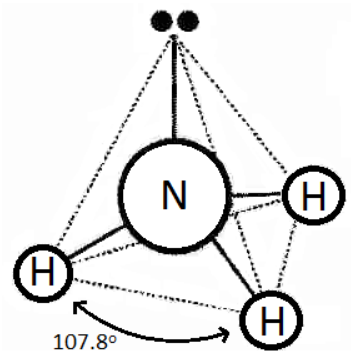

Figure 3. Schematic of the NH_3 molecular structure. The black dots represent unbonded electrons.

Again the unbonded electron pair alters the bond angle from the ideal tetrahedral configuration of 109.5° to 107.8°. The ammonia molecule dissolved in water is also susceptible to electromagnetic radiation because of its dipole moment and Debye relaxation (Debye 1929).

Under normal storage conditions (i.e., closed container, 25 °C) aqueous ammonia solutions are stable in terms of concentration (Ricca Chemical Company 2010). It is noted that when exposed to the ambient conditions, ammonia concentration decreases from uncontained aqueous ammonia solutions due to ammonia evaporation. When considering aqueous ammonia, the concentration and temperature affect the vapor pressure of the solution; increased temperatures decrease the ammonia concentration in solution and increase the vapor pressure, and thus, more ammonia is able to outgas at a faster rate.

2.3 Meissner and Wentz Model

The Meissner and Wentz model for the complex dielectric constant of pure water is used as the basis for the new model for the complex dielectric constant of aqueous ammonia. Meissner and Wentz's model is fit based on laboratory measurements and is valid for temperatures between -20 °C and 40 °C and for frequencies up to 500 GHz for pure water. Their model is also valid for sea water for temperatures between -2 °C and 29 °C and for frequencies up to 90 GHz (Meissner and Wentz 2004).

The Meissner and Wentz model is a modified version of Klein and Swift's model for the dielectric constant of water (Klein and Swift 1977). The Klein and Swift dielectric model fits dielectric constants with a single Debye relaxation law. The Debye formula is the

response of ideal non-interacting polar molecules to an external electric field, as given by equation 2.3.

$$\hat{\varepsilon}(\omega) = \varepsilon_{\infty} + \frac{\varepsilon_s - \varepsilon_{\infty}}{1 + i\omega\tau} \tag{2.3}$$

Here, ε_{∞} is the electric permittivity at the high frequency limit, ε_s is the static electric permittivity at low frequencies, $i = \sqrt{-1}$, ω is the frequency of the field, and τ is the relaxation time in seconds (Debye 1929). The Klein-Swift model for the dielectric constant of sea water at microwave frequencies is presented below (Klein and Swift, 1977):

$$\varepsilon(T,S) = \varepsilon_{\infty} + \frac{\varepsilon_S(T,S) - \varepsilon_{\infty}}{1 + \left(i\frac{\nu}{\nu_R(T,S)}\right)^{1-\eta}} - i\frac{\sigma(T,S)}{(2\pi\varepsilon_0)\nu} \tag{2.4}$$

Here, T is the temperature in degrees Celsius, S is the salinity in ppt, ν is the frequency in GHz, ν_R is the Debye relaxation frequency in GHz, σ is the conductivity (of water) in S/m, ε_0 is the electric permittivity at vacuum, and η is the Cole-Cole spread factor which is set to zero in the Klein-Swift model (Meissner and Wentz 2004, Cole and Cole 1941).

It was observed that the Klein-Swift model is sufficiently accurate at lower frequencies, (Guillou 1998, Wang 2002, and Wentz 1997). It was suggested by Leibe *et al.* (1991) that a second Debye relaxation frequency is required to fit high frequency data; they were able to fit their own high frequency measurements up to 1 THz using a double

Debye fit. Meissner and Wentz (2004) also implement a double Debye fit in their model of the complex dielectric constant of pure and sea water; their model is given below in equations 2.5-2.10. For pure water, S = 0 and the conductivity σ(T, S=0) = 0.

$$\varepsilon(T,S) = \frac{\varepsilon_s(T,S) - \varepsilon_1(T,S)}{1 + j \cdot \frac{\nu}{\nu_1(T,S)}} + \frac{\varepsilon_1(T,S) - \varepsilon_\infty(T,S)}{1 + j \cdot \frac{\nu}{\nu_2(T,S)}} + \varepsilon_\infty(T,S) - j \cdot \frac{\sigma(T,S)}{(2 \cdot \pi \cdot \varepsilon_0) \cdot \nu} \tag{2.5}$$

$$\varepsilon_s(T,S) = \frac{3.70886 \cdot 10^4 - 8.2168 \cdot 10^1 \cdot T}{4.21854 \cdot 10^2 \cdot T} \tag{2.6}$$

$$\varepsilon_1(T, S=0) = x_0 + x_1 \cdot T + x_2 \cdot T^2 \tag{2.7}$$

$$\nu_1(T, S=0) = \frac{45 + T}{x_3 + x_4 \cdot T + x_5 \cdot T^2} \tag{2.8}$$

$$\varepsilon_\infty(T, S=0) = x_6 + x_7 \cdot T \tag{2.9}$$

$$\nu_2(T, S=0) = \frac{45 + T}{x_8 + x_9 \cdot T + x_{10} \cdot T^2} \tag{2.10}$$

In equation 2.5, $j = \sqrt{-1}$ and ν_1 and ν_2 represent the two Debye relaxation frequencies in GHz. The parameters x_k are given below in Table 1.

Table 1. Parameters for the Meissner and Wentz model.

k	$\mathbf{x_k}$
0	5.7230 E 00
1	2.2379 E -02
2	-7.1237 E -04
3	5.0478 E 00
4	-7.0315 E -02
5	6.0059 E -04
6	3.6143 E 00
7	2.8841 E -02
8	1.3652 E -01
9	1.4825 E -03
10	2.4166 E -04

The Meissner and Wentz model of the complex dielectric constant of pure water is used as the basis for the new model for the complex dielectric constant of aqueous ammonia solutions.

Chapter III

Experiment Design, Theory, and Results

Multiple measurement systems have been developed at the Planetary Atmospheres Laboratory (PAL) at the Georgia Institute of Technology to precisely measure the complex dielectric properties of aqueous ammonia solutions relative to pure water. Throughout the study, the various experimental setups were modified based on preliminary results so as to ensure the most accurate measurements of the complex dielectric constants.

3.1 Measurement Theory

All of the measurement systems developed for this work are based on the use of the Agilent 85070E dielectric probe, operating in conjunction with an Agilent E5071C network analyzer. The probe acts as an open-ended transmission line. The provided Agilent software directs the network analyzer to generate and transmit a signal over specified microwave frequency bands to the test material (water and aqueous ammonia for this work) via the probe, to then measure the reflected response, and finally to relate the reflected signal to the materials' dielectric properties.

The Agilent 85070E dielectric probe has a relatively poor absolute accuracy of ±5% for the real part of the complex dielectric constant, ε'. To mitigate the uncertainty due to the dielectric probe instrumentation error, initial measurements of the complex dielectric

constant of deionized water (DI water) were made. The complex dielectric properties of water have been previously measured to high accuracy by Meissner and Wentz (2004), and the measurements were used to provide a baseline correction of data taken with the Agilent 85070E dielectric probe.

Measurements of the complex dielectric constant of test solutions were made in the 2–8.5GHz range. A complete sequence or data set recorded 30 sweeps/measurements with 1000 linearly spaced data points in the specified frequency range. Multiple measurements were taken of each solution per temperature to develop a statistic for the variability in the data sets. The measurements recorded are tabulated in Table 2.

Table 2. Number of measurement sets recorded per solution per temperature.

	Room Temperature ~23°C	High Temperature ~40°C	Cold Temperature ~4°C
Deionized Water (0% NH_3/vol)	8	3	3
0.5N NH_4OH (0.85% NH_3/vol)	2	3	3
1N NH_4OH (1.7% NH_3/vol)	2	3	3
2N NH_4OH (3.4% NH_3/vol)	2	3	3
5N NH_4OH (8.5% NH_3/vol)	2	3	3

The complex dielectric constant of water varies with temperature, and it was assumed that the dielectric properties of aqueous ammonia would likely have a similar temperature dependence. Temperature was carefully monitored for each set of measurements.

Due to the volatile nature of aqueous ammonia and the high vapor pressure of NH_3 relative to water, preferential evaporation of NH_3 from the aqueous ammonia solutions was expected. Thus, the pH of the solution under test was recorded for each set of measurements so as to monitor NH_3 concentration.

The dielectric probe operates similar to a transmission line passing through a boundary of two mediums with the second medium being the dielectric liquid as shown in Figure 4.

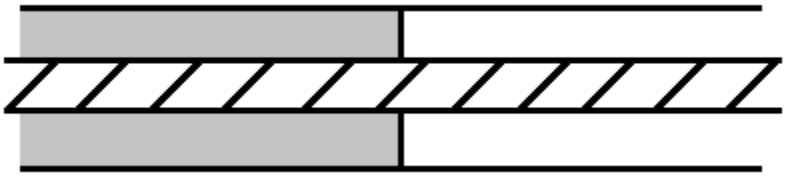

Figure 4. Transmission line passing through a boundary of two different mediums.

The probe software calculates the dielectric properties of the test material by measuring the reflection coefficient, Γ, at the boundary and relating this parameter to the dielectric properties. In transmission line theory, the ratio of a reflected signal to the incident signal is related as

$$\Gamma = \frac{V^-}{V^+} = \frac{Z_L - Z_0}{Z_L + Z_0}, \tag{3.1}$$

where V^+ is the incident transmitted signal, V^- is the reflected signal, Z_L is the impedance of the load or material under test (MUT), and Z_0 is the characteristic

impedance of the transmission line (Hayt and Buck 2006). For a large distributed medium, the load impedance can be written as

$$Z_L = Z_0 \cdot \sqrt{\frac{j\omega\mu}{\sigma + j\omega\varepsilon}}, \tag{3.2}$$

where ω is the angular frequency, μ is the magnetic permeability, σ is the conductivity, and ε is the electric permittivity. For a perfectly-insulating dielectric material, where conductivity is zero, the load impedance can be reduced to

$$Z_L = \sqrt{\frac{\mu}{\varepsilon_e}}. \tag{3.3}$$

Here ε_e refers to the effective dielectric permittivity of the medium which is defined as $\varepsilon_e = \varepsilon + \frac{\sigma}{j \cdot \omega} = \varepsilon_e' - j \cdot \varepsilon_e''$. The concept of a complex electric permittivity arises from the non-ideal nature of materials relating to permanent or induced dipole relaxation, resonance effects of atoms, ions, or electrons, and conduction effects of dielectric materials (Hayt and Buck 2006). This complex electric permittivity can be used to write the load impedance as

$$Z_L = \sqrt{\frac{\mu}{\varepsilon' - j\varepsilon''}}, \tag{3.4}$$

where ε' and ε'' are the real and imaginary parts, respectively, of the complex dielectric constant of the load or MUT.

3.2 Room Temperature Experimental Setup

The measurement system used for room temperature measurements for this work is shown in Figures 5 and 6. The main component of the system is the Agilent 85070E dielectric probe. The dielectric probe is connected to an Agilent E5071B/C vector network analyzer (VNA) which is controlled by the Agilent 85070E software. Custom software in MATLAB® was developed by a previous Georgia Tech student, Sahand Noorizadeh, to automate the data acquisition.

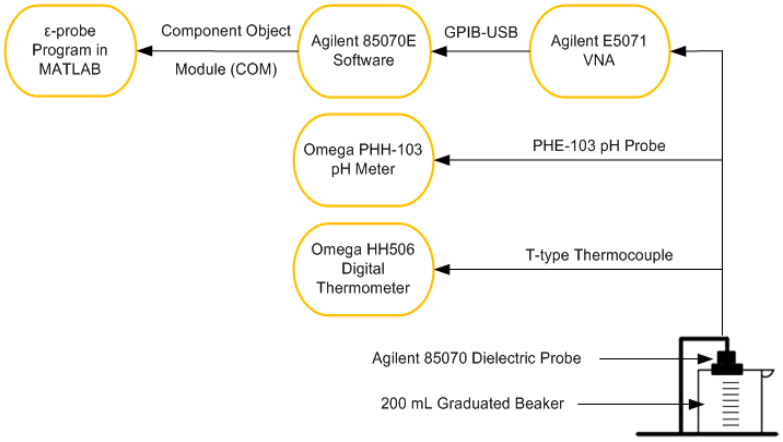

Figure 5. Block diagram of the room temperature measurement system.

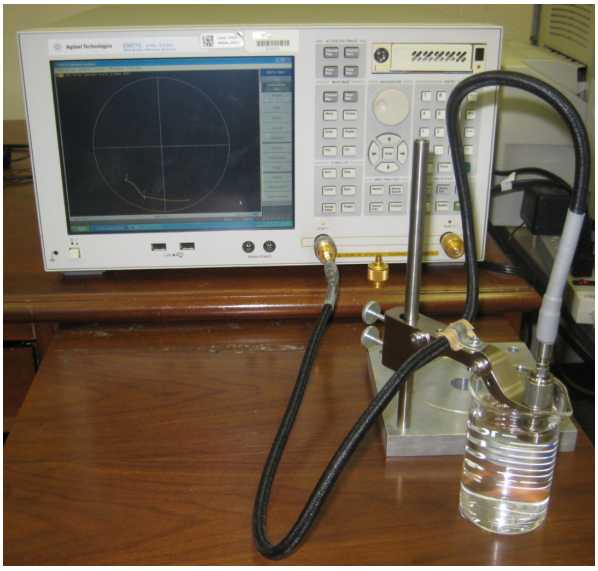

Figure 6. The room temperature experimental setup. The dielectric probe submerged in the solution in test is connected to the Agilent 5071C VNA.

Solutions were tested in a 200mL graduated beaker. The temperature and pH of the solution were monitored using the HH506 digital thermometer and Omega PHH-103 pH meter, respectively, to verify the temperature and concentration of ammonia. The Omega PHH-103 has a pH measurement resolution of 0.01 and an accuracy of ±0.02. The Omega HH506 digital thermometer has a temperature resolution of 0.1°C and an accuracy of ±(0.05% rdg (°C) + 0.3°C) when using a T-type thermocouple.

The Agilent 85070E dielectric probe has a calibration process that was used before each set of sequence of measurements at a particular temperature, i.e., one calibration for all measurements at a given temperature.

3.3 High Temperature Experimental Setup

To understand the effect of changes in temperature on the complex dielectric properties of aqueous ammonia, a high temperature measurement system was designed. Initially, the high temperature system was identical to the room temperature system shown in Figure 5 with the dielectric probe and solution in test in an oven rated up to 600 degrees Kelvin. An Omega CN77000 temperature controller was used with a T-type thermocouple to control the oven temperature. The Omega CN77000 has an accuracy of $\pm 0.4^{o}$C and could maintain the oven temperature to within $\pm 2^{o}$C of the set temperature value. The Omega HH506 digital thermometer, and later the Omega PHH-103 pH probe, was used to monitor the temperature of the solution in test.

After initial tests, it was determined that ammonia was preferentially evaporating from the aqueous ammonia solutions under test. This is due to the higher vapor pressure of ammonia than water, and this was confirmed with pH measurements. To reduce the evaporation of ammonia, 200 mL glass jars with a screw-on PTFE lined cap machined to fit the 85070E dielectric probe were used. In order to monitor the pH over the period of heating and measurement without disturbing the solution in test, a second 200 mL sealed glass jar was used as an analog system. With this analog system, the Omega PHH-103 was fitted to the analog jar and monitored both pH and temperature with ± 0.02 and $\pm 0.3^{o}$C accuracy, respectively. The high temperature system is shown in Figures 7 and 8.

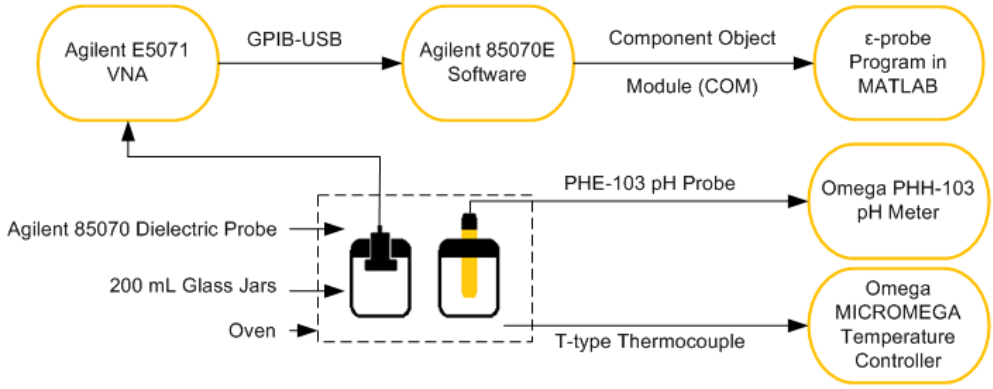

Figure 7. Block diagram of the high temperature measurement system.

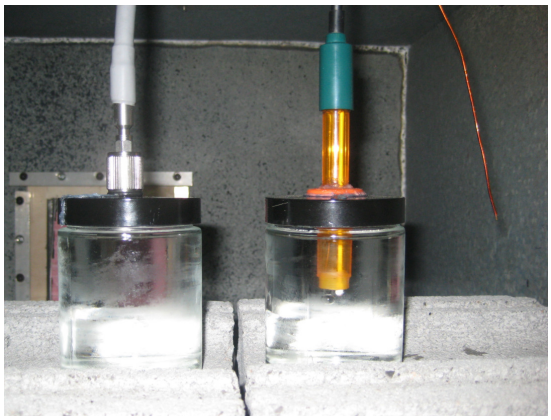

Figure 8. The high temperature experimental setup inside of the oven. The dielectric probe is submerged in the sealed container on the left. The pH probe is submerged in an analog system on the right. The T-type thermocouple which controls the oven temperature is shown on the right.

Measurements were initially planned for 40°C and 60°C. However, because of the large amount of ammonia outgassing at 60 °C, only 40°C measurements were taken.

3.4 Cold Temperature Experimental Setup

Due to the volatility of aqueous ammonia, especially at higher temperatures, it was determined that cold temperature measurements would provide a more reliable data set to develop a model for the temperature dependence of the complex dielectric properties

of aqueous ammonia. A block diagram of the cold temperature measurement is shown in Figure 9.

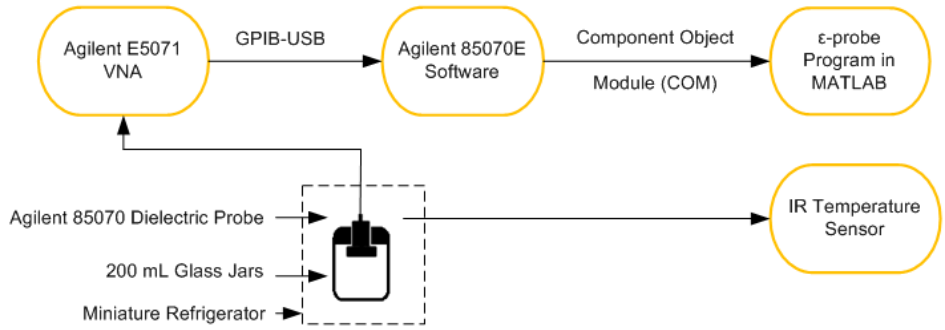

Figure 9. Block diagram of the cold temperature measurement system.

A miniature refrigerator was used to cool the solutions under test; the refrigerator was able to maintain a temperature of 4°C ± 0.6°C. Since aqueous ammonia is more stable at colder temperatures, continuous monitoring of the pH of the solutions under test was not necessary for the cold temperature measurements. Temperature was monitored by a Fluke 62 miniature IR thermometer which has a resolution of ±1°C and an accuracy of ±1.5°C. Temperature was monitored with the IR thermometer because it would not interfere with the dielectric probe measurement system and eliminated the need for an analog system.

3.5 Calibration with Water Measurements

The absolute accuracy of these lab measurements depends on the accuracy of measurements of the properties of aqueous ammonia solutions relative to the reference (water). Water was chosen as the reference measurement because its properties are well

documented (Meissner and Wentz 2004). By performing relative measurements with a well-known reference versus absolute measurements, the errors associated with the measurement system are decreased.

The water calibration is performed by taking three measurements of pure water at each temperature (23 ± 0.5 °C for room temperature and 4.5 ± 1.7 °C for cold temperature), and correcting them to fit the Meissner and Wentz model for pure water. The correction factor is obtained from the water measurements using a linear difference operation on the data so that it conforms to the Meissner and Wentz model. The linear correction was chosen over other possible mathematical operators because it was able to correct for systematic fluctuations easily. For example, the measurements of both the real and imaginary parts of the dielectric constants exhibited a residual standing wave of ~3 GHz length which could not be properly corrected for using a ratio-based correction factor.

A sample plot of a water data set at 23.9 °C, the Meissner and Wentz model at 23.9 °C, and the correction factor applied to all room temperature measurements is shown below in Figure 10. The same data set with the correction factor applied is shown in Figure 11.

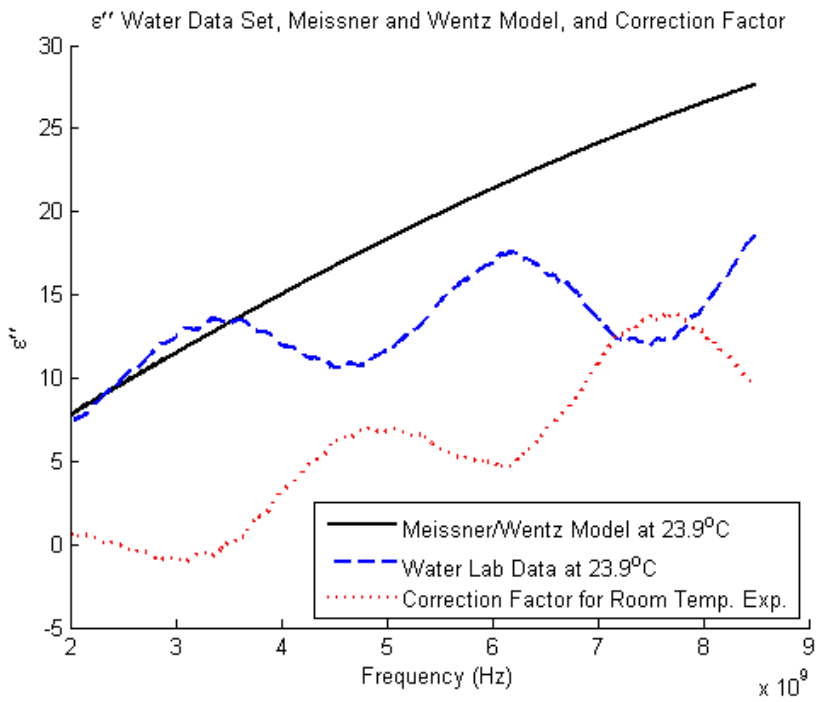

Figure 10. Meissner and Wentz model and correction factor for all room temperature measurements. The correction factor is a linear difference operation of all water measurements at room temperature and the model.

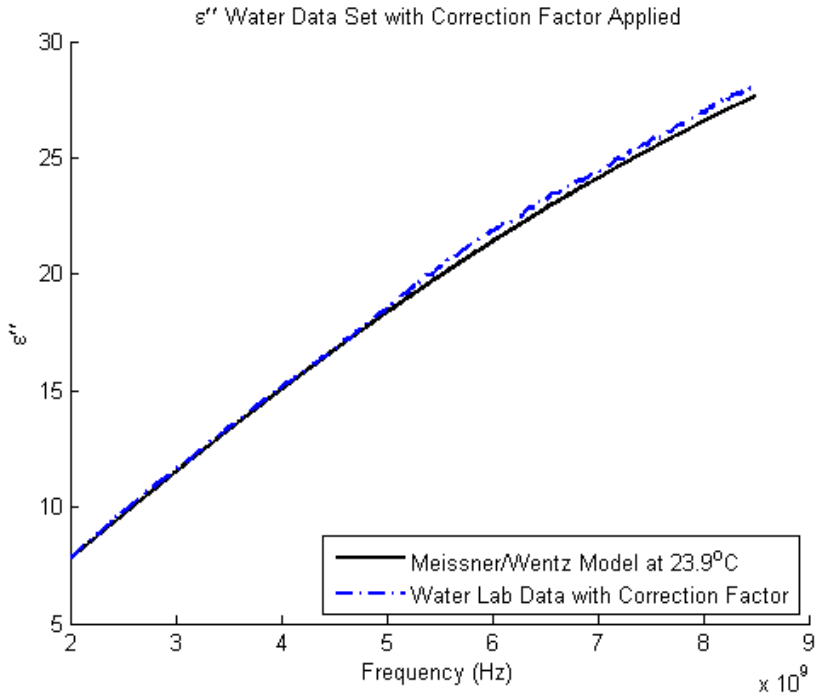

Figure 11. The same water data set at 23.9 °C with the room temperature correction factor applied. The Meissner and Wentz model is shown as reference.

As can be seen from Figure 11, the linear correction model provides a reliable fit over the entire frequency range.

3.6 Ammonia Concentration Verification

An accurate knowledge of the NH_3 concentration in the aqueous ammonia solutions under test is required for an accurate model of its properties. Access to a method to determine the ammonia concentration directly was not available for these measurements. However, a pH meter proved effective in monitoring the acidity of the aqueous ammonia solutions during test, and an independent pH study was performed to verify the validity of the pH measurements.

A sequence of 30 measurements of the complex dielectric properties of the aqueous ammonia solutions typically took 20 minutes to complete. For room temperature measurements, this was the only period in which the aqueous ammonia solution in test was exposed to the open air. Of major concern was the amount of NH_3 that vaporized from the aqueous ammonia solution during the experiment.

The concentration verification experiments consisted of using a Vernier PH_BTA pH probe connected to a Vernier LabPro sensor interface to measure the pH of an identical solution of aqueous ammonia exposed to open air for a 20 minute period. The resolution of the Vernier PH_BTA probe is documented as 0.02 pH units, and the probe was

calibrated using 4.0 and 7.0 pH buffer solutions before each trial. The probe was unable to measure the pH of deionized water due to the lack of any ionization, so only the pH of aqueous ammonia solutions were measured. The experiment consisted of placing the pH probe in a solution of aqueous ammonia at room temperature for five minutes to allow the meter to stabilize and then monitoring the pH for 20 minutes. Two trials were performed for each concentration of aqueous ammonia; the results are shown in Figure 12 and Table 3.

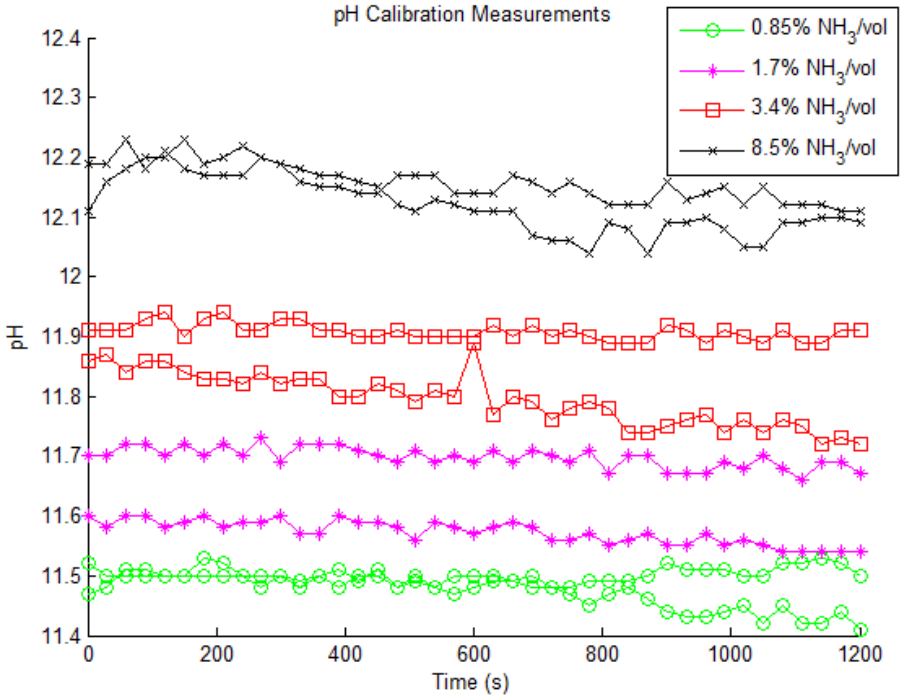

Figure 12. Results of the ammonia concentration study at room temperature. pH is used as an indication of ammonia concentration in aqueous ammonia.

Table 3. Tabulated results for the concentration validation experiments.

Concentration (% NH_3/vol)	Trial	Minimum pH (pH units)	Maximum pH (pH units)	Mean pH (pH units)	Standard Deviation
0.85	1	11.48	11.53	11.500	0.0126
0.85	2	11.41	11.53	11.474	0.0309
1.7	1	11.66	11.73	11.698	0.0171
1.7	2	11.54	11.60	11.572	0.0198
3.4	1	11.72	11.89	11.795	0.0444
3.4	2	11.89	11.94	11.908	0.0136
8.5	1	12.04	12.23	12.124	0.0538
8.5	2	12.11	12.23	12.154	0.0284

As shown in Table 3 the standard deviation is low for the experiments, with only one 8.5 %NH_3/volume concentration trial having a standard deviation above 0.05 pH units. Particularly at the higher concentrations such as 3.4% and 8.5% NH_3/volume, there appears to be some loss in concentration over the span of 25 minutes. However, the change in ammonia concentration is small relative to other uncertainties.

3.7 Experimental Results

The Agilent 85070E dielectric probe software provides results for the complex dielectric properties of the solution in test directly. An example of one complete data set is shown in Figures 13 and 14.

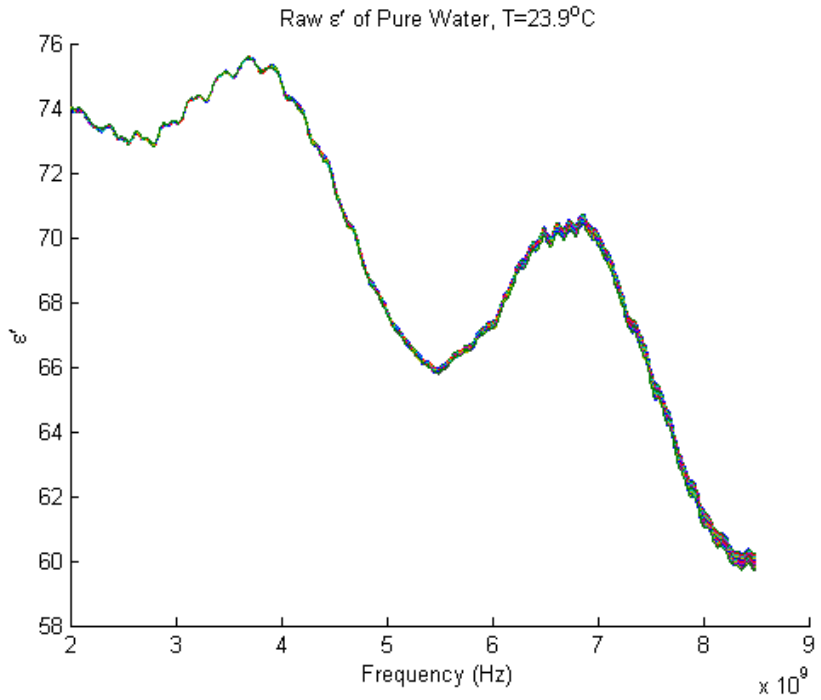

Figure 13. Raw data for one sequence (30 sweeps) of ε' measurements at room temperature (23.9 °C).

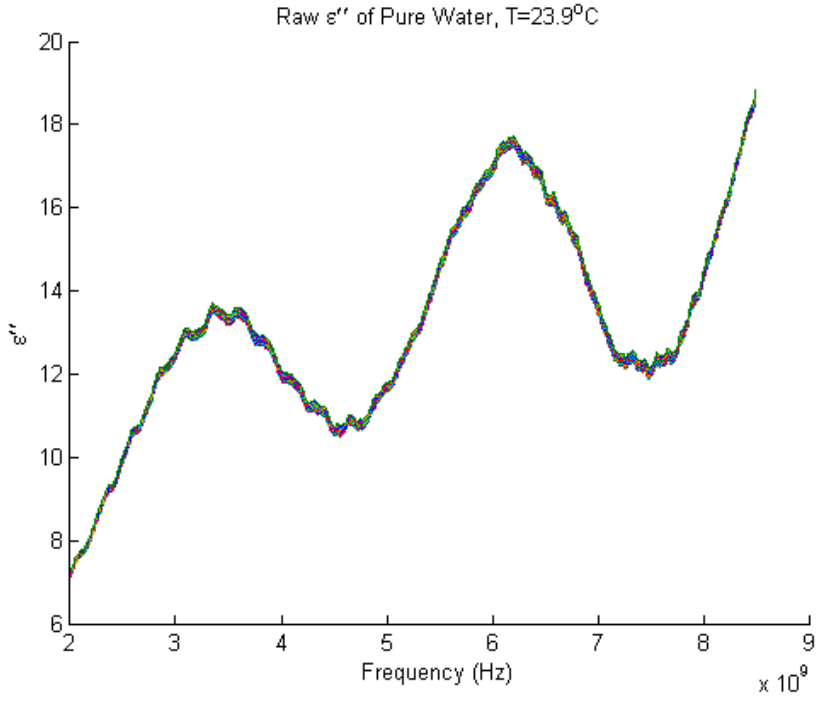

Figure 14. Raw data for one sequence (30 sweeps) of ε" measurements at room temperature (23.9 °C).

The data shown in Figures 13 and 14 are characteristic of all sequences of measurements for room, high, and cold temperature measurements. This data may be plotted concurrently with the Meissner and Wentz (2004) model as a comparison, shown below in Figures 15 and 16.

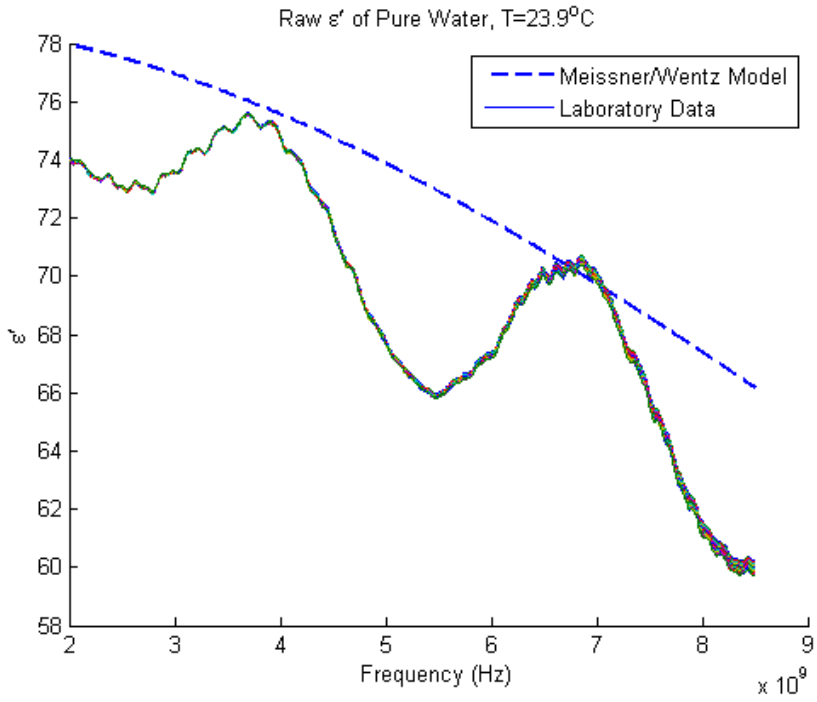

Figure 15. Raw data for one sequence (30 sweeps) of ε' measurements at room temperature (23.9°C) with Meissner and Wentz model for pure water.

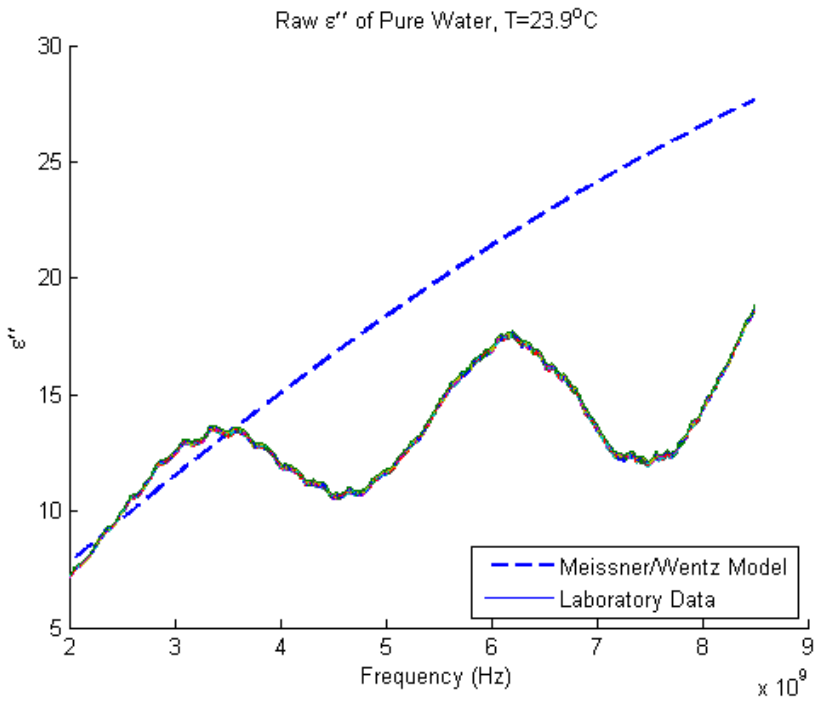

Figure 16. Raw data for one sequence (30 sweeps) of ε" measurements at room temperature (23.9°C) with Meissner and Wentz model for pure water.

There exists a systematic standing wave among all data sets due to reflections from the test setup, and there also exists smaller higher frequency ripples in the overall spectral response. The higher frequency ripples became more prominent over a period of days due to calibration drift. Thus, all experiments for a particular temperature were completed over a period of less than one week.

Chapter IV

Model Fitting and Modifications

In total, 26 data sets were taken (11 at ~24 °C and 15 at ~4 °C). A new model for the complex dielectric constant of aqueous ammonia has been developed which fits 60.26% of all 780,000 measured data points within 2σ uncertainty. Consideration of the model fitting process and the final model are presented.

4.1 Measurement Uncertainty

Two uncertainties exist for both the room temperature and the cold temperature measurement systems: instrumentation errors and electrical noise (Err_{inst}) and conditional errors (Err_{cond}), which reflect the uncertainties in environmental conditions during the experiments. The term *Err* is used to describe a bound on uncertainty within 2σ.

Instrumentation errors arise due to noise from the internal electronics of the test equipment used. Since the measurements are compared to a reference (pure water), the relative change in response is of most importance, and thus the absolute uncertainty associated with the Agilent E5071C VNA is not considered.

Electrical noise from the test equipment is partially mitigated by taking 30 sweeps of measurements for each data set. The uncertainty that arises from electrical noise is

modeled as a probability distribution of the 30 measurements per data set. The probability distribution chosen is the Student's t-test with a 95% confidence interval (Hines *et al.* 2003), which is approximately equivalent to 2σ uncertainty (95.4%). For a data set of 30 measurements, Err_{inst} is calculated as

$$Err_{inst} = \frac{t_n}{\sqrt{n}} \cdot S_n \,, \tag{4.1}$$

where n is the number of samples in the distribution (30), t_n is the student t-test coefficient (critical value) for a 95% confidence interval, and S_n is the sample standard deviation. Common t-test values for 95% confidence are tabulated in Table 4, and the sample standard deviation is calculated as

$$S_n = \sqrt{\frac{1}{n-1}\sum_{i-1}^{n}(x_i - \bar{x})^2} \,, \tag{4.2}$$

where x_i is the measured value and $\bar{x}$ is the sampled mean of the n number of measurements.

Table 4. T-test coefficients for a two-sided 95% confidence interval.

n	3	5	10	15	20	25	30	∞
$\mathbf{t_{test}(n)}$	4.303	2.776	2.262	2.145	2.093	2.064	2.045	1.960

This probability distribution implies that the actual mean lies within the measured mean plus or minus the error bound calculated from the Student's t-test with 95% confidence ($\bar{x} \pm Err_{inst}$) (Hines *et al.* 2003).

Conditional errors arise from uncertainties in the measurement conditions including temperature, concentration of NH_3, pressure, etc. Uncertainties in temperature are most readily calculated as temperature was recorded for every set of measurements. Absolute uncertainties exist for the Omega HH-23A digital thermometer using a T-type thermocouple (Omega Engineering 2007), Omega PHH-103 pH/temperature meter (Omega Engineering 2010), and Fluke 62 Mini IR thermometer (Fluke 2010) as listed in Table 5.

Table 5. Rated resolution and accuracy of various thermometers used.

Meter	Resolution (°C)	Accuracy (°C)
Omega HH-23A (T-type thermocouple)	0.1	±(0.1% rdg + 0.6)
Omega PHH-103 pH/Temperature meter	0.1	0.3
Fluke 62 Mini IR thermometer	0.2	±1.5% rdg or ± 1.5, whichever is greater

The uncertainty in the complex dielectric constant as a result of uncertainties in the measurement of temperature is estimated by calculating the difference between the Meissner and Wentz model for pure water at the measured temperature (T) and the model value at the measured temperature plus the maximum error in temperature measurement (T_{max_dev}) as shown in equation 4.3.

$$Err_{temp} = \left|\text{model}(T) - \text{model}(T + T_{\text{max\_dev}})\right| \tag{4.3}$$

The solutions' pH values were measured during the experiments, and an independent pH-concentration verification experiment described in chapter III was performed to verify that the concentration of NH_3 remained stable during each measurement period.

A method for absolutely measuring the NH_3 concentration in aqueous ammonia solutions was not available for this work, and thus, a statistical bound on the uncertainty on the concentration is not available. Based on the pH measurements, the concentration is assumed to be constant for the purpose of this model. Thus Err_{cond} is only determined by the uncertainties in the measured dielectric properties resulting from the uncertainty in temperature,

$$Err_{cond} = \sqrt{Err_{temp}^{\ 2}} = Err_{temp}. \tag{4.4}$$

The total error associated with a sequence of 30 measurements is calculated as the square root of the sum of squares of Err_{inst} and Err_{cond} as shown in equation 4.5.

$$Err_{total} = \sqrt{Err_{inst}^{\ 2} + Err_{cond}^{\ 2}} \tag{4.5}$$

This calculation of total error is consistent with the independence of the instrumental and conditional errors.

4.2 Model Fitting Process

The measured data used for fitting the new model consists of 26 data sets of 30 measurement sweeps ranging from temperatures of 1.2 to 23.9 °C and concentrations of 0 to 8.5 % NH_3/vol between 2-8.5 GHz as presented in Table 6.

Table 6. Data sets used for model fitting.

Data Set	Date/Time Measured	Concentration (%NH_3/vol)	Temperature (°C)
1	7/1/2010 - 19:21	0	23.9
2	7/1/2010 - 19:52	0.85	21.7
3	7/1/2010 - 20:13	1.7	21.7
4	7/1/2010 - 20:37	3.4	21.7
5	7/1/2010 - 22:46	8.5	20.0
6	7/1/2010 - 23:39	0	23.0
7	7/2/2010 - 00:07	8.5	20.7
8	7/2/2010 - 00:36	3.4	21.5
9	7/2/2010 - 01:02	1.7	22.1
10	7/2/2010 - 01:28	0.85	22.1
11	7/2/2010 - 01:52	0	22.5
12	1/7/2011 - 01:21	8.5	3.2
13	1/7/2011 - 02:10	3.4	1.9
14	1/7/2011 - 03:02	1.7	1.8
15	1/7/2011 - 03:48	0.85	1.2
16	1/7/2011 - 04:47	0	3.6
17	1/7/2011 - 05:12	0.85	3.0
18	1/7/2011 - 05:41	1.7	3.6
19	1/7/2011 - 13:05	3.4	1.2
20	1/7/2011 - 13:32	8.5	3.2
21	1/7/2011 - 14:39	0	4.2
22	1/7/2011 - 15:11	8.5	4.0
23	1/7/2011 - 15:38	3.4	4.2
24	1/7/2011 - 16:10	1.7	4.8
25	1/7/2011 - 16:35	0.85	5.6
26	1/7/2011 - 17:00	0	6.2

For the model fitting process, an adaptation of the Levenberg-Marquardt optimization algorithm was used (Levenberg 1944, Marquardt 1963). The algorithm used the χ-minimizing function

$$\chi = \sum_{n=1}^{26} \frac{\varepsilon_{\text{measured}} - \varepsilon_{\text{model}}}{\sigma_{\text{measured}}}, \tag{4.6}$$

where, $\varepsilon_{measured}$ is the measured dielectric constant, ε_{model} is the modeled dielectric constant under model optimization, and $\sigma_{measured}$ is the 2σ uncertainty in the measured data. Equation 4.6 is a modification of minimizing functions used in previous model fitting processes (see e.g., Hanley 2007, Devaraj 2011). Model fitting for the real component (ε') and imaginary component (ε") of the dielectric constant must be conducted independently; however, the model is optimized so as to minimize χ for both components.

The model optimization process fits unknown coefficients of a particular mathematical form so as to minimize the value of χ over all 26 data sets. The Meissner and Wentz (2004) model was used as the basis for the new model. A constraint applied to the new model is that it must match the Meissner and Wentz model when the solution's ammonia concentration equals zero, 0. The model optimization must account for the temperature, frequency, and concentration dependencies when NH_3 is added to water. The first mathematical form that converged across all data sets was

$$\Delta_{NH_3,1}(C,f,T) = \frac{x_{11}\cdot C\cdot f^{x_{12}}}{T^{x_{13}}} + j\cdot\frac{x_{14}\cdot C\cdot f^{x_{15}}}{T^{x_{16}}}, \tag{4.7}$$

where $j=\sqrt{-1}$, C is the concentration of $\%NH_3$/vol, f is the frequency, T is the temperature, and the coefficients x_k are given in Table 7.

Table 7. Coefficients x_k for equation 4.7.

k	x_k
11	-7.800 E 01
12	1.090 E -02
13	5.860 E -02
14	2.264 E 02
15	2.310 E -02
16	1.290 E 01

When the parameter $\Delta_{NH_3,1}(C,f,T)$ is linearly added to the Meissner and Wentz model for pure water (equation 2.5), the new preliminary model fit the real component of the dielectric constant, ε', of aqueous ammonia of the laboratory data well, as shown in Figures 17 and 18.

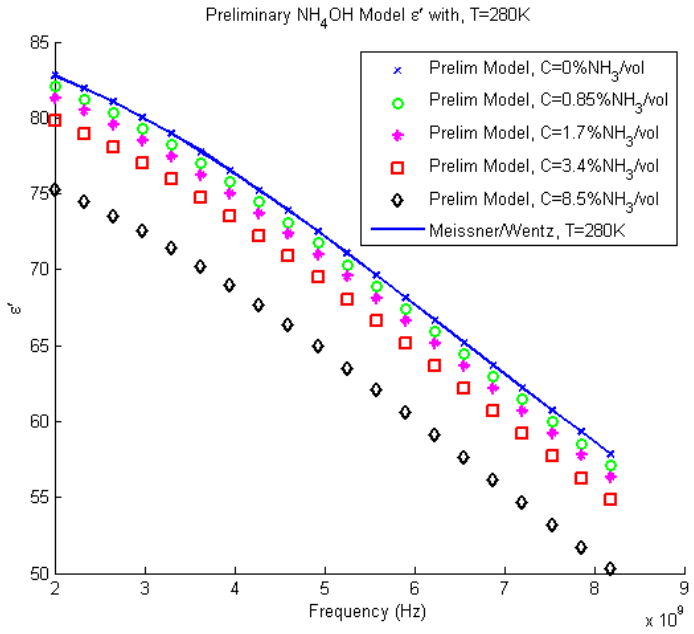

Figure 17. Preliminary model results with T=280K and varying concentration.

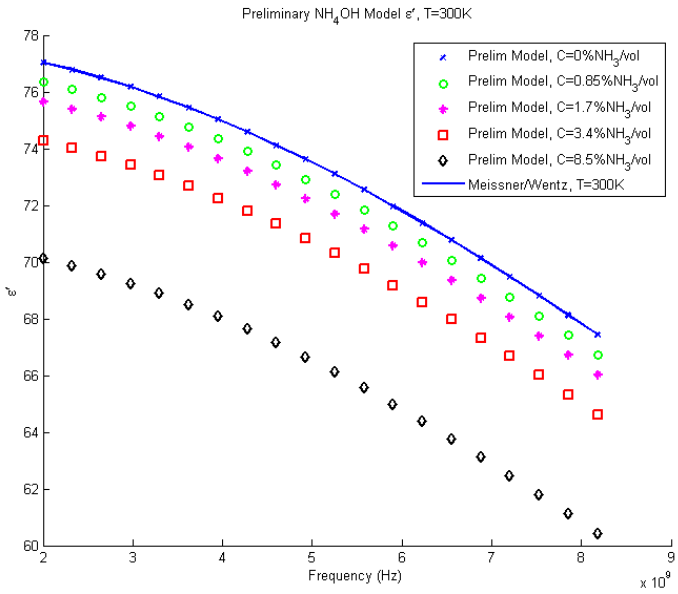

Figure 18. Preliminary model results with T=300K and varying concentration.

Since the temperature and frequency dependencies of ε" were fit well with the preliminary model, it was determined that an additional factor dependent only on ammonia concentration in the imaginary domain was required. The mathematical forms shown in equations 4.8 and 4.9 are modifications of $\Delta_{NH_3,1}(C,f,T)$ to better account for the effect of NH_3 on the imaginary component of the new model.

$$\Delta_{NH_3,2}(C,f,T) = \frac{x_{11}\cdot C\cdot f^{x_{12}}}{T^{x_{13}}} + j\cdot\left(\frac{x_{14}\cdot C\cdot f^{x_{15}}}{T^{x_{16}}} + x_{17}\cdot C\right) \tag{4.8}$$

$$\Delta_{NH_3,3}(C,f,T) = \frac{x_{11}\cdot C\cdot f^{x_{12}}}{T^{x_{13}}} + j\cdot\left(\frac{x_{14}\cdot C\cdot f^{x_{15}}}{T^{x_{16}}} + x_{18}\cdot C^{x_{19}}\right) \tag{4.9}$$

Parameters x_k for k=11...16 are presented in Table 7, and parameters x_k for k=17...19 are presented in Table 8.

Table 8. Coefficients x_k for equations 4.8 and 4.9.

k	x_k
17	2.477 E 01
18	1.962 E 01
19	9.081 E -01

The new parameter $\Delta_{NH_3,2}(C,f,T)$ better accounts for the concentration of aqueous ammonia as shown in Figure 19, and fits the experimental data better than $\Delta_{NH_3,3}(C,f,T)$ (60.26% versus 60.25%, respectively, within 2σ uncertainty).

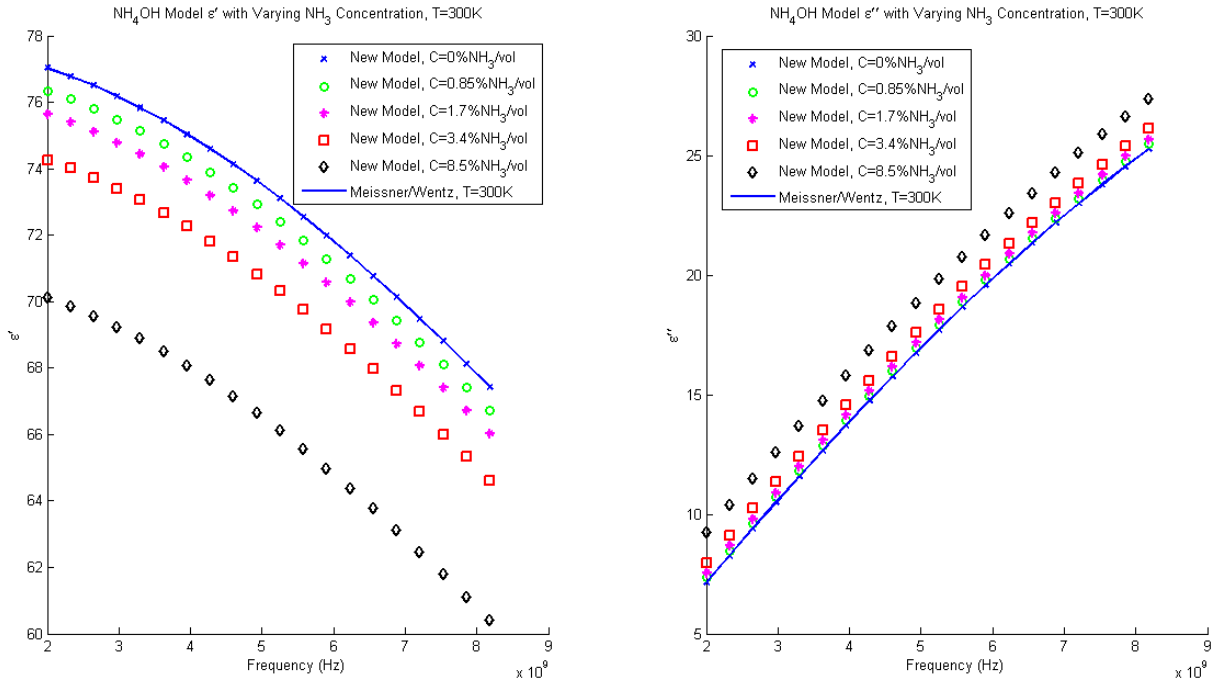

Figure 19. Preliminary model using parameter $\Delta_{NH_3,2}$ results with T=300K and varying concentration.

For cold temperature measurements, there was an artificial deviation in ε" at the higher frequencies as shown in Figure 20.

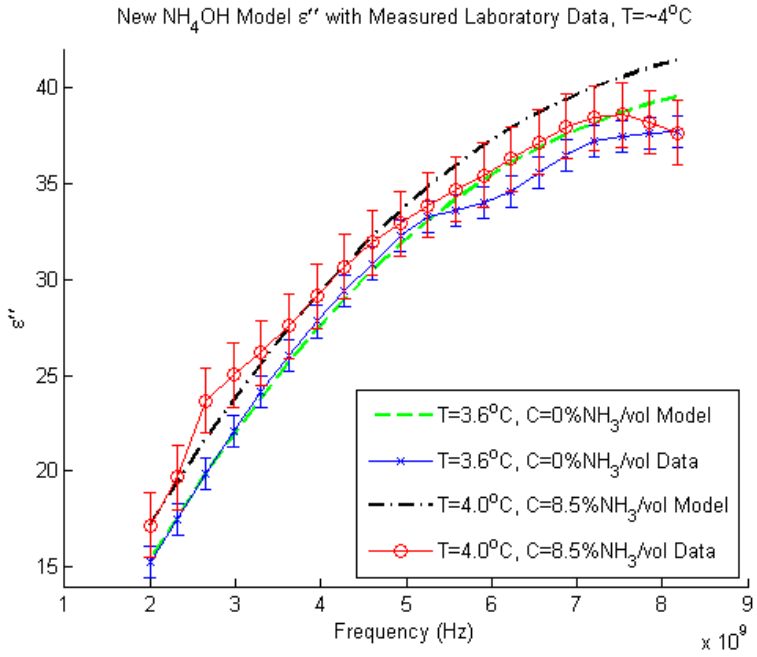

Figure 20. Cold temperature data showing artificial deviation at higher frequencies.

This deviation is noticed at about 5.5 GHz and is systematic across all cold temperature measurements. The deviation is possibly caused due to resonances of the enclosed refrigerator (box resonator) or systematic errors when operating at the colder temperatures. As the deviations are artificial, the new model's fit of 60.26% of all laboratory data points is likely an underestimation of the true fit given a refrigerator cavity that is sufficiently large and a temperature insensitive dielectric probe.

A presentation of the new model's fit against laboratory data is shown in Figures 21-30, and a complete presentation of the new model's performance as compared to laboratory data is available in Appendix B.

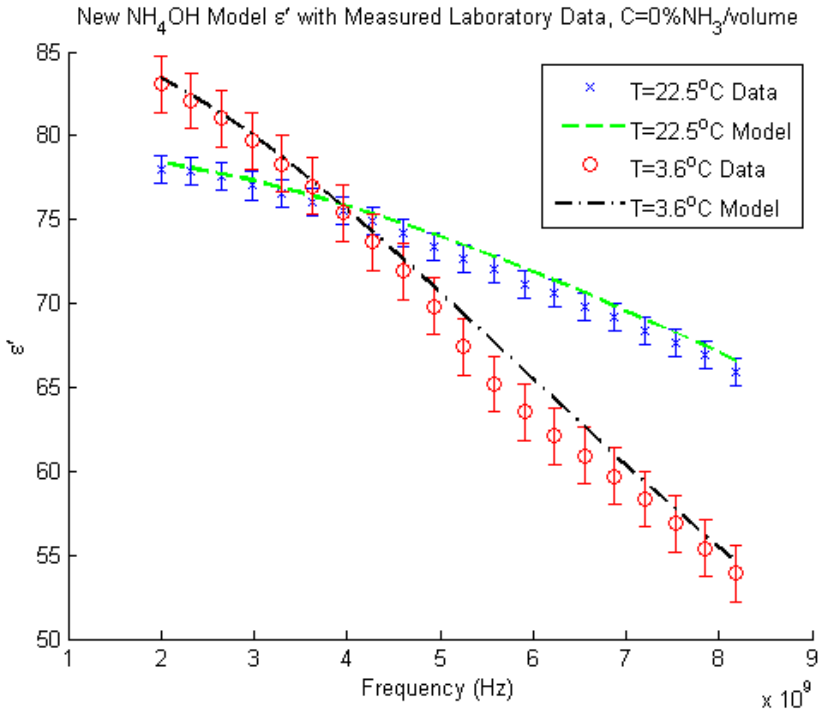

Figure 21. New model plotted with laboratory data (ε') at zero ammonia concentration and temperatures of 22.5 and 3.6 degrees Celsius.

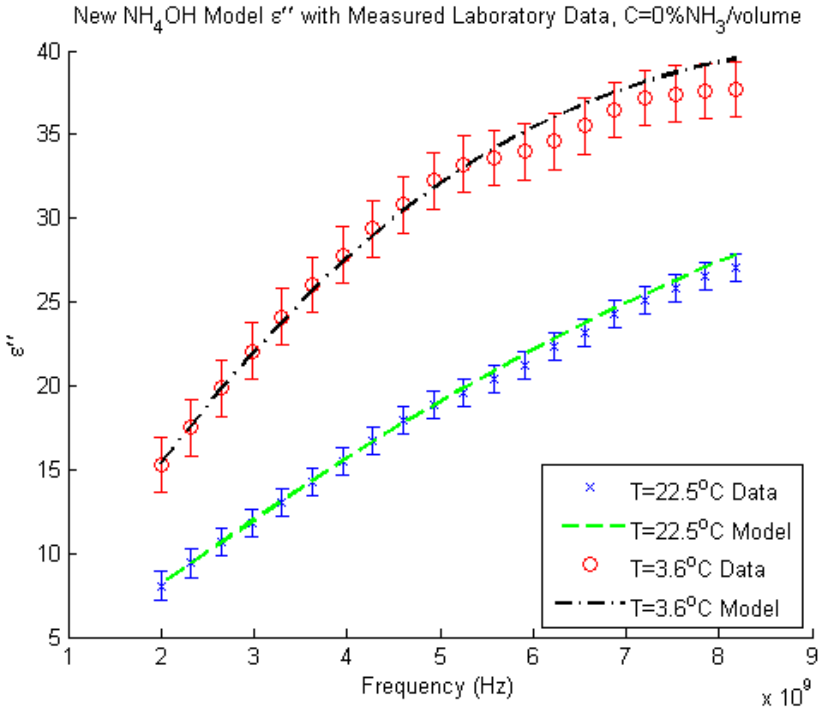

Figure 22. New model plotted with laboratory data (ε") at zero ammonia concentration and temperatures of 22.5 and 3.6 degrees Celsius.

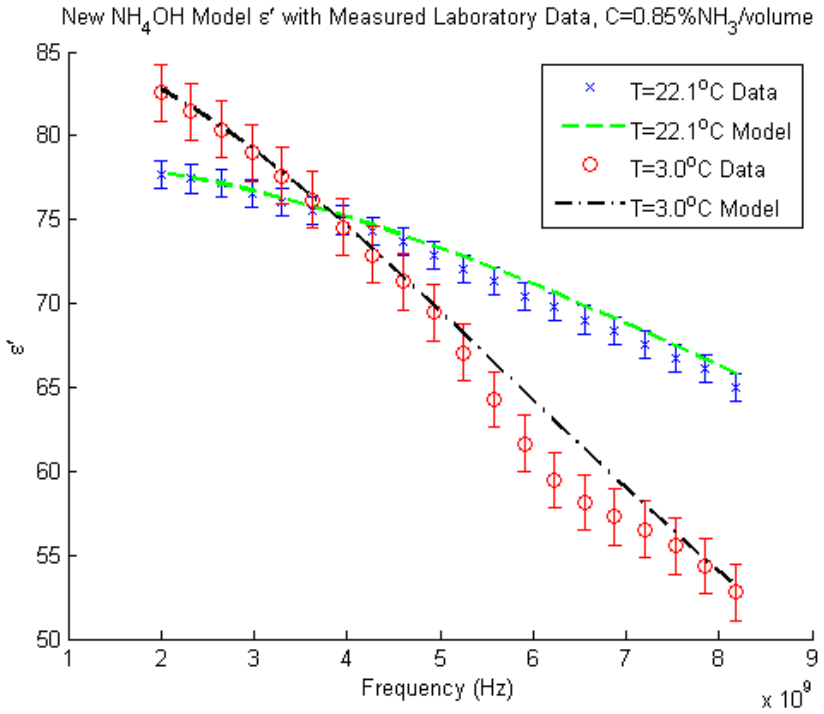

Figure 23. New model plotted with laboratory data (ε') at 0.85 %NH_3/volume ammonia concentration and temperatures of 22.1 and 3.0 degrees Celsius.

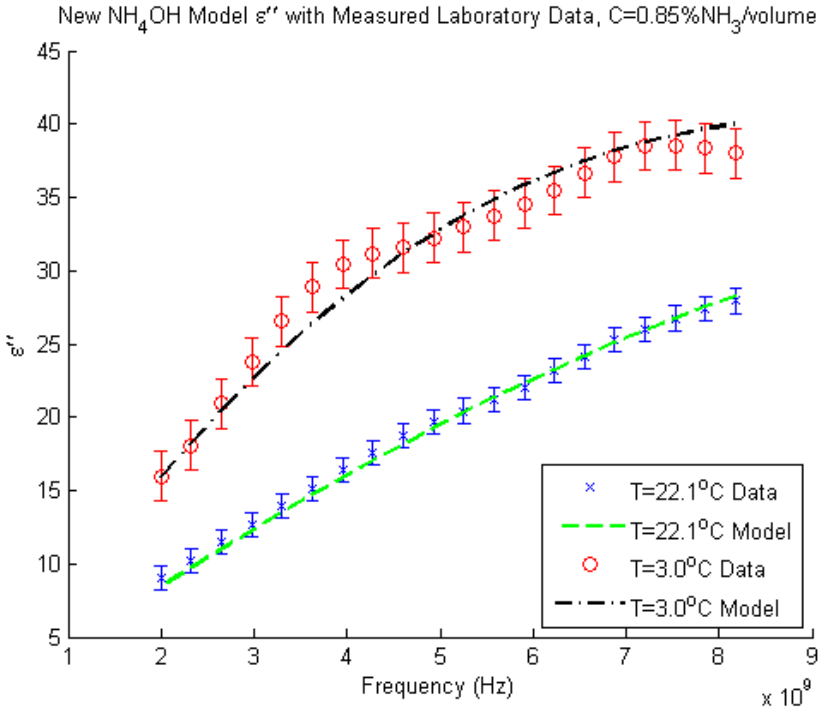

Figure 24. New model plotted with laboratory data (ε") at 0.85 %NH_3/volume ammonia concentration and temperatures of 22.1 and 3.0 degrees Celsius.

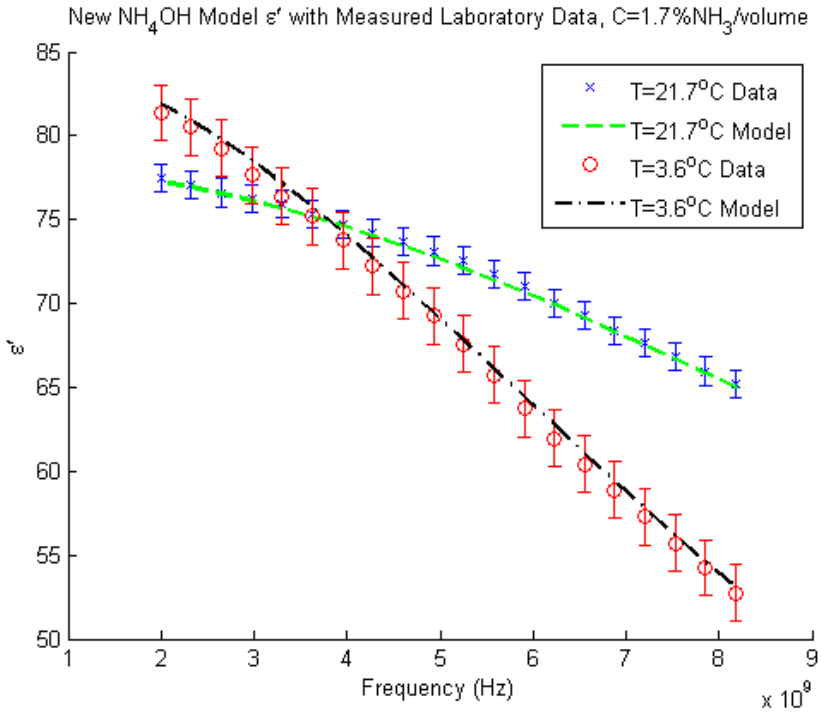

Figure 25. New model plotted with laboratory data (ε') at 1.7 %NH_3/volume ammonia concentration and temperatures of 21.7 and 3.6 degrees Celsius.

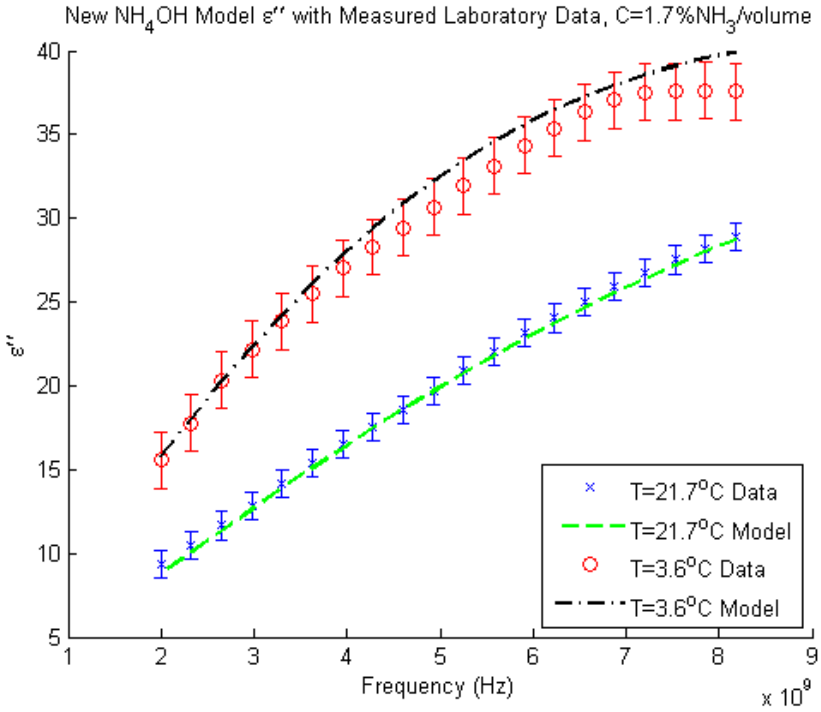

Figure 26. New model plotted with laboratory data (ε") at 1.7 %NH_3/volume ammonia concentration and temperatures of 21.7 and 3.6 degrees Celsius.

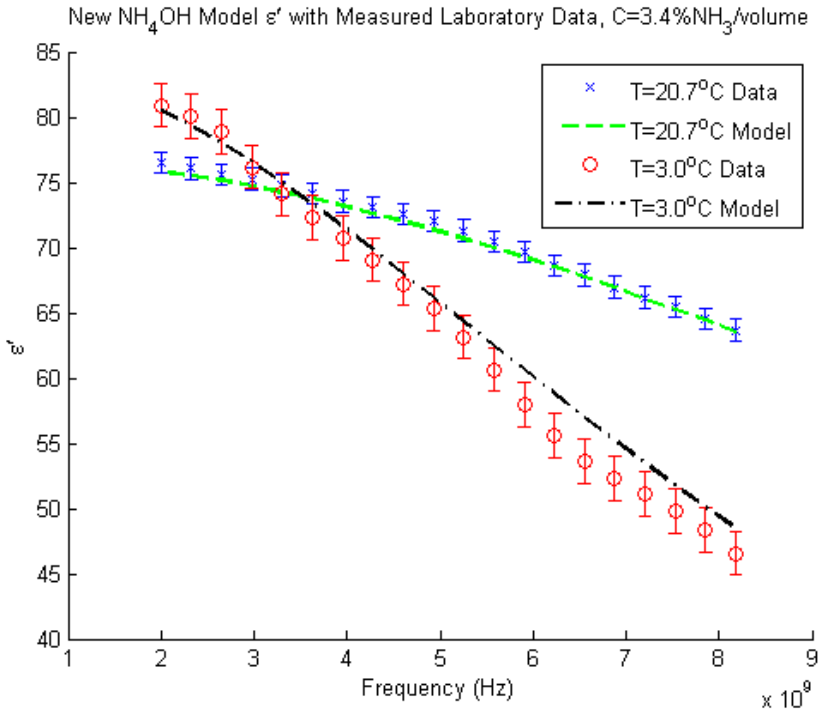

Figure 27. New model plotted with laboratory data (ε') at 3.4 %NH_3/volume ammonia concentration and temperatures of 20.7 and 3.0 degrees Celsius.

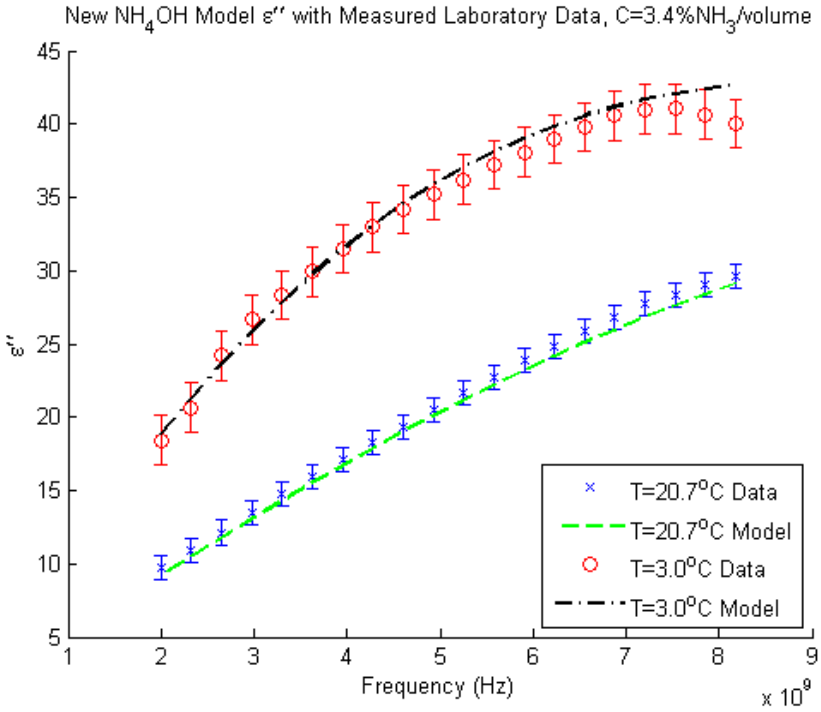

Figure 28. New model plotted with laboratory data (ε") at 3.4 %NH_3/volume ammonia concentration and temperatures of 20.7 and 3.0 degrees Celsius.

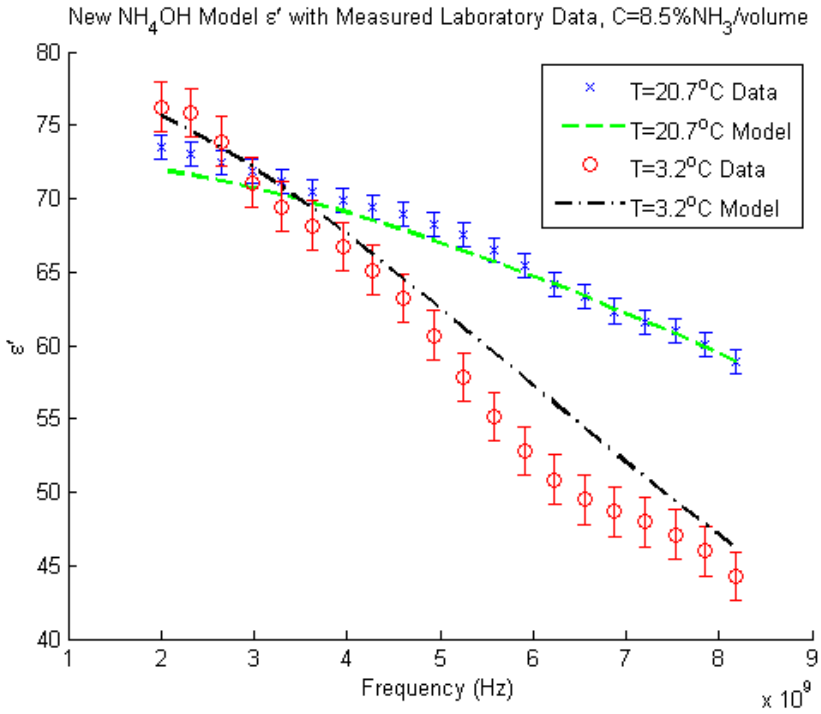

Figure 29. New model plotted with laboratory data (ε') at 8.5 %NH_3/volume ammonia concentration and temperatures of 20.7 and 3.2 degrees Celsius.

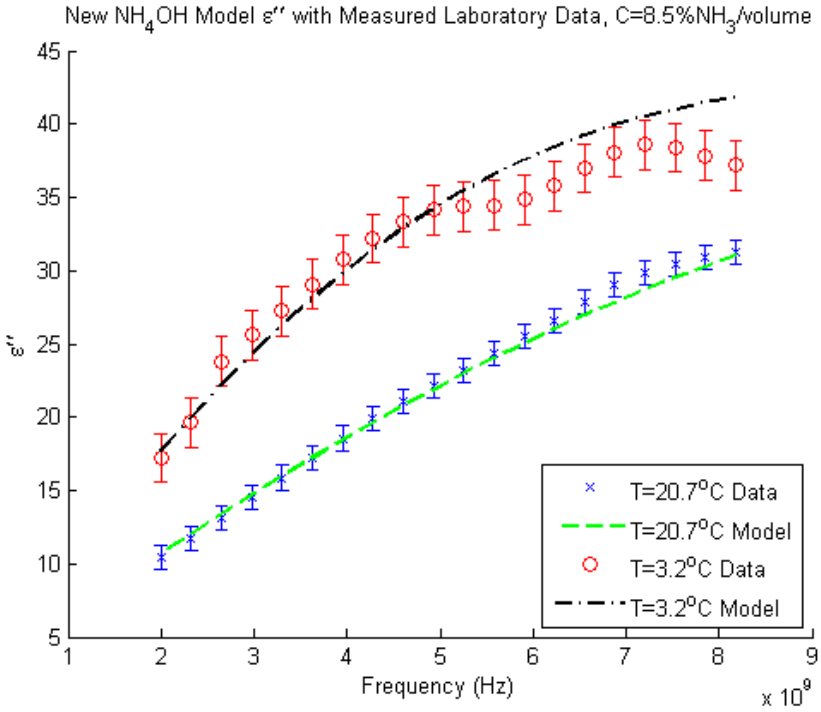

Figure 30. New model plotted with laboratory data (ε") at 8.5 %NH_3/volume ammonia concentration and temperatures of 20.7 and 3.2 degrees Celsius.

4.3 New Model for the Complex Dielectric Constant of NH_4OH

The new model for the complex dielectric constant of NH_4OH is presented as

$$\varepsilon(T,S)=\frac{\varepsilon_s(T,S)-\varepsilon_1(T,S)}{1+j\cdot\frac{\nu}{\nu_1(T,S)}}+\frac{\varepsilon_1(T,S)-\varepsilon_\infty(T,S)}{1+j\cdot\frac{\nu}{\nu_2(T,S)}}+\varepsilon_\infty(T,S)-j\cdot\frac{\sigma(T,S)}{(2\cdot\pi\cdot\varepsilon_0)\cdot\nu}+\Delta_{NH_3}(C,f,T), \quad (4.10)$$

where $j=\sqrt{-1}$, $S=0$, $\sigma(T,S=0)=0$, and

$$\varepsilon_s(T,S)=\frac{3.70886\cdot10^4-8.2168\cdot10^1\cdot T}{4.21854\cdot10^2\cdot T}, \quad (4.11)$$

$$\varepsilon_1(T,S=0)=x_0+x_1\cdot T+x_2\cdot T^2, \quad (4.12)$$

$$\nu_1(T,S=0)=\frac{45+T}{x_3+x_4\cdot T+x_5\cdot T^2}, \quad (4.13)$$

$$\varepsilon_\infty(T,S=0)=x_6+x_7\cdot T, \quad (4.14)$$

$$\nu_2(T,S=0)=\frac{45+T}{x_8+x_9\cdot T+x_{10}\cdot T^2}, \quad (4.15)$$

$$\Delta_{NH_3}(C,f,T)=\frac{x_{11}\cdot C\cdot\nu^{x_{12}}}{T^{x_{13}}}+j\cdot\left(\frac{x_{14}\cdot C\cdot\nu^{x_{15}}}{T^{x_{16}}}+x_{17}\cdot C\right), \quad (4.16)$$

The new model fits laboratory data between 2-8.5 GHz, temperatures between 0-25 °C (273 -298 K), and ammonia concentrations of 0-8.5 %NH_3/volume. The model is an extension of Meissner and Wentz's model of the complex dielectric constant of pure water (2004). Equations 4.11-4.15 are identical to the original Meissner and Wentz

equations presented in chapter II (equations 2.6-2.10). However, the new model incorporates the new parameter $\Delta_{NH_3}(C, f, T)$ which is only non-zero if the concentration is non-zero ($C \neq 0$), and thus, the new model is identical to the Meissner and Wentz model when the ammonia concentration is zero.

4.4 Determining Absolute Input Parameter Bounds

A sensitivity study was performed to ensure that the new model is robust enough to operate outside of the measured temperature and ammonia concentration ranges. At the highest concentration measured, C = 8.5 %NH_3/volume, the new model does not show any irregularities for temperatures up to 525 K as shown in Figures 31 and 32.

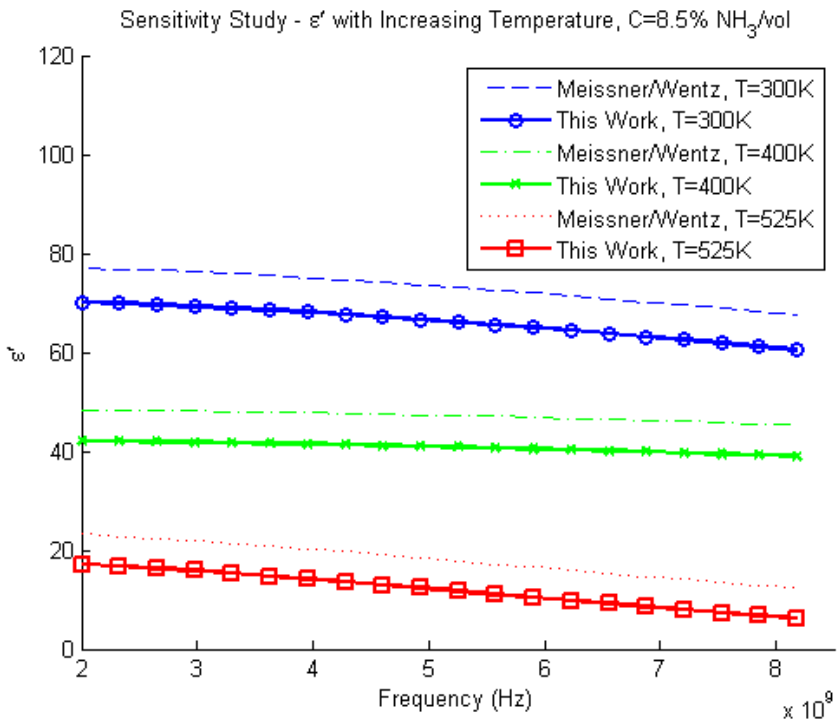

Figure 31. Sensitivity study for upper temperature boundary when concentration is maintained at 8.5 %NH_3/volume.

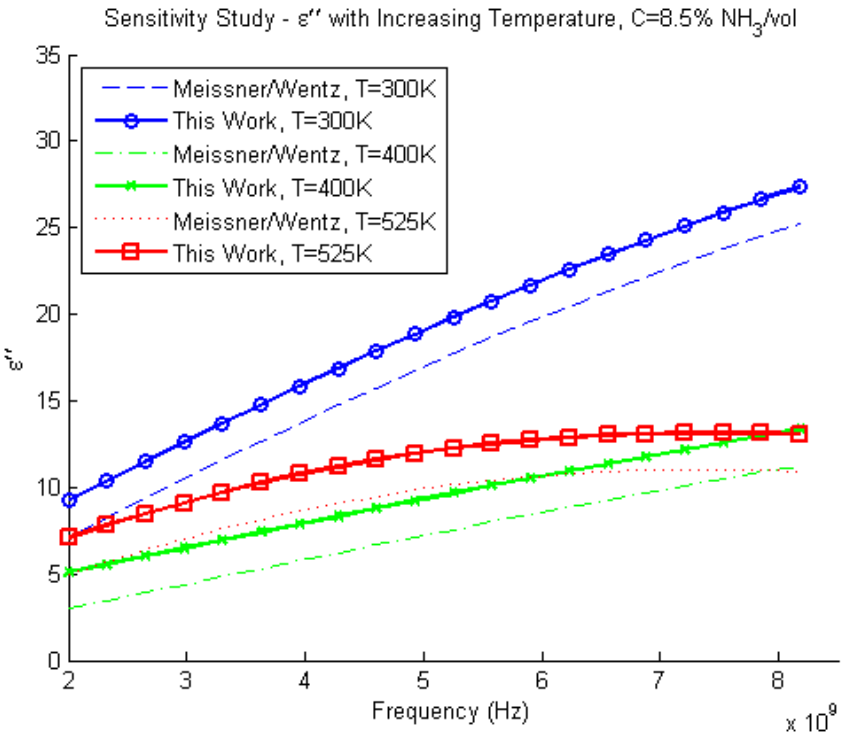

Figure 32. Sensitivity study for upper temperature boundary when concentration is maintained at 8.5 %NH_3/volume.

However, the conditional uncertainties associated with these extreme limits become too large to guarantee accuracy in the model.

When temperature is maintained at 300 K, the upper limit of concentration is tested and the results are shown in Figures 33 and 34.

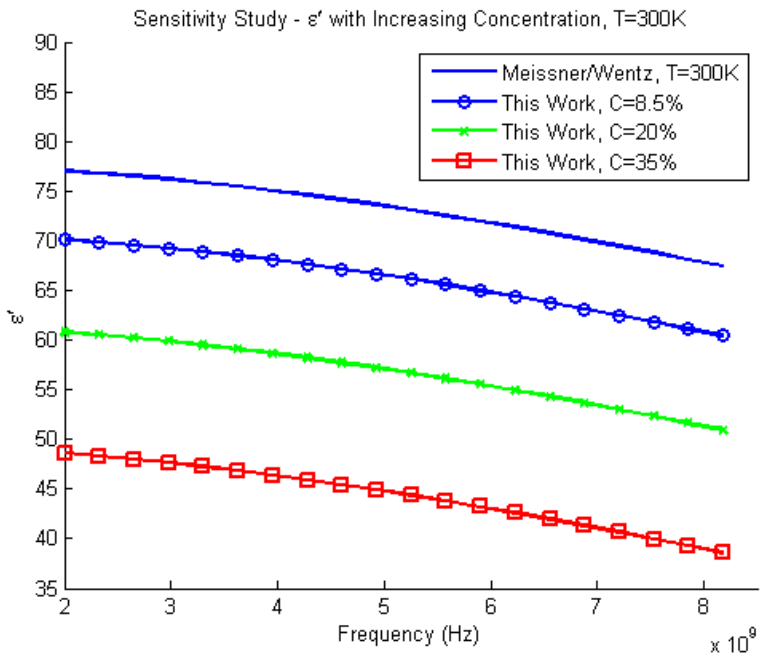

Figure 33. Sensitivity study for upper concentration boundary on ε' when temperature is maintained at 300 K.

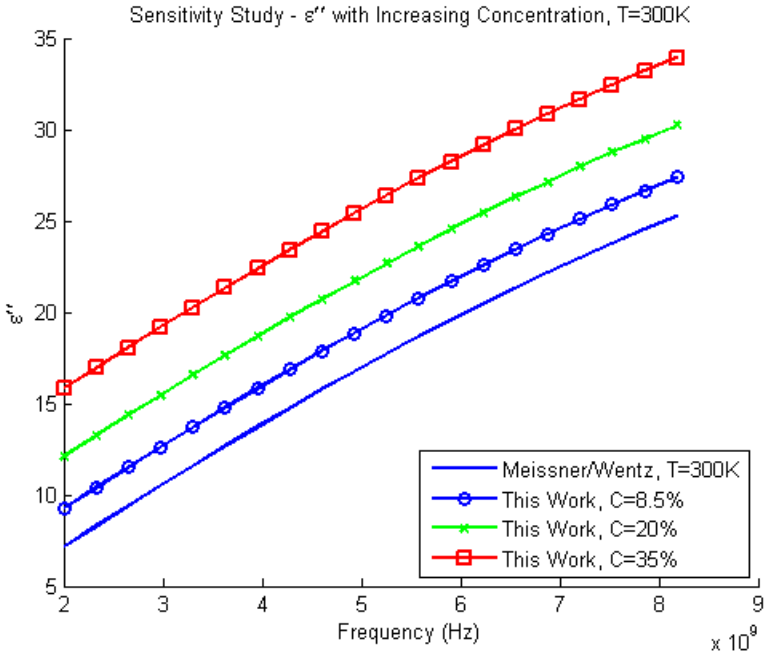

Figure 34. Sensitivity study for upper concentration boundary on ε" when temperature is maintained at 300 K.

The sensitivity study performed when maintaining temperature at 300 K and altering concentration does not show any irregularities up to ammonia concentrations of 35

%NH_3/volume; 35 %NH_3/volume is chosen as the upper test bound on ammonia concentration because it is approximately the aqueous ammonia saturation at room temperatures (LeBlanc *et al.* 1978, Budavari *et al.* 1996). A third sensitivity study was performed to determine the absolute bounds when both varying temperature and concentration: the results of the study are shown in Figures 35 and 36.

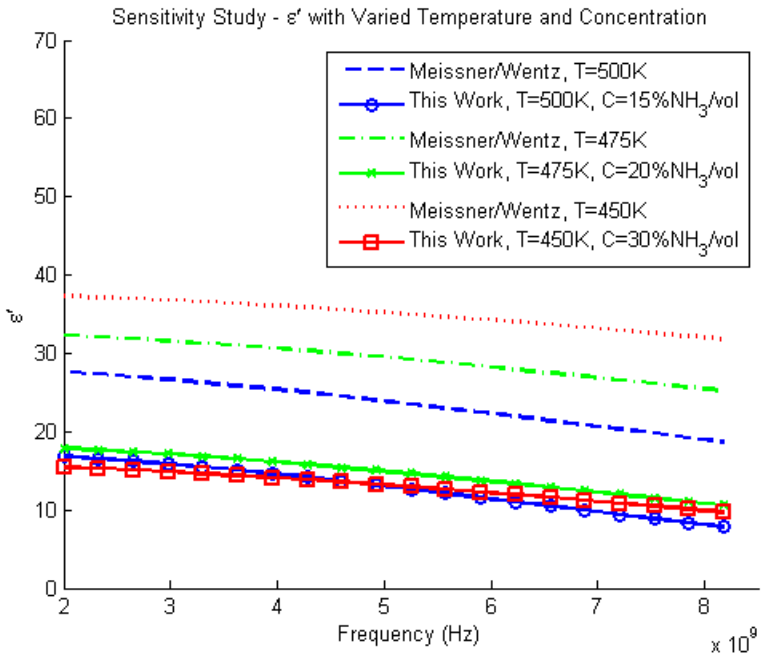

Figure 35. Sensitivity study on ε' to determine absolute bounds on temperature and concentration.

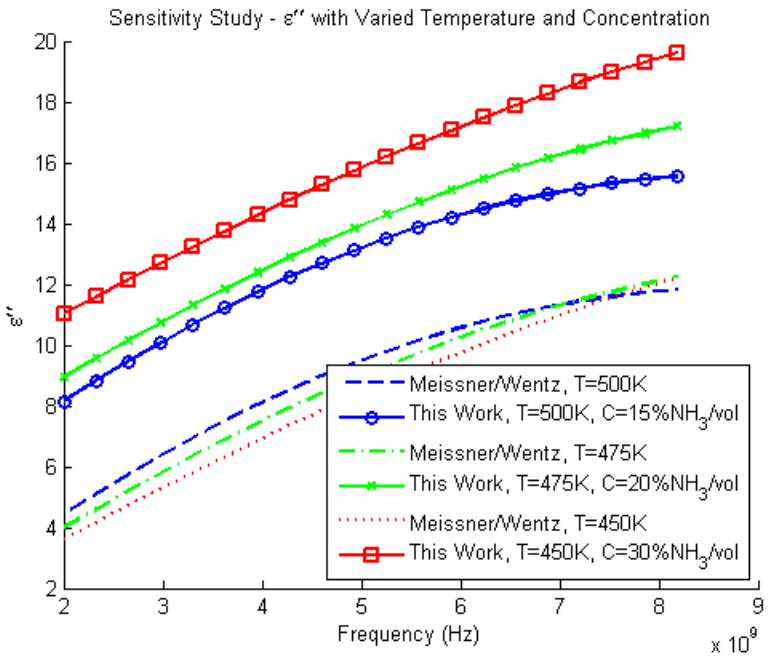

Figure 36. Sensitivity study on ε" to determine absolute bounds on temperature and concentration.

Due to large uncertainties associated with high ammonia concentrations, the absolute upper bound on concentration is set to 20 $\%NH_3$/volume. Similarly the absolute upper bound on temperature is set to 475 K. Accuracy of the new model using parameters greater than these absolute upper bounds on temperature and concentration are not guaranteed.

Chapter V

Summary and Conclusions

With the recent launch of NASA's Juno probe to Jupiter, knowledge of the complex dielectric properties of aqueous ammonia will be important to characterizing the jovian clouds. Discussions of the model, remote sensing applications to the Juno mission, and suggestions for future work are presented below.

5.1 Significant Results

No model for the complex dielectric constant of aqueous ammonia has been previously developed, and thus, these results are a significant increase in the understanding of the true electromagnetic properties of NH_4OH.

The new model for the complex dielectric constant of aqueous ammonia is able to fit 60.26% of the laboratory data within 2σ uncertainty. The bounds verified by laboratory data are set to frequencies between 2-8.5 GHz, temperatures between 0-24 °C (273-297 K), and concentrations between 0-8.5 $\%NH_3$/volume. The sensitivity study performed showed no irregularities up to temperatures and concentrations of 202 °C (475 K) and 20 $\%NH_3$/volume, respectively; the results of the model from input parameters greater than these absolute bounds are not guaranteed.

5.2 Application to Juno

NASA's Juno mission to Jupiter employs a six-channel (0.6, 1.25, 2.6, 5.2, 10, and 22 GHz) microwave radiometer called the MWR (Pingree 2008). The spacecraft will enter a highly elliptical polar orbit with a perijove of 1.06 R_J (4,500 km) to pass under Jupiter's synchrotron radiation belts (Matousek 2005). The new aqueous ammonia model is of particular importance for the 2.6 and 5.2 GHz MWR channels. Based on analyses of the DeBoer-Steffes models for mean jovian conditions shown in Figures 37 and 39 (see e.g., DeBoer and Steffes 1996, Karpowicz 2010) and abundance estimates for NH_3 and H_2O shown in Figure 38 (Karpowicz 2010), it is determined that under the most generous estimates, aqueous ammonia clouds are only able to form at temperatures at or below ~325 K.

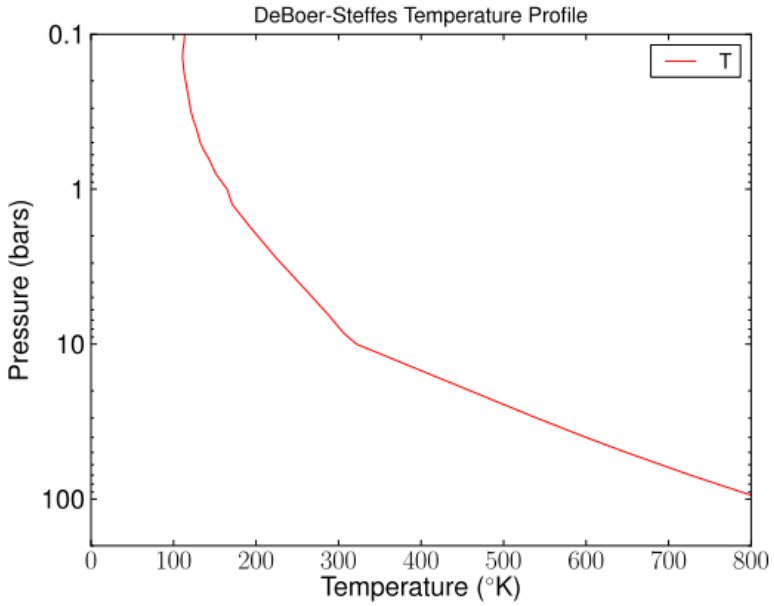

Figure 37. DeBoer-Steffes TP profile under mean jovian conditions.

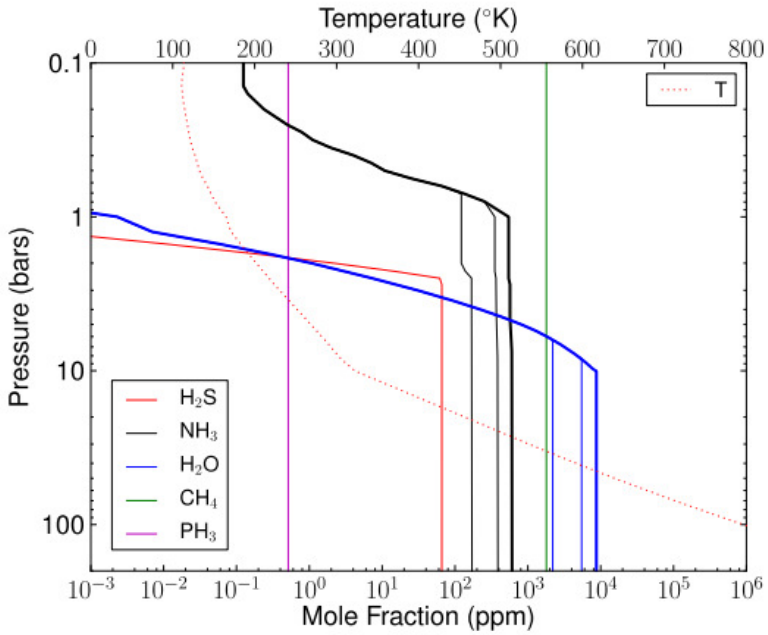

Figure 38. Constituent abundance profile and DeBoer-Steffes TP profile. Line weight denotes depleted, mean, and enhanced abundance conditions.

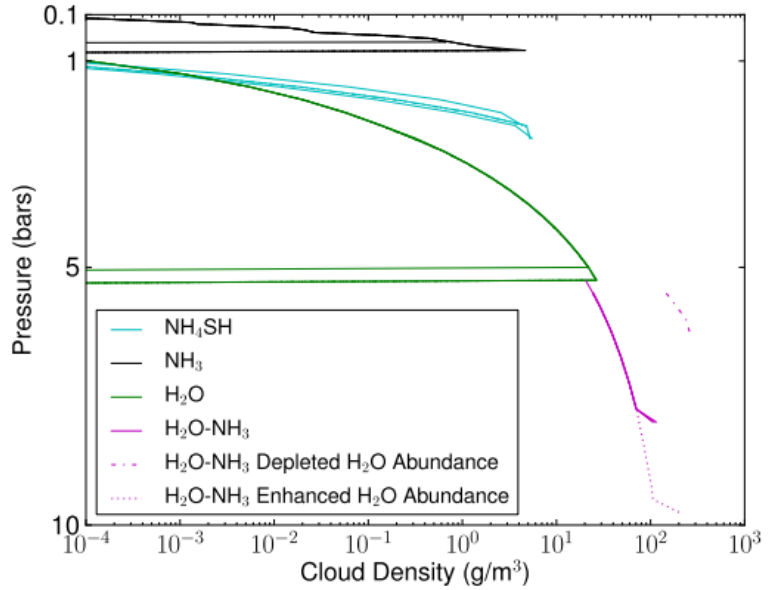

Figure 39. Cloud densities under various jovian conditions.

Given the bounds on the environmental conditions surrounding cloud formation and the estimates on constituent abundances, the new aqueous ammonia model is valid for use in modeling jovian cloud opacity.

As no model for the complex dielectric properties of aqueous ammonia previously existed, the values of water were used as a substitute when estimating the cloud opacity of these types of clouds under jovian conditions. It is thus useful to determine the difference in the cloud opacity when using values calculated for water versus values calculated using the new model. Assuming Rayleigh scattering, the cloud opacity is obtained from the volume extinction coefficient approximated by (Battan 1973),

$$\alpha_{cloud} = \frac{246 \cdot M \cdot \varepsilon''}{\rho \cdot \lambda \cdot [(\varepsilon'+2)^2 + (\varepsilon'')^2]} \text{ dB/km}, \tag{5.1}$$

where M is the cloud bulk density, ρ is the density of the liquid (water or aqueous ammonia) in the same units, λ is the wavelength in km, and ε' and ε" are the real and imaginary components, respectively, of the dielectric constant of the liquid.

The density of the liquid, ρ, varies depending on the temperature and concentration of ammonia for aqueous ammonia solutions, and estimates of the cloud bulk density, M, are available for the jovian model (see e.g. Figure 39, Karpowicz 2010). However, assuming the parameters M and ρ to be constant, a percent difference in the cloud attenuation can be calculated using the values of ε' and ε" calculated for water versus those calculated using the new aqueous ammonia model as shown in Figure 40.

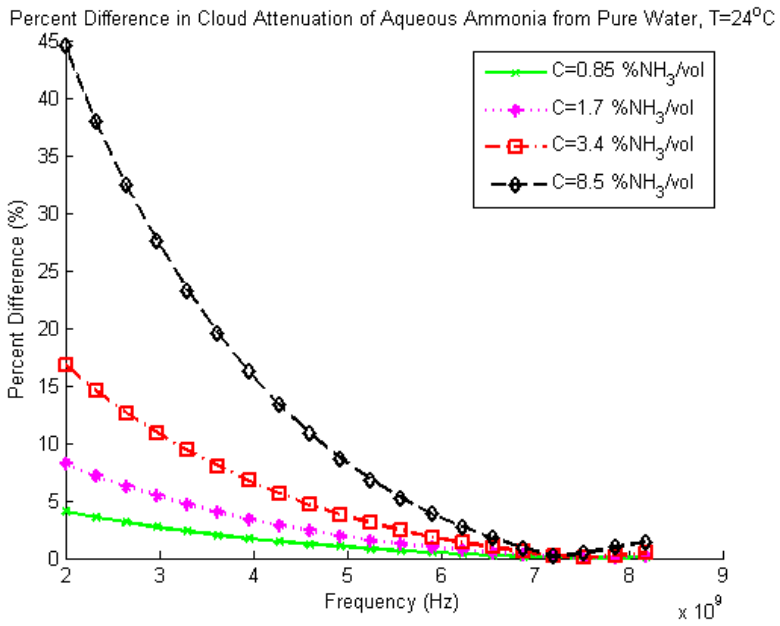

Figure 40. Percent difference in α_{cloud} using the new model versus pure water; assumes parameters M and ρ to be constant in the volume extinction coefficient approximation.

As shown in Figure 40, there is a significant difference in the α_{cloud} from aqueous ammonia versus that of water. As this is only a percentage difference, the magnitude of this effect will not be known until the true values for the parameters M and ρ can be applied to the calculation of the volume extinction coefficient in equation 5.1. However, it is significant that there is a difference in α_{cloud} from aqueous ammonia versus α_{cloud} from water.

Current estimates of the dissolved ammonia abundance in the jovian water cloud are between 2-3%. The most generous bulk density estimates of water clouds with dissolved ammonia reach values of M = 300 g/m^3 as shown in Figure 40. The jovian ammonia cloud opacity based on reasonable estimates of cloud bulk density in the range between 100 to 200 g/m^3 and varied concentrations between 2 and 3 %NH_3/volume as shown in

Figures 41-43. The temperature is 300 K, and the density, ρ, used in equation 5.1 is a linear combination of the aqueous ammonia density (ρ_{NH4OH} = 9.853 E 5 g/m^3) and water density (ρ_{H2O} = 9.970 E 5 g/m^3) based on concentration (Weast 1989).

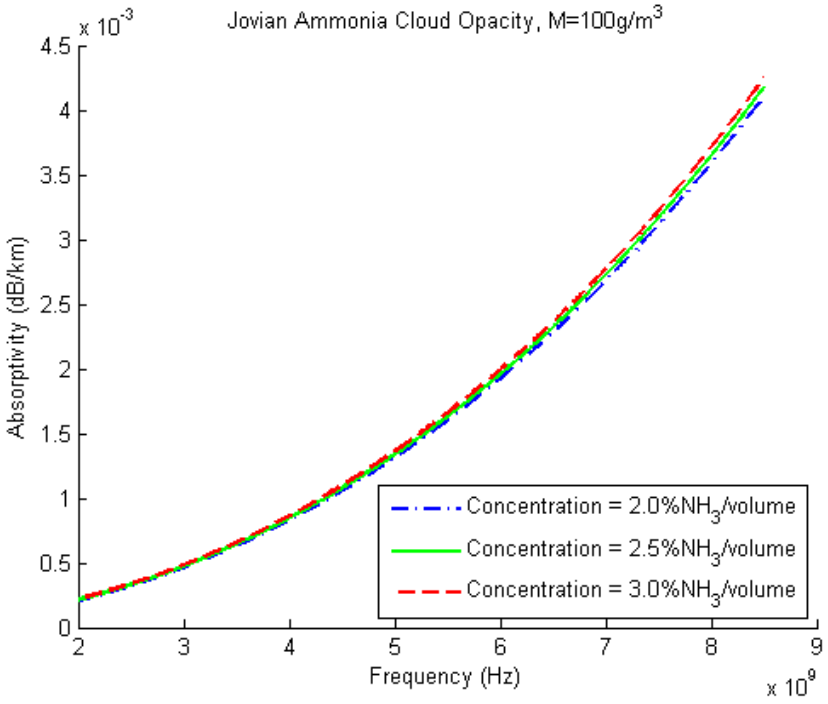

Figure 41. Jovian ammonia cloud opacity at 300 K with concentrations between 2 to 3 %NH_3/volume with a cloud bulk density M=100 g/m^3.

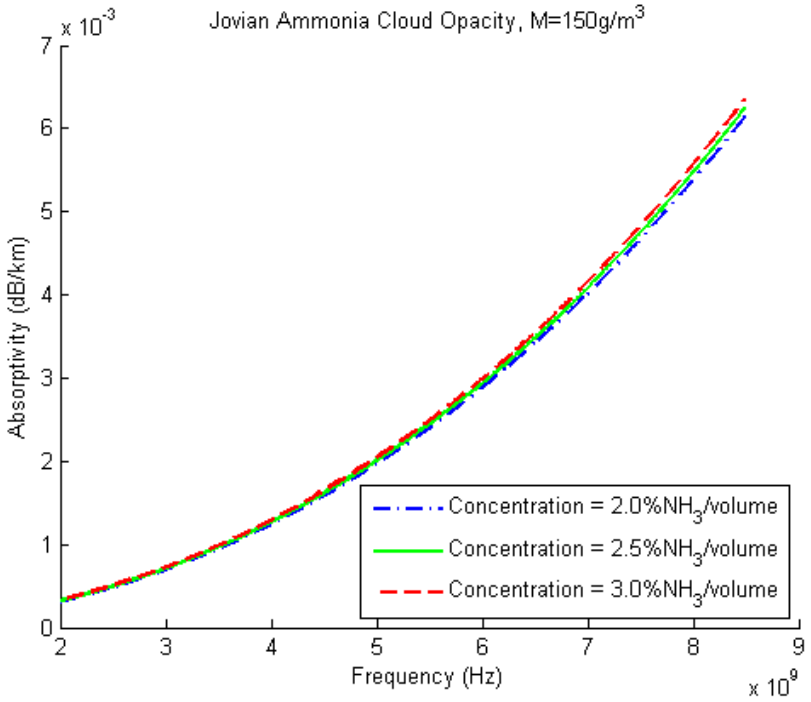

Figure 42. Jovian ammonia cloud opacity at 300 K with concentrations between 2 to 3 $\%NH_3$/volume with a cloud bulk density M=150 g/m^3.

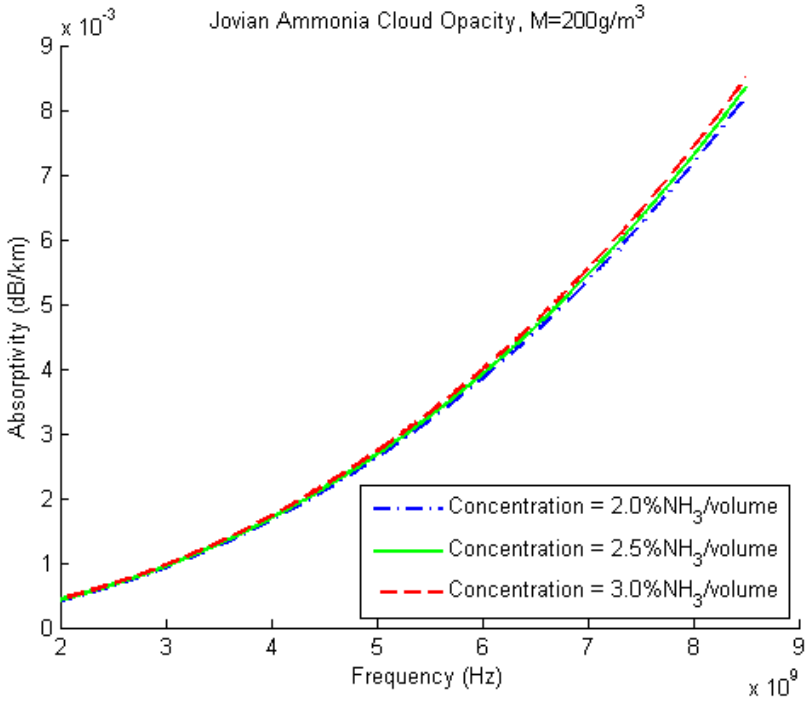

Figure 43. Jovian ammonia cloud opacity at 300 K with concentrations between 2 to 3 $\%NH_3$/volume with a cloud bulk density M=200 g/m^3.

5.3 Suggestions for Future Work

Many improvements can be made to reduce uncertainties associated with both the room-temperature and cold-temperature measurement systems. The Agilent 85070E dielectric probe operates essentially as an open-ended transmission line, which in the case of this work, is submerged in a liquid (i.e., pure water or aqueous ammonia). The probe assumes enough liquid is present that the medium is largely distributed and appears "infinite" with respect to the probe (Agilent 2006). Samples of 200 mL were used per trial for these laboratory measurements which should be sufficiently large in volume; however, for more confident results a larger volume of liquid could be used. Furthermore, the presence of air bubbles or other air gap effects present on the probe-liquid interface can be a significant source of error in the measurement of the complex dielectric constant. For these laboratory measurements, a visual inspection was performed before each data collection to ensure there were no air bubbles present. A more rigorous test to verify the absence of air bubbles or any such air gap could be employed; furthermore, a more sophisticated apparatus could be machined around the probe to ensure a hermetic seal around the probe and solution under test.

Similarly the cold temperature experiments were performed in a 1.7 cubic foot (0.048 cubic meter) refrigerator. These results exhibited an artificial deviation in ε" at the higher frequencies (greater than 5.5 GHz) which may be attributed to resonances internal to the refrigerator. A sufficiently large refrigerator or sufficiently cold room could be used to mitigate this type of resonance effect.

The probe is susceptible to reflections from nearly any surface, including the aluminum probe stand. Microwave absorbent foam fit to the 200 mL beakers was used as an attempt to mitigate the standing waves present in the room temperature measurements; however, this did not provide any reduction in the prominence of the standing waves. Ideally a sufficiently large ("infinite") source of solution in test would mitigate any type of inadvertent reflections or standing waves present in the system.

As previously mentioned similar laboratory measurements were attempted at higher temperatures (~40 °C) but were abandoned due to a decrease in ammonia concentration during the heating process. These additional measurements would be useful in verifying the new aqueous ammonia model's effectiveness at these temperatures; however, a more robust high temperature measurement system would have to be developed. First a system that is able to heat aqueous ammonia solutions with minimal loss of ammonia concentration is required. 200 mL glass jars with a plastic PTFE-lined lid machined to fit the dielectric probe was used to attempt to mitigate this issue; however, this failed due to a lack of a hermetic seal, and the pressure produced by the outgassing of ammonia was enough to damage the plastic PTFE-lined lid. A strong, machined, hermetically sealed container is a possibility for at least reducing the loss of ammonia concentration. Secondly a system to accurately monitor the ammonia concentration would be beneficial. This is recommended for measurements at all temperatures and not just high temperature measurements. A pH meter was used to roughly monitor the ammonia concentration. This was used to verify that the concentration of ammonia

remained stable for the cold and room temperature experiments. However, this was only useful as a relative measurement of concentration among aqueous ammonia solutions rather than the absolute ammonia concentration.

Appendix A

Complete Laboratory Data

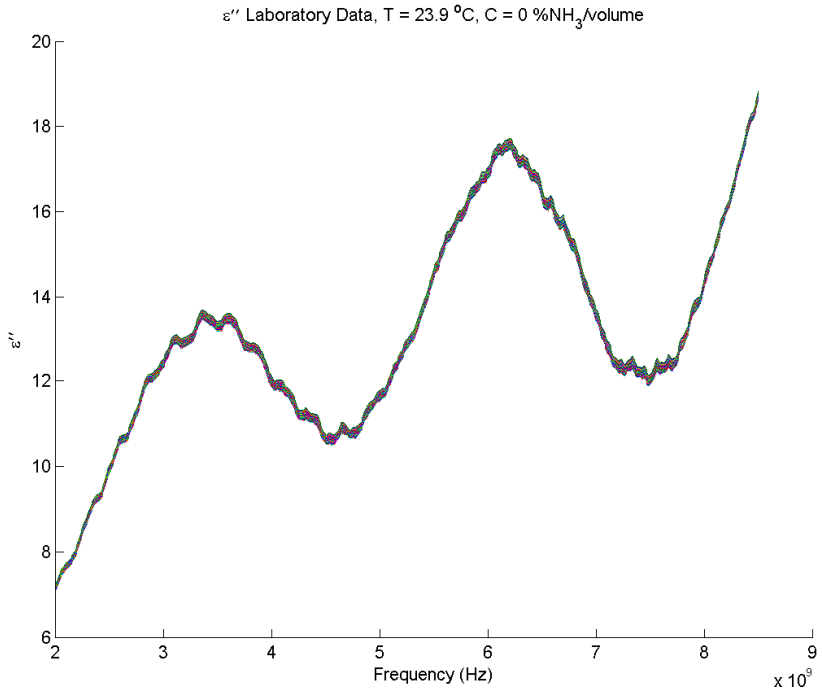

Figure 44. ε" laboratory data set 1 taken on 7/1/2010 - 19:21.

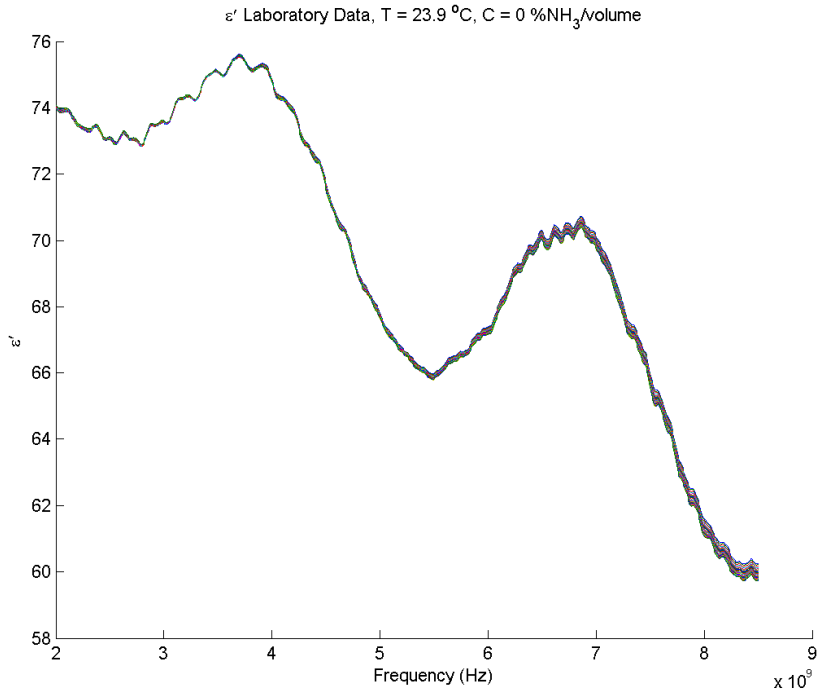

Figure 45. ε' laboratory data set 1 taken on 7/1/2010 - 19:21.

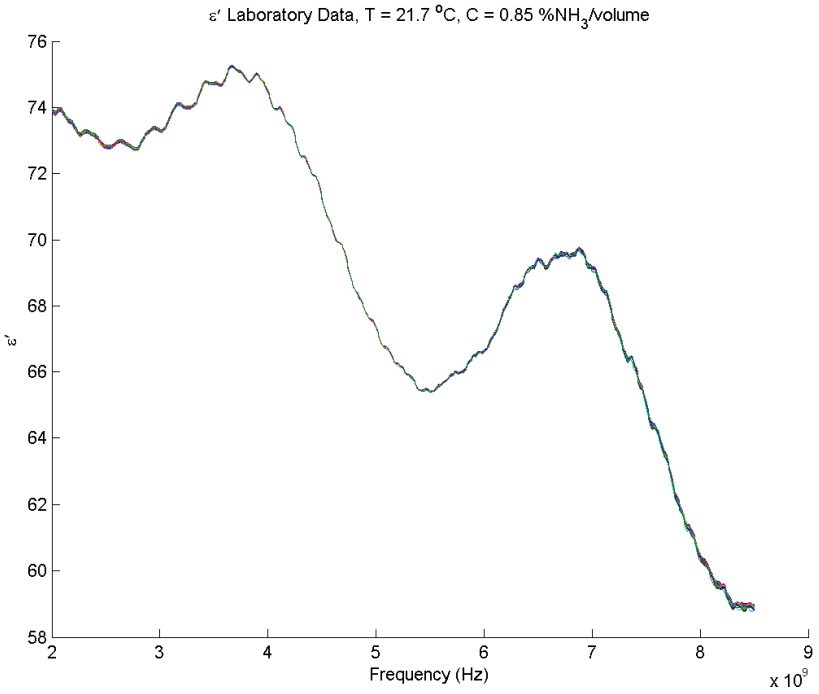

Figure 46. ε" laboratory data set 2 taken on 7/1/2010 - 19:52.

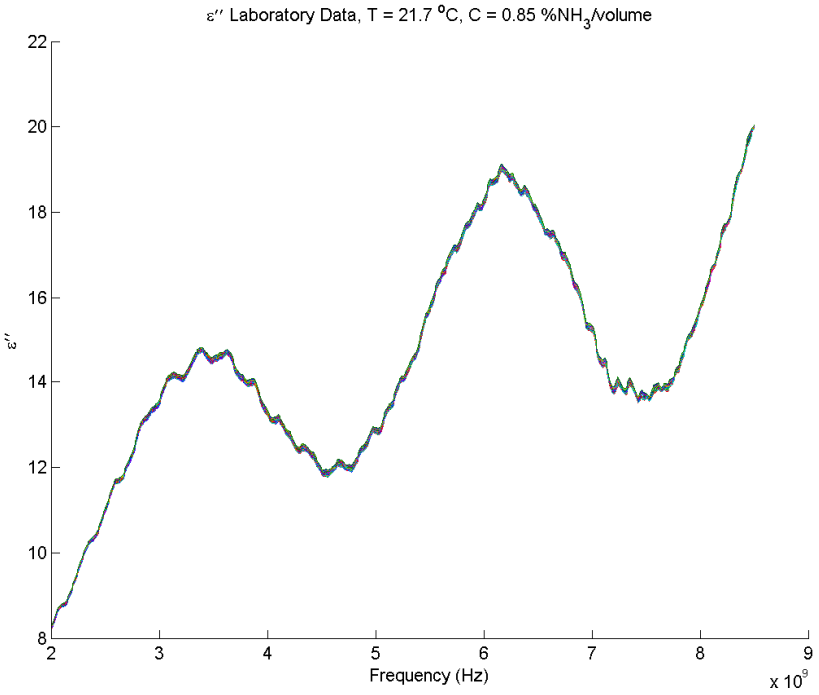

Figure 47. ε' laboratory data set 2 taken on 7/1/2010 - 19:52.

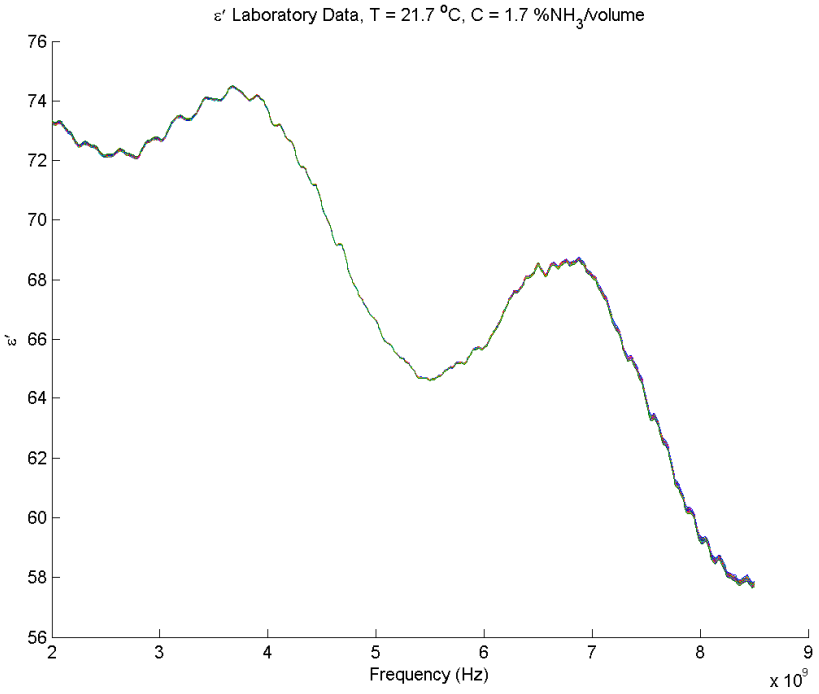

Figure 48. ε" laboratory data set 3 taken on 7/1/2010 - 20:13.

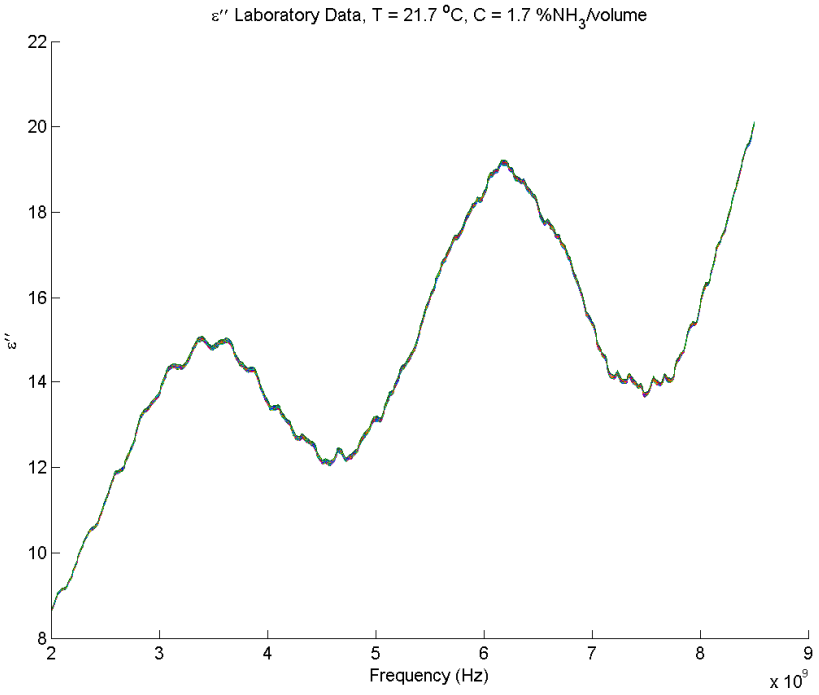

Figure 49. ε' laboratory data set 3 taken on 7/1/2010 - 20:13.

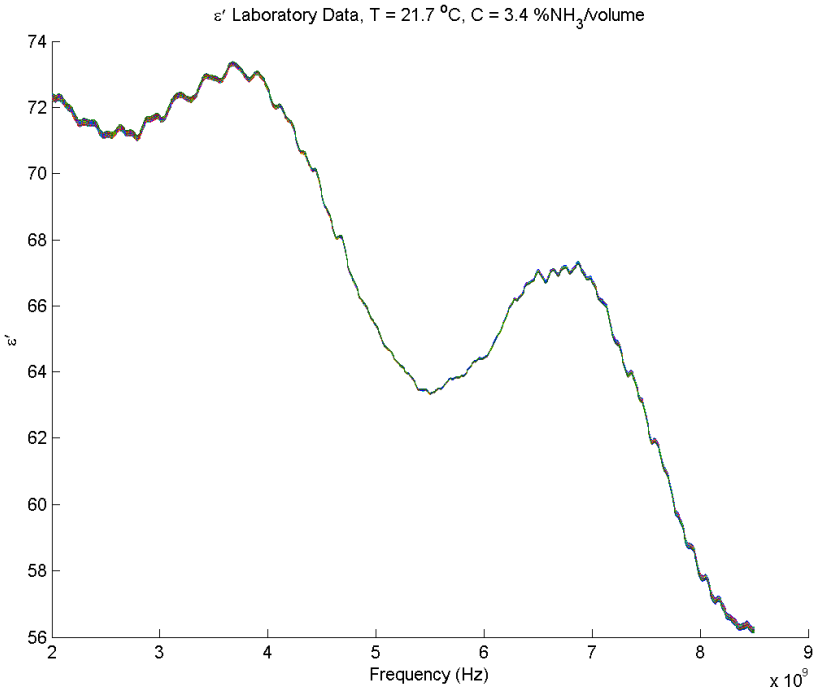

Figure 50. ε" laboratory data set 4 taken on 7/1/2010 - 20:37.

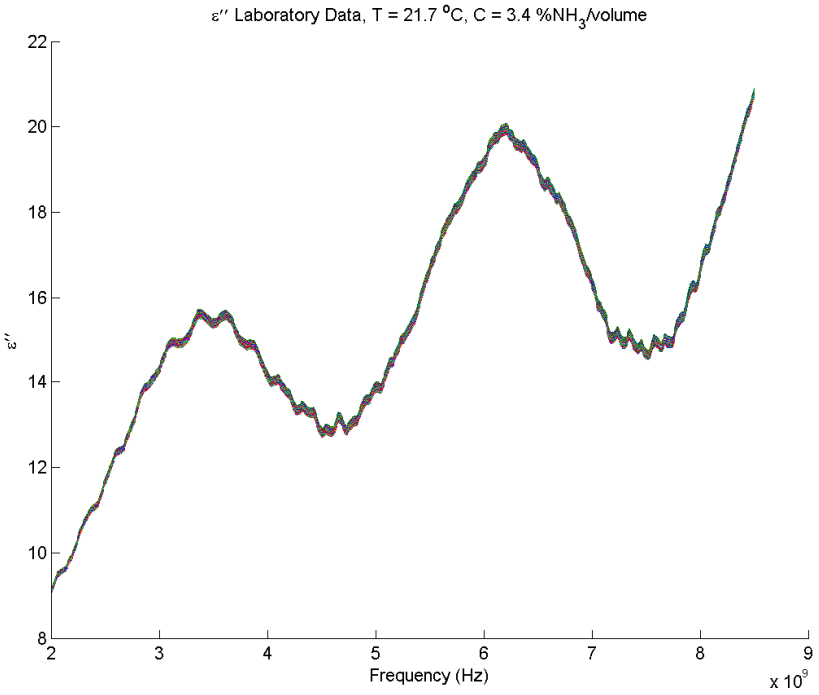

Figure 51. ε' laboratory data set 4 taken on 7/1/2010 - 20:37.

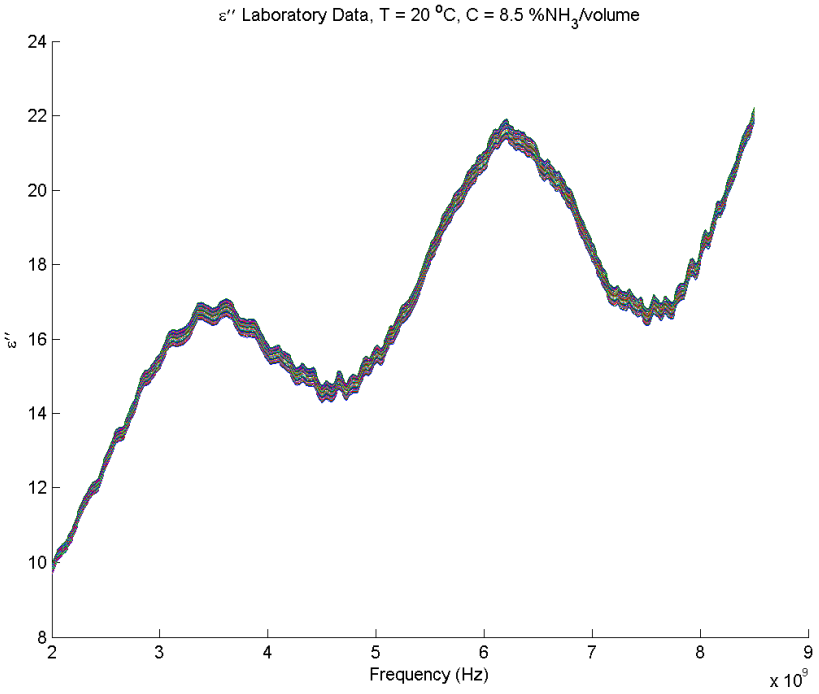

Figure 52. ε" laboratory data set 5 taken on 7/1/2010 - 22:46.

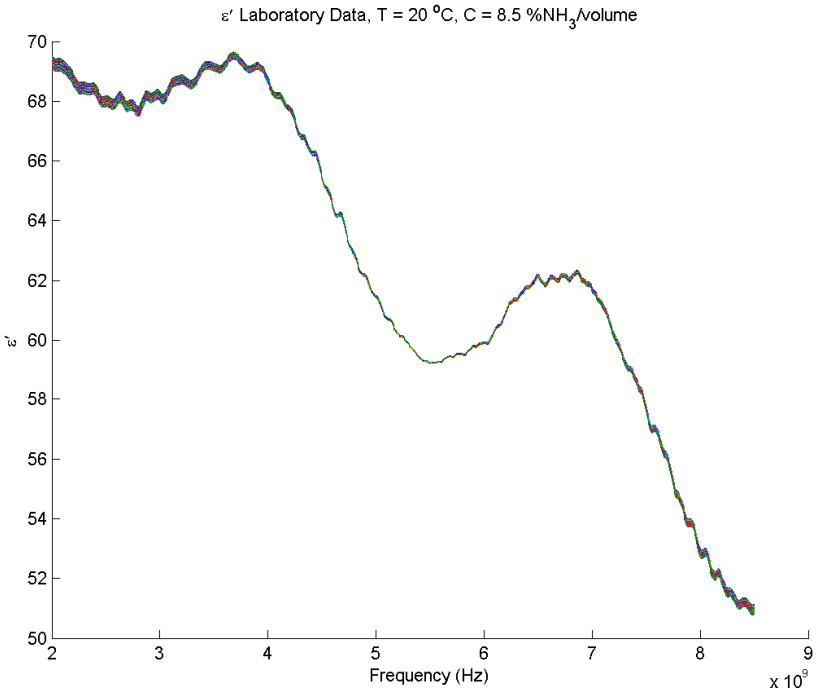

Figure 53. ε' laboratory data set 5 taken on 7/1/2010 - 22:46.

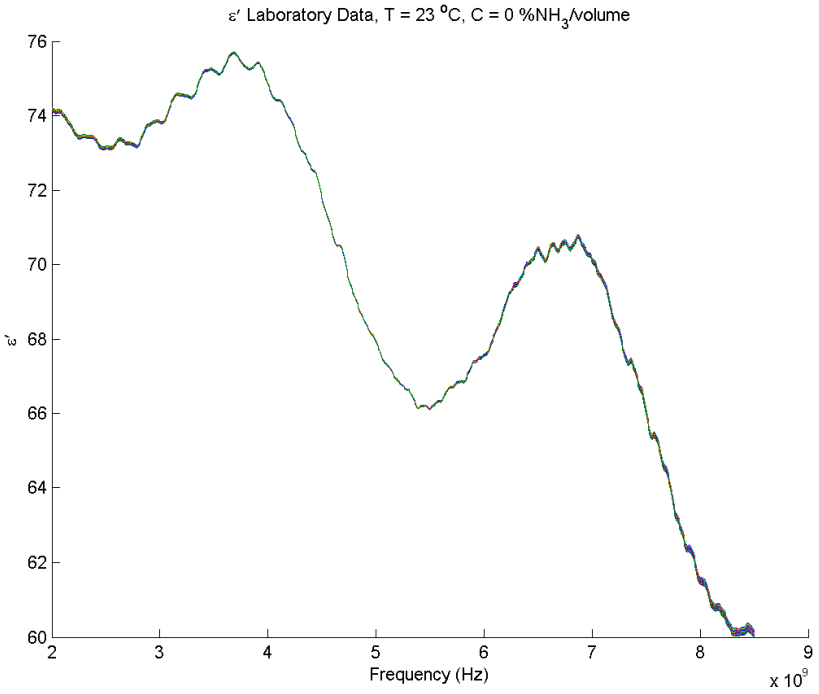

Figure 54. ε" laboratory data set 6 taken on 7/1/2010 - 23:39.

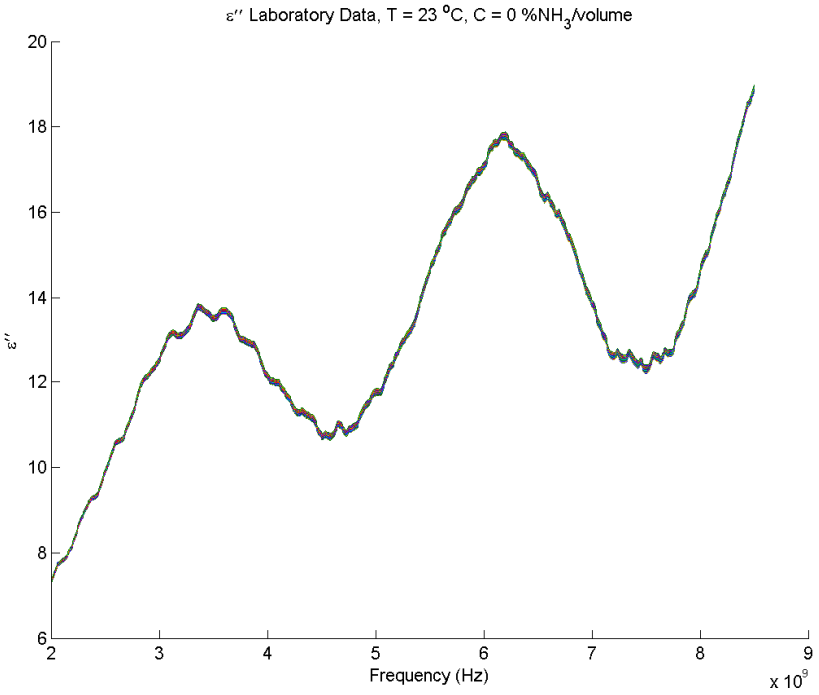

Figure 55. ε' laboratory data set 6 taken on 7/1/2010 - 23:39.

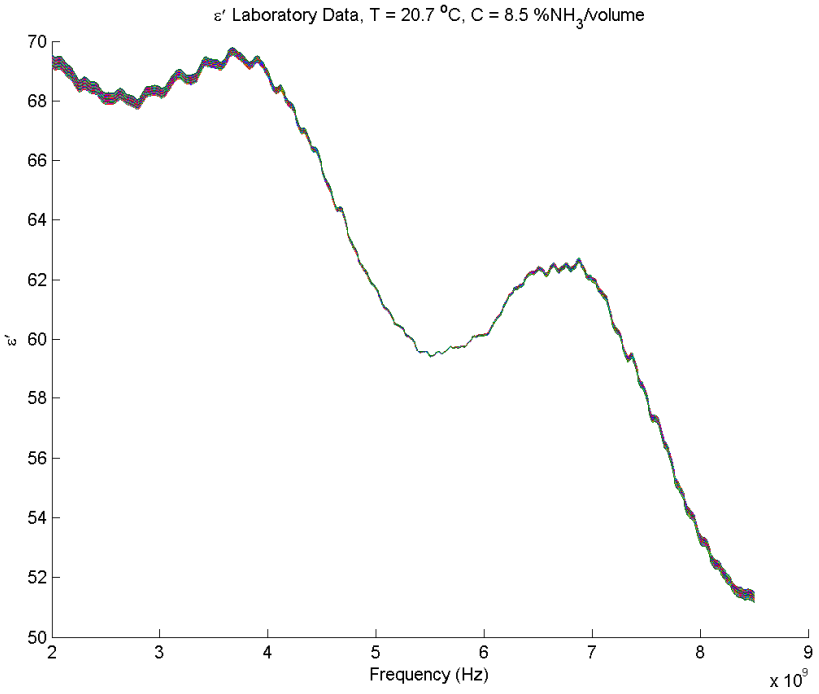

Figure 56. ε" laboratory data set 7 taken on 7/2/2010 - 00:07.

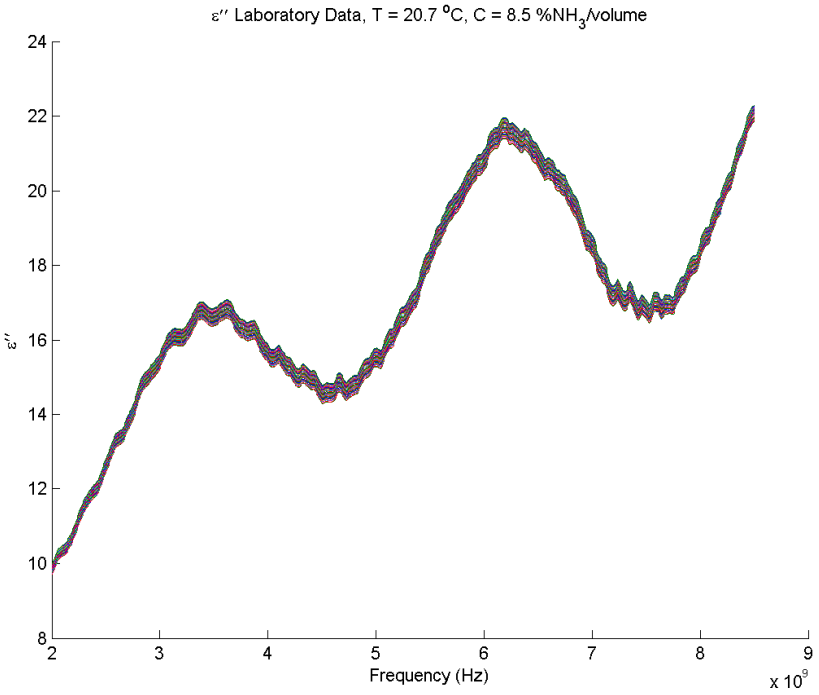

Figure 57. ε' laboratory data set 7 taken on 7/2/2010 - 00:07.

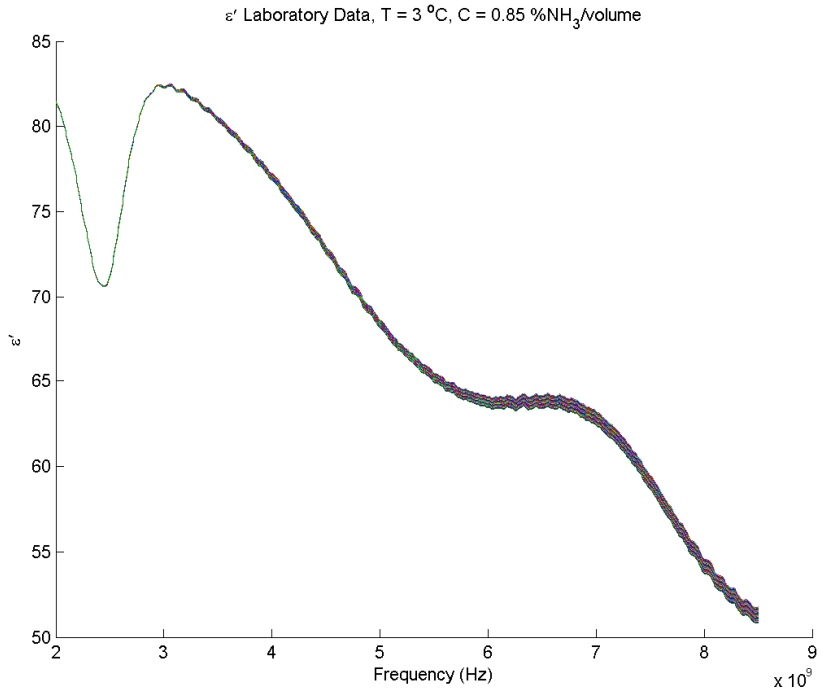

Figure 58. ε" laboratory data set 8 taken on 7/2/2010 - 00:36.

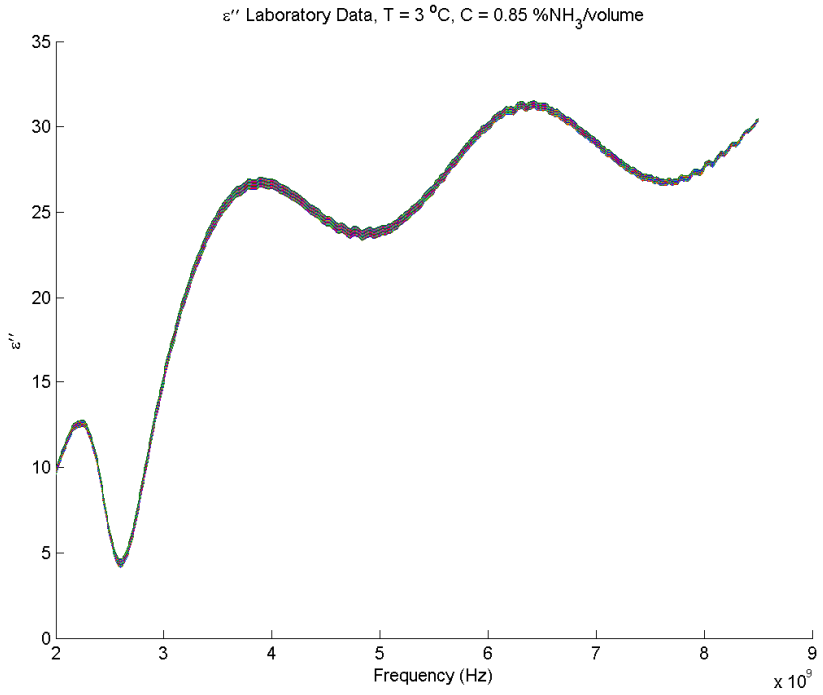

Figure 59. ε' laboratory data set 8 taken on 7/2/2010 - 00:36.

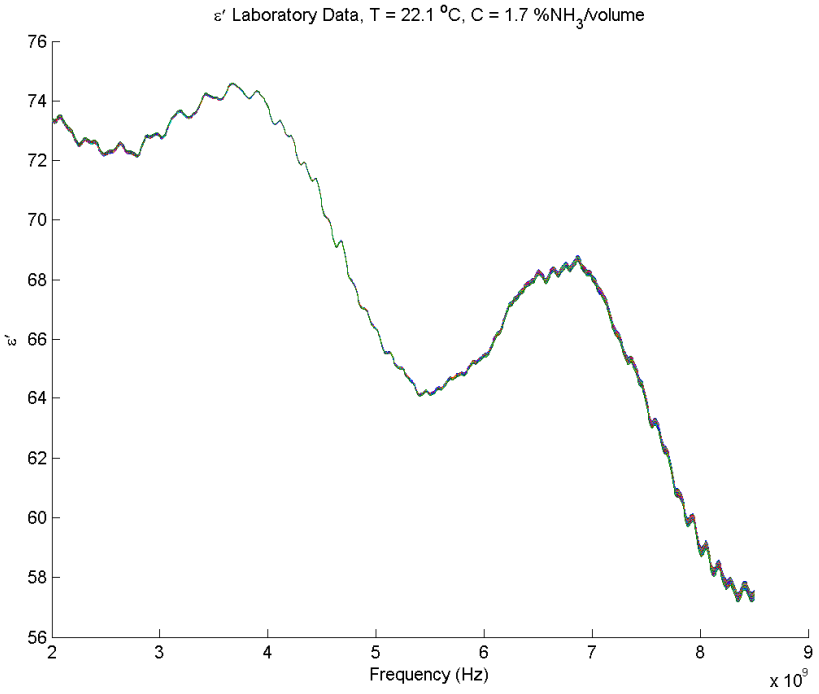

Figure 60. ε" laboratory data set 9 taken on 7/2/2010 - 01:02.

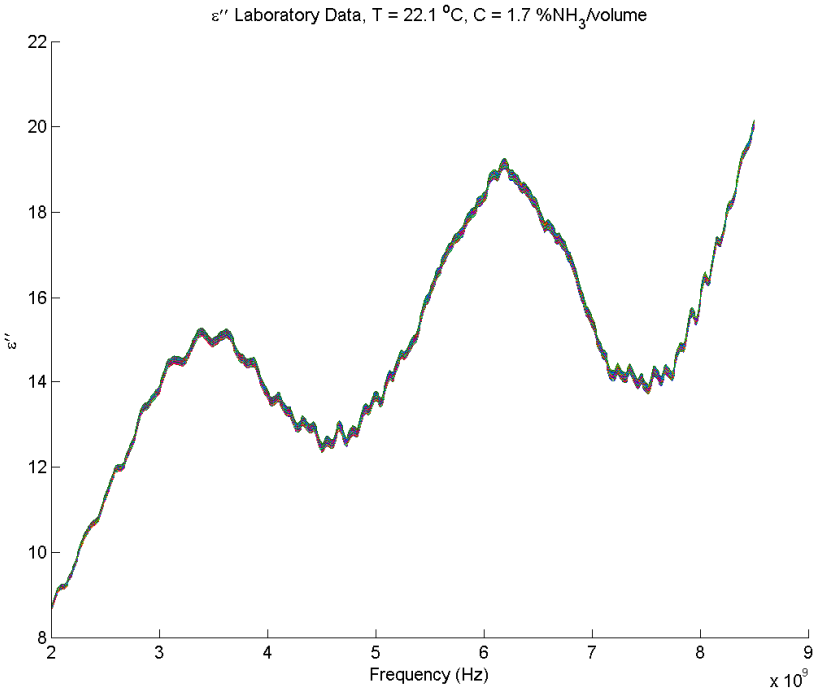

Figure 61. ε' laboratory data set 9 taken on 7/2/2010 - 01:02.

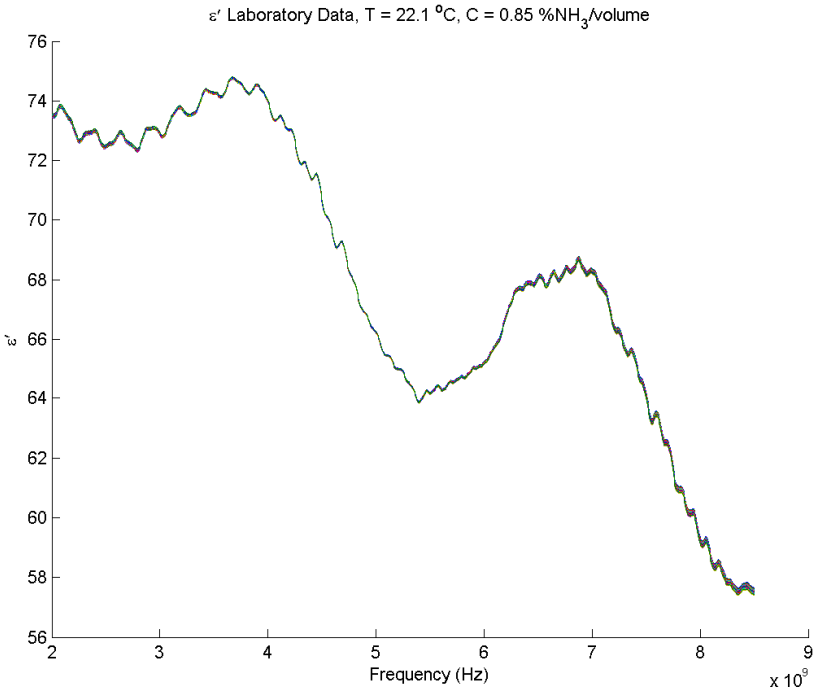

Figure 62. ε" laboratory data set 10 taken on 7/2/2010 - 01:28.

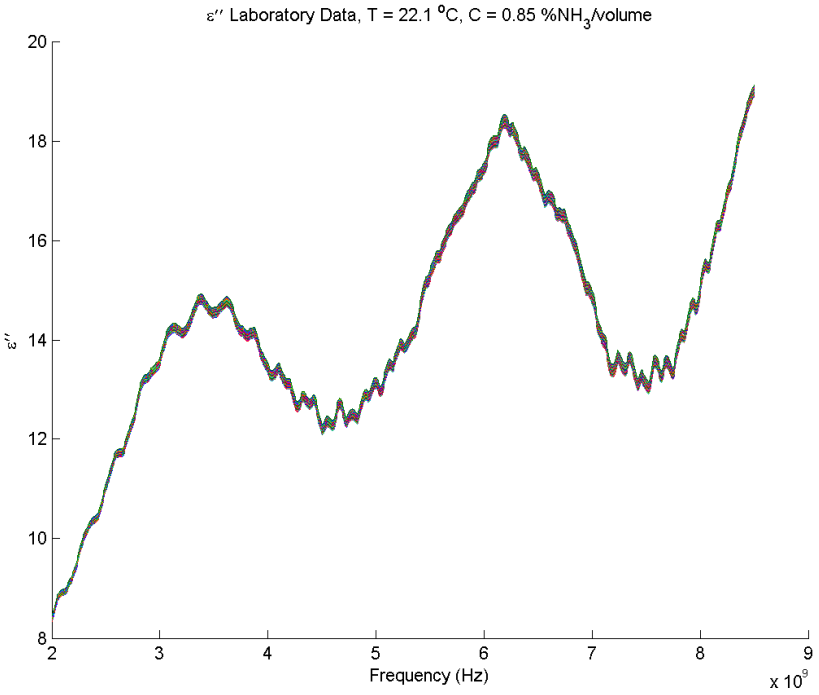

Figure 63. ε' laboratory data set 10 taken on 7/2/2010 - 01:28.

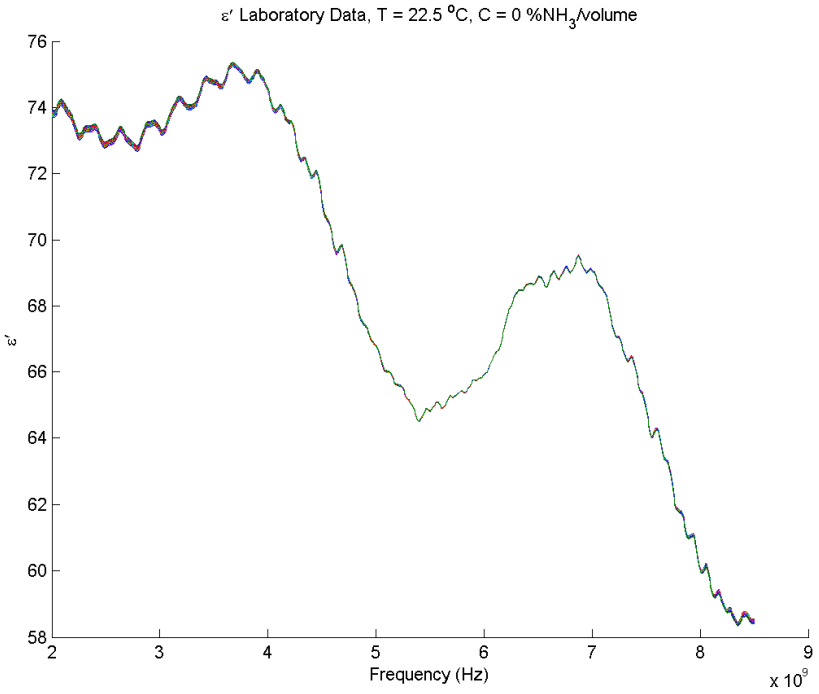

Figure 64. ε" laboratory data set 11 taken on 7/2/2010 - 01:52.

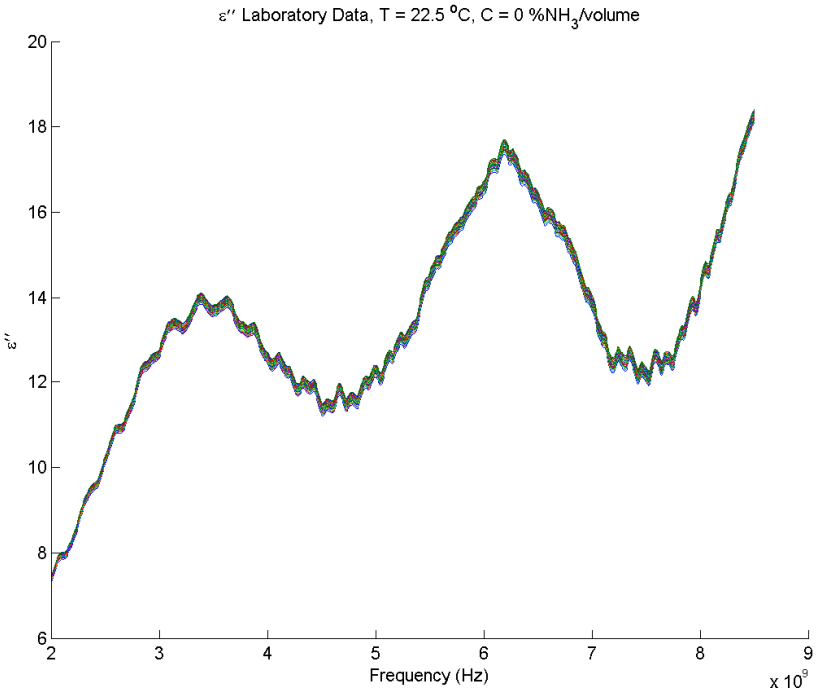

Figure 65. ε' laboratory data set 11 taken on 7/2/2010 - 01:52.

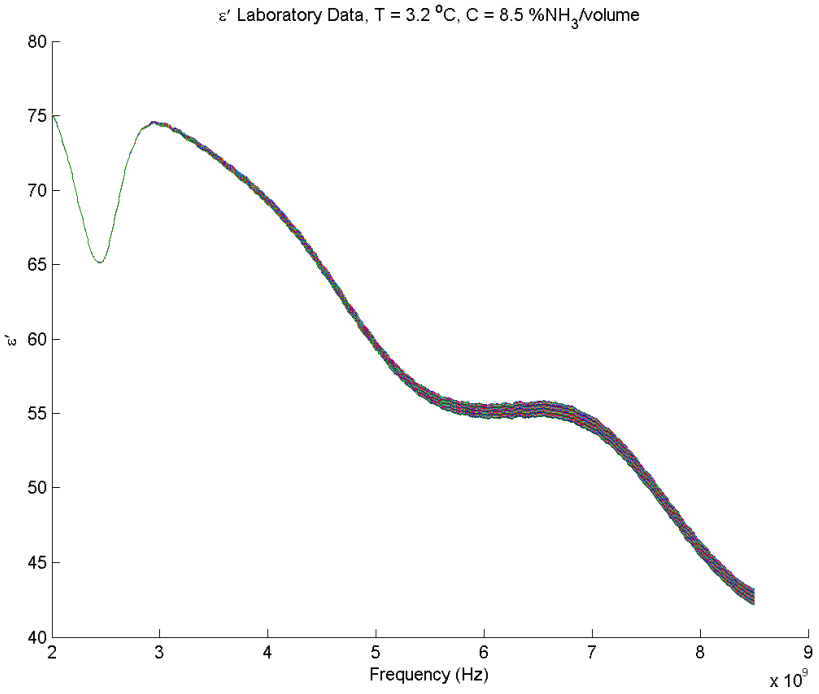

Figure 66. ε" laboratory data set 12 taken on 1/7/2011 - 01:21.

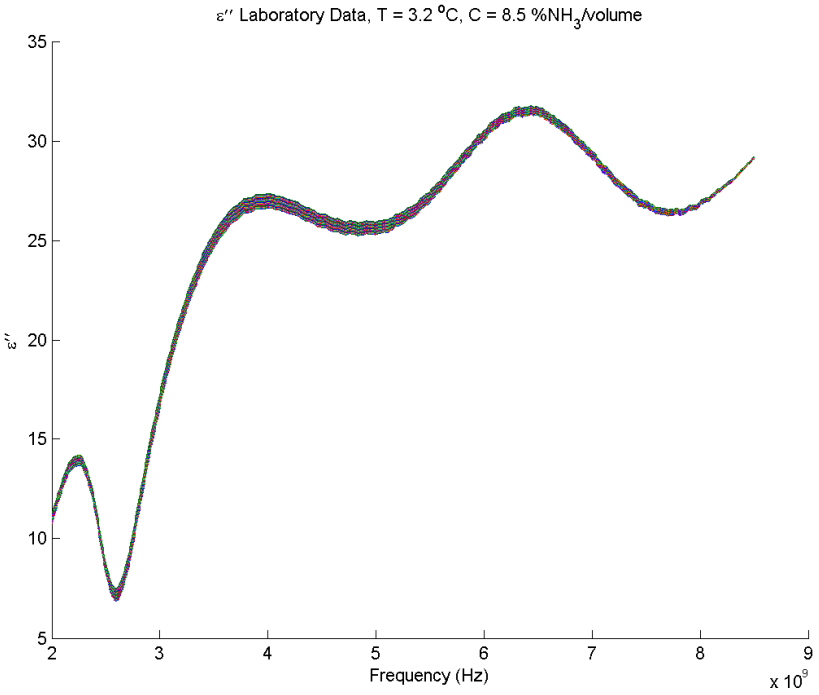

Figure 67. ε' laboratory data set 12 taken on 1/7/2011 - 01:21.

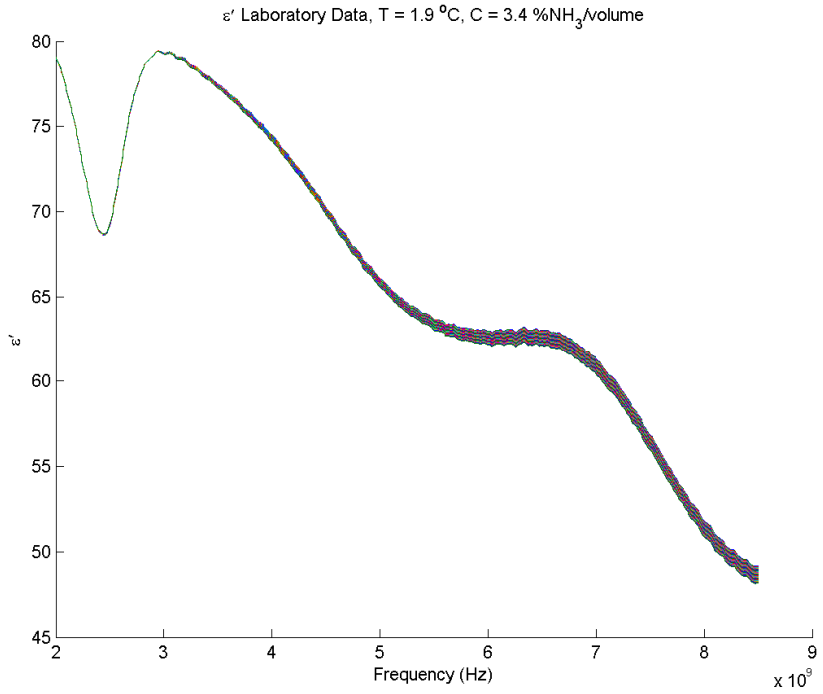

Figure 68. ε" laboratory data set 13 taken on 1/7/2011 - 02:10.

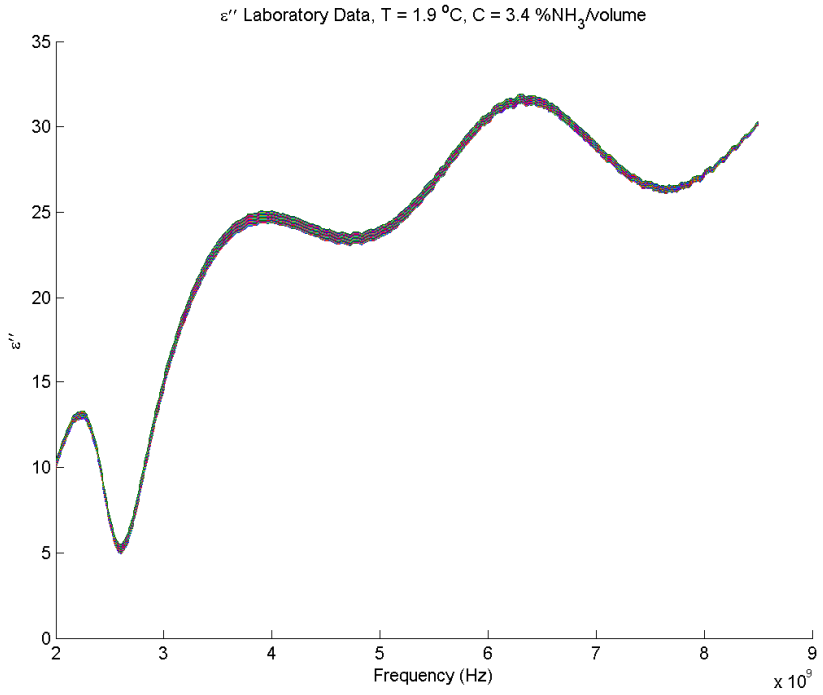

Figure 69. ε' laboratory data set 13 taken on 1/7/2011 - 02:10.

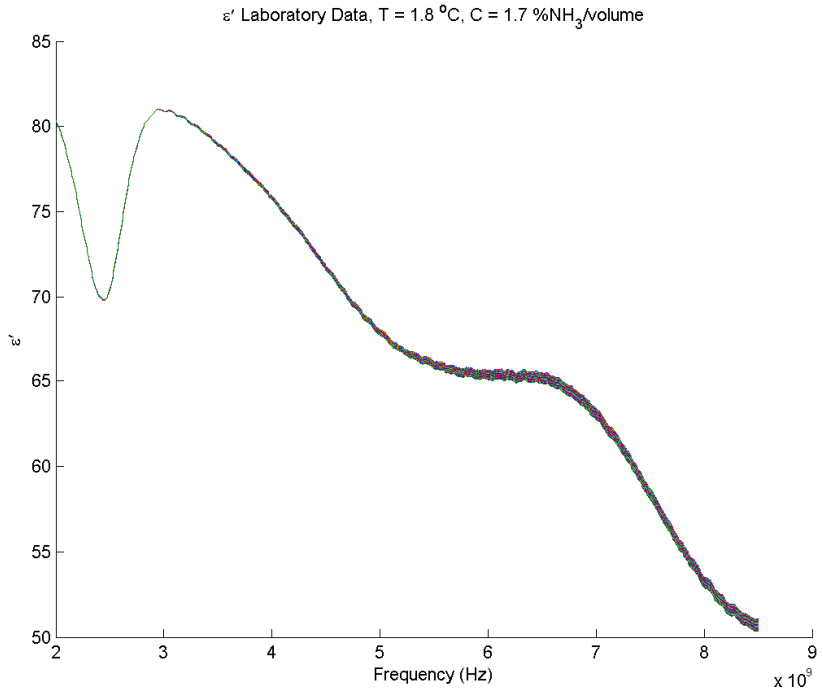

Figure 70. ε" laboratory data set 14 taken on 1/7/2011 - 03:02.

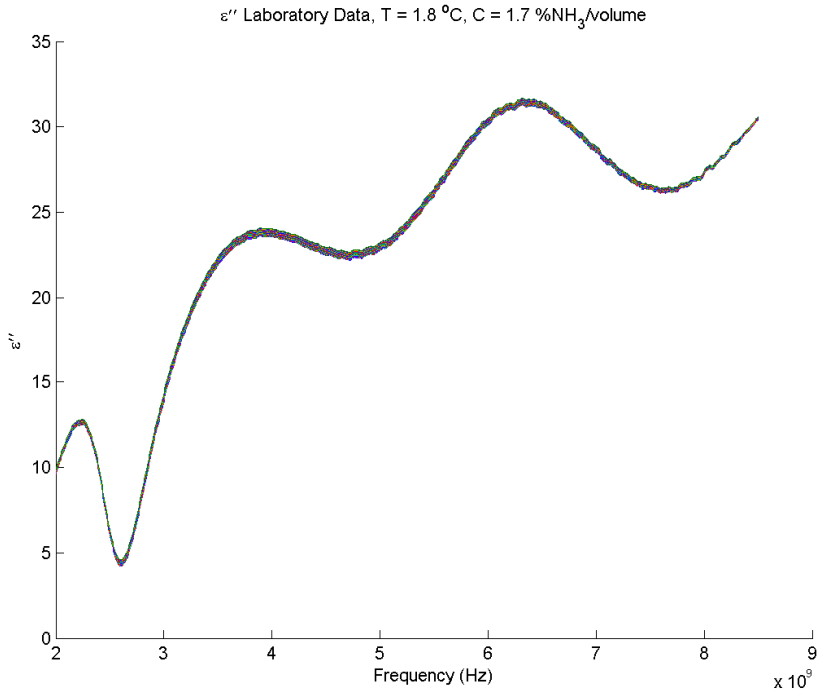

Figure 71. ε' laboratory data set 14 taken on 1/7/2011 - 03:02.

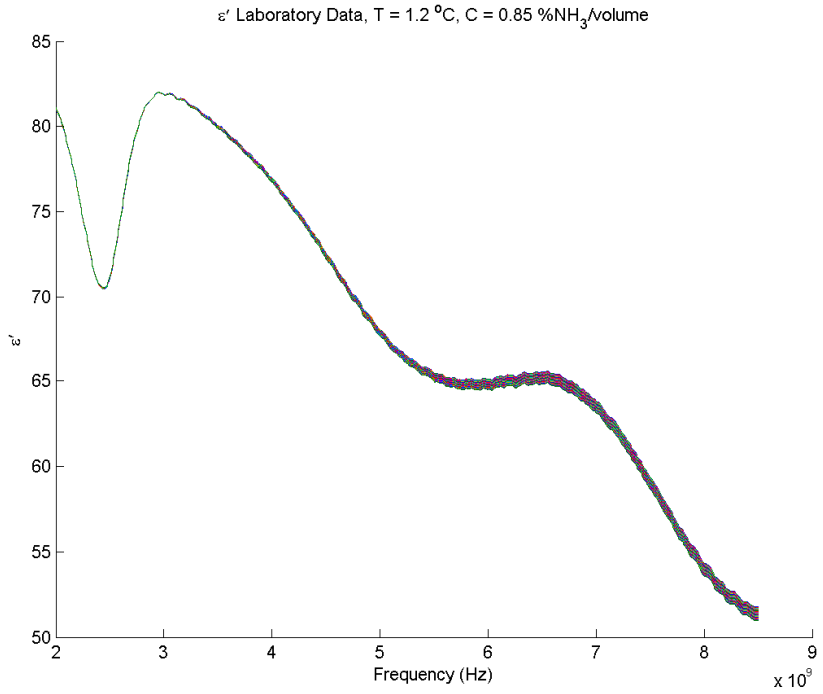

Figure 72. ε" laboratory data set 15 taken on 1/7/2011 - 03:48.

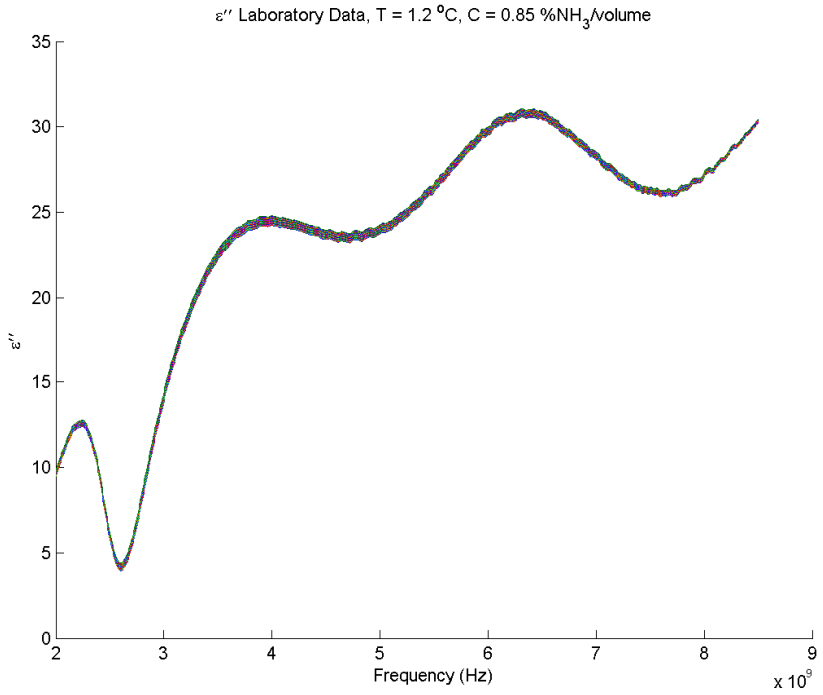

Figure 73. ε' laboratory data set 15 taken on 1/7/2011 - 03:48.

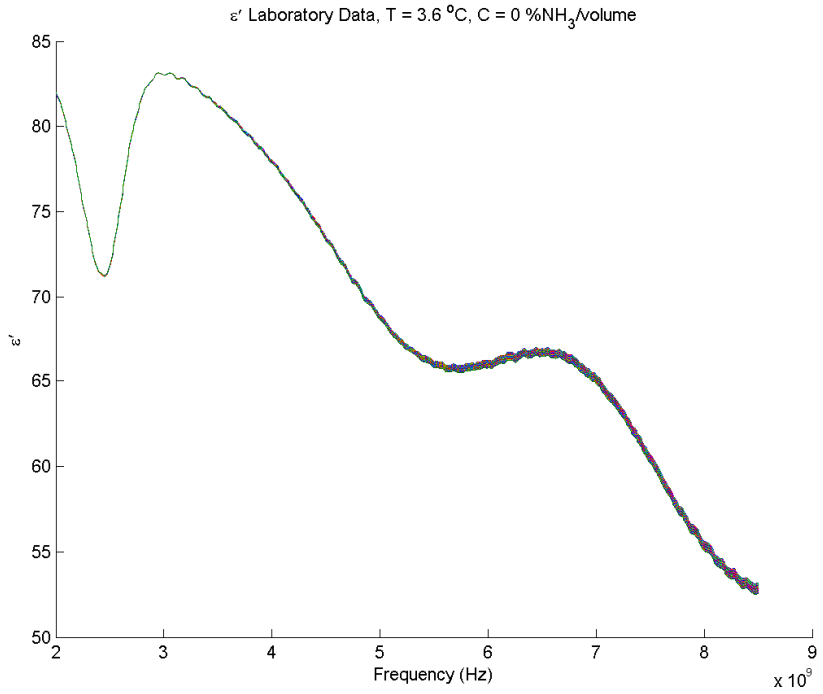

Figure 74. ε" laboratory data set 16 taken on 1/7/2011 - 04:47.

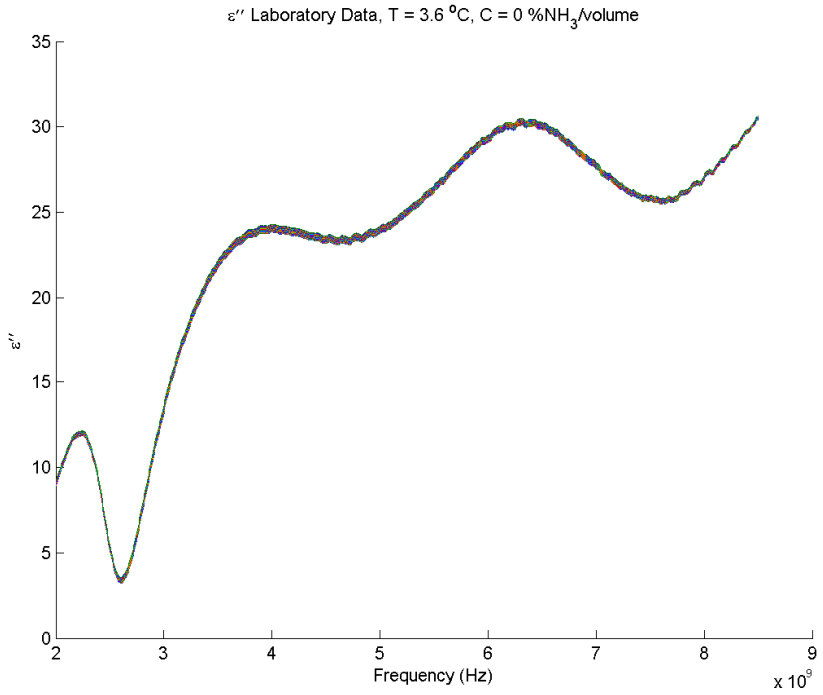

Figure 75. ε' laboratory data set 16 taken on 1/7/2011 - 04:47.

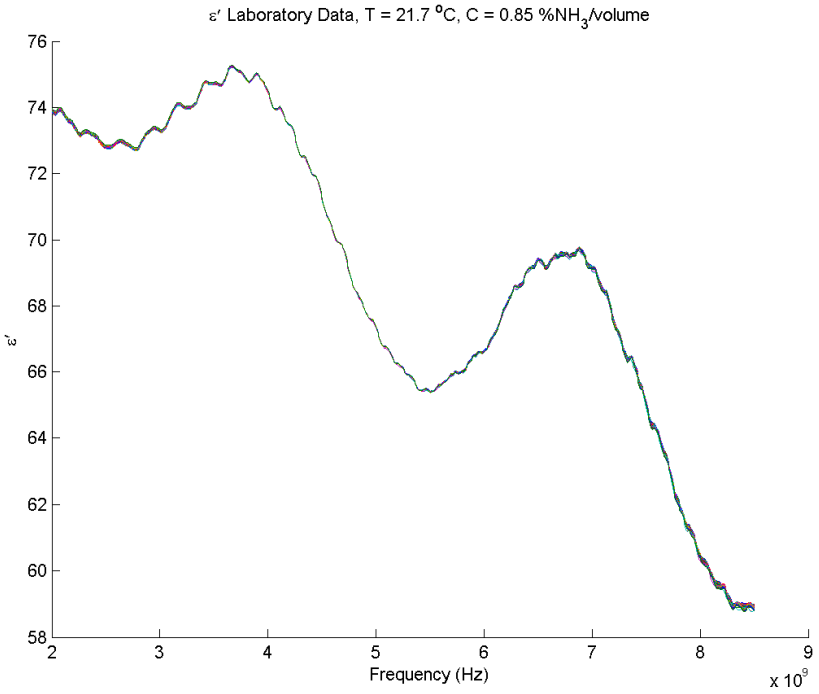

Figure 76. ε" laboratory data set 17 taken on 1/7/2011 - 05:12.

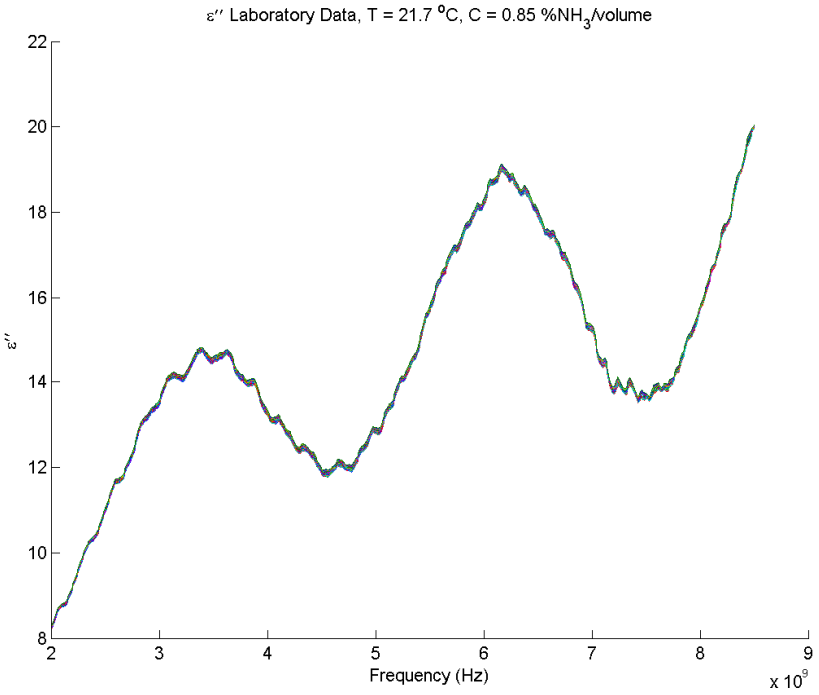

Figure 77. ε' laboratory data set 17 taken on 1/7/2011 - 05:12.

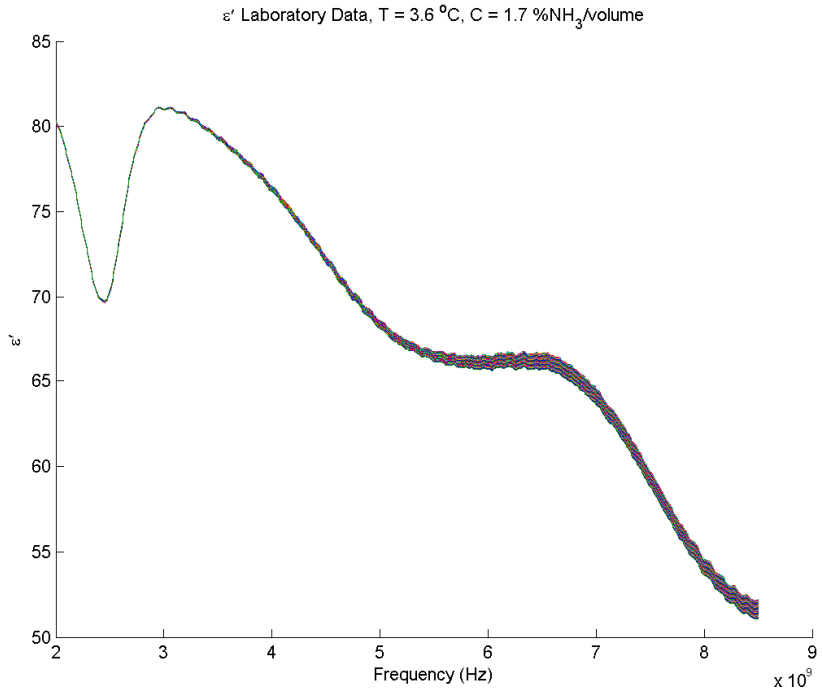

Figure 78. ε" laboratory data set 18 taken on 1/7/2011 - 05:41.

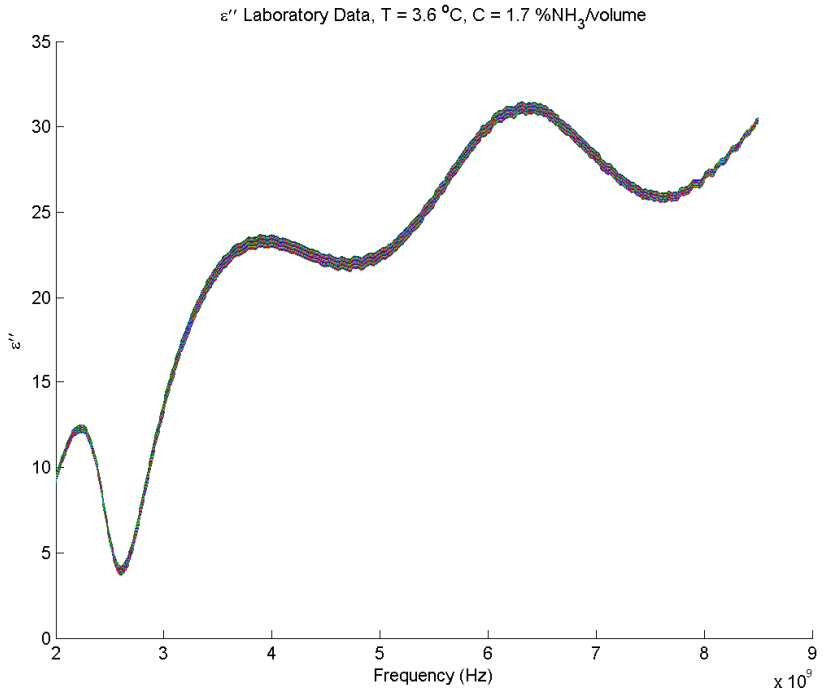

Figure 79. ε' laboratory data set 18 taken on 1/7/2011 - 05:41.

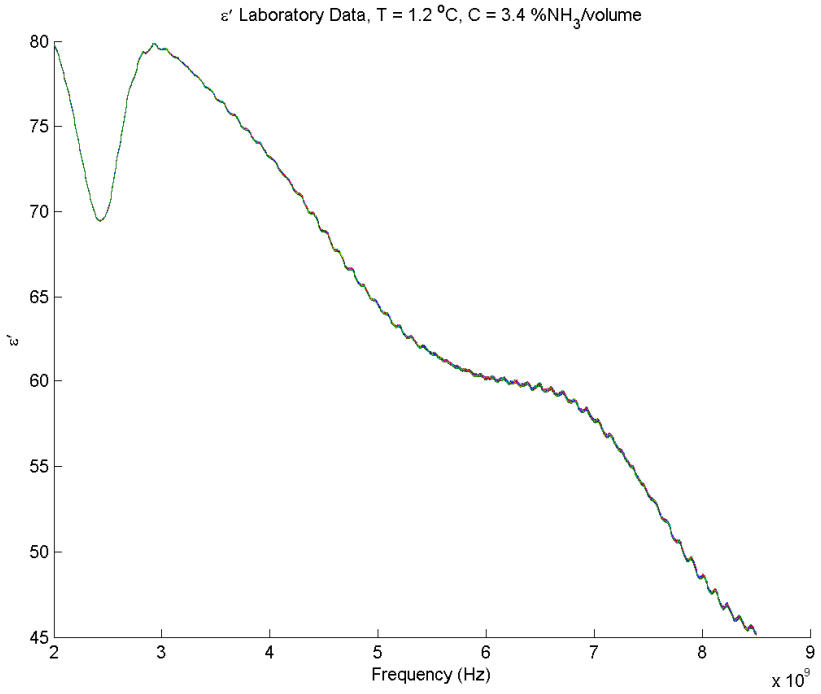

Figure 80. ε" laboratory data set 19 taken on 1/7/2011 - 13:05.

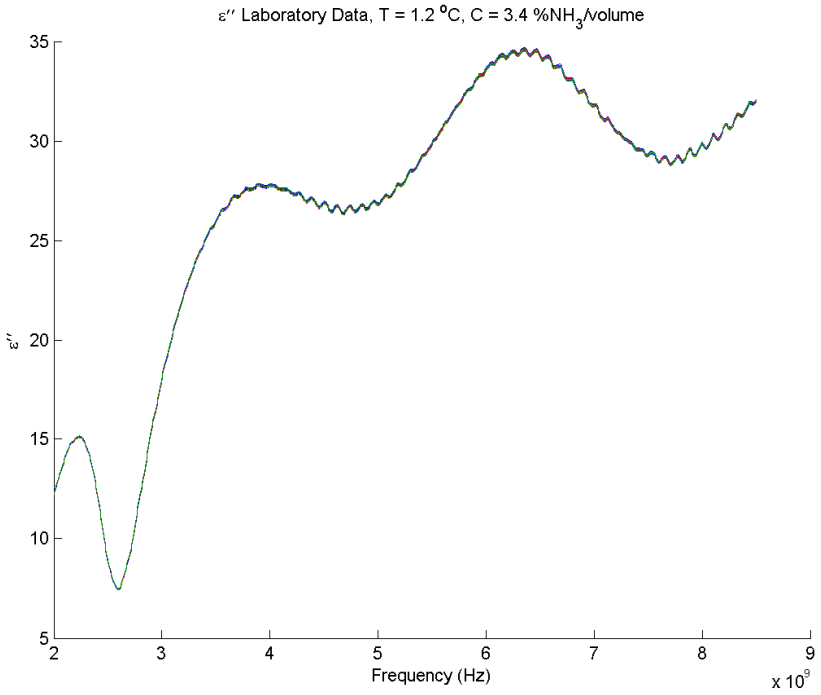

Figure 81. ε' laboratory data set 19 taken on 1/7/2011 - 13:05.

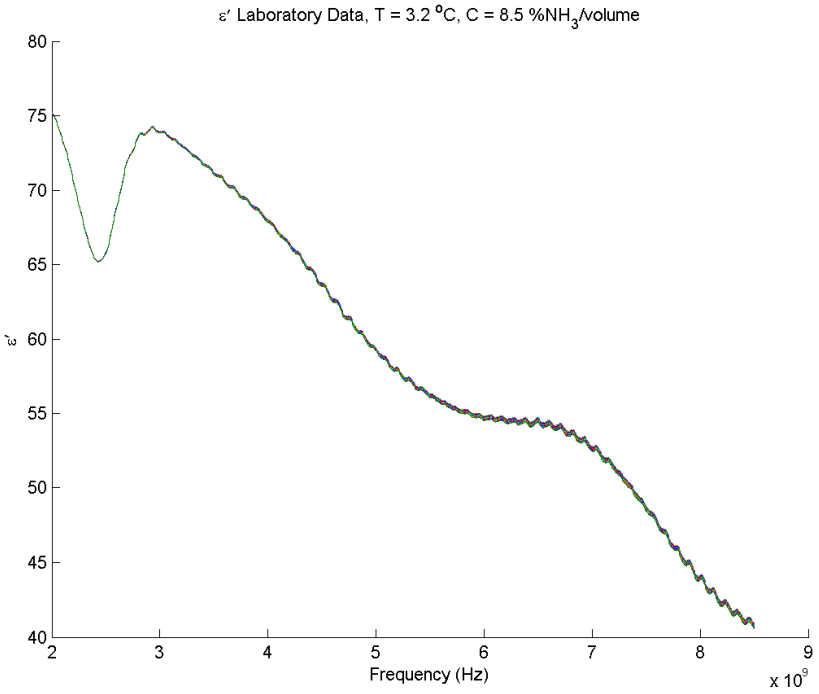

Figure 82. ε" laboratory data set 20 taken on 1/7/2011 - 13:32.

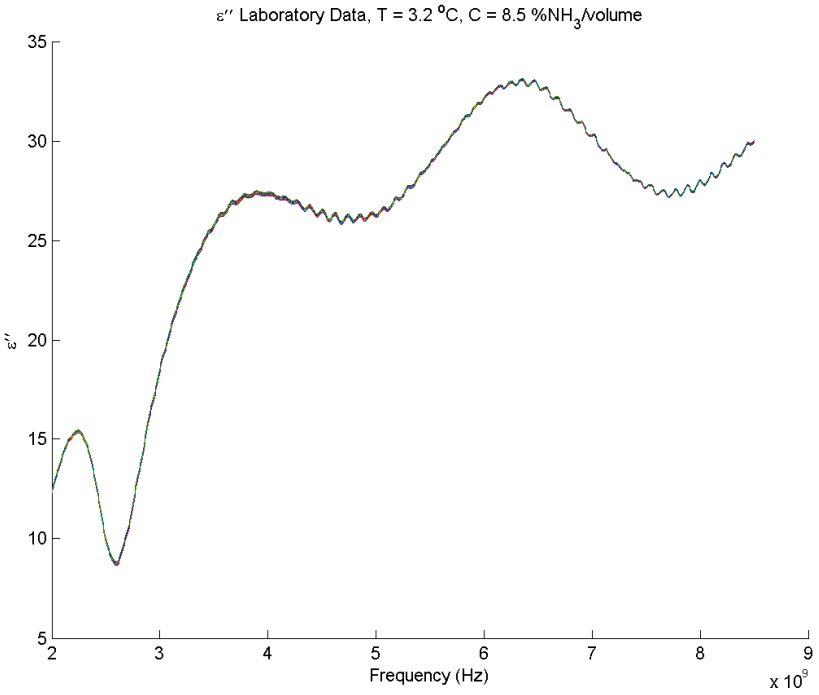

Figure 83. ε' laboratory data set 20 taken on 1/7/2011 - 13:32.

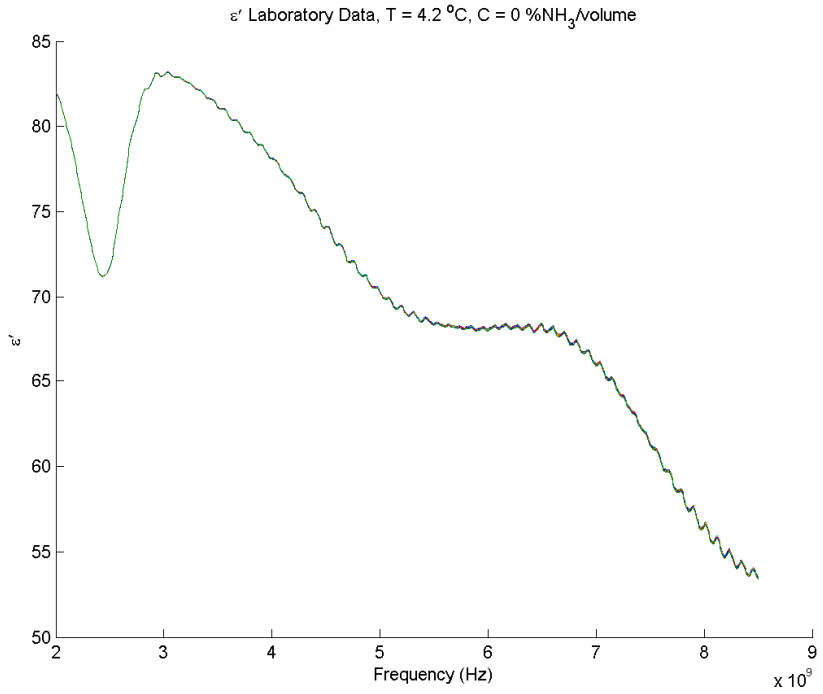

Figure 84. ε" laboratory data set 21 taken on 1/7/2011 - 14:39.

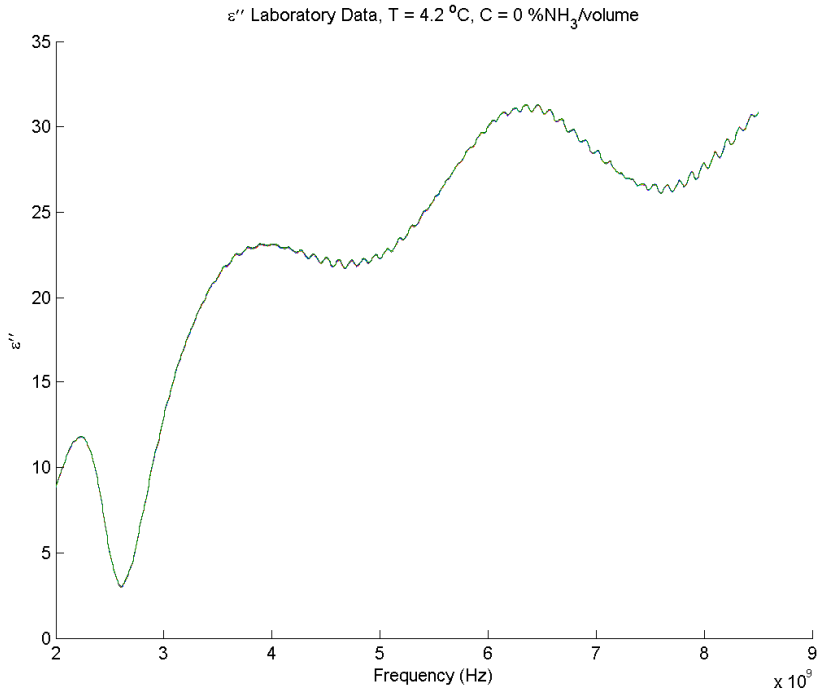

Figure 85. ε' laboratory data set 21 taken on 1/7/2011 - 14:39.

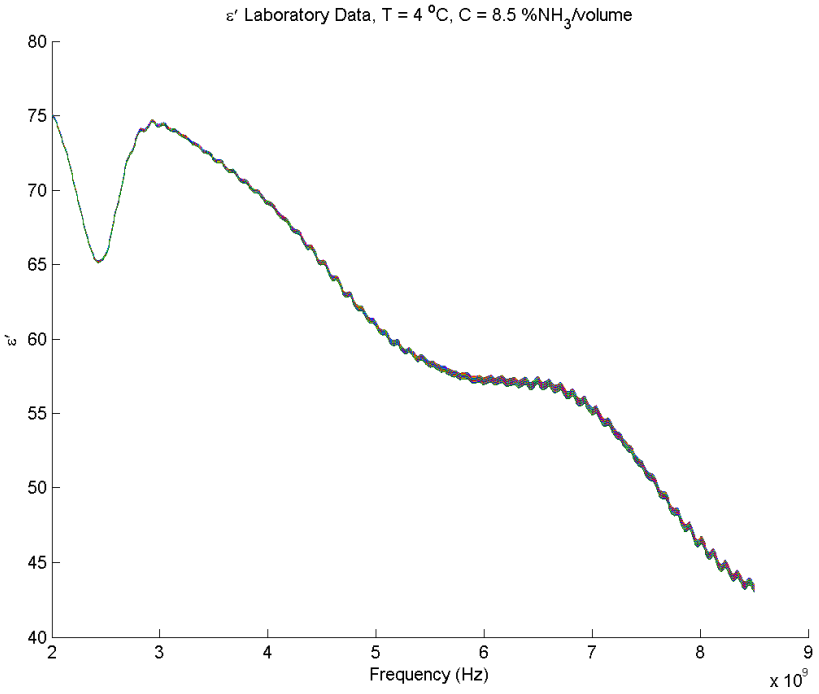

Figure 86. ε" laboratory data set 22 taken on 1/7/2011 - 15:11.

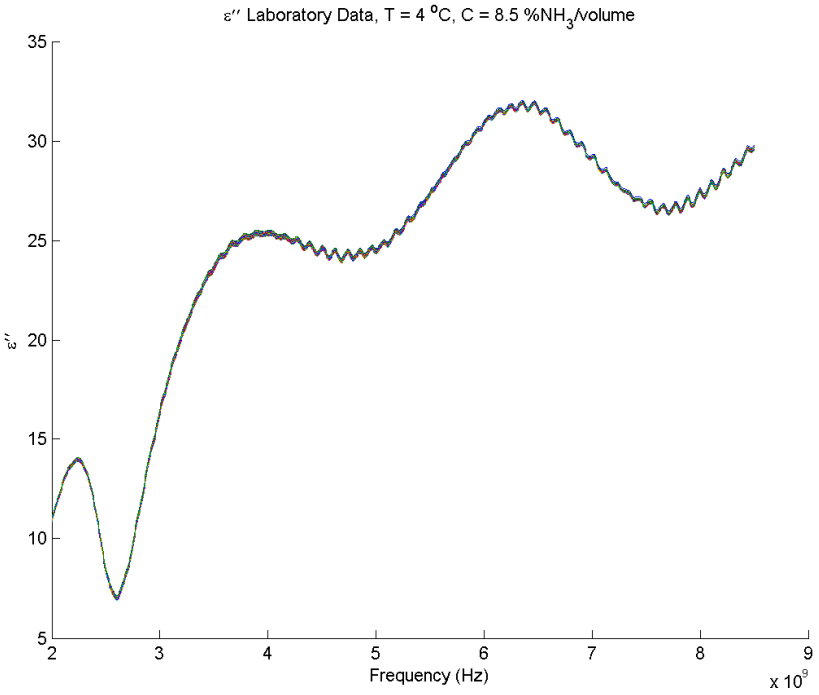

Figure 87. ε' laboratory data set 22 taken on 1/7/2011 - 15:11.

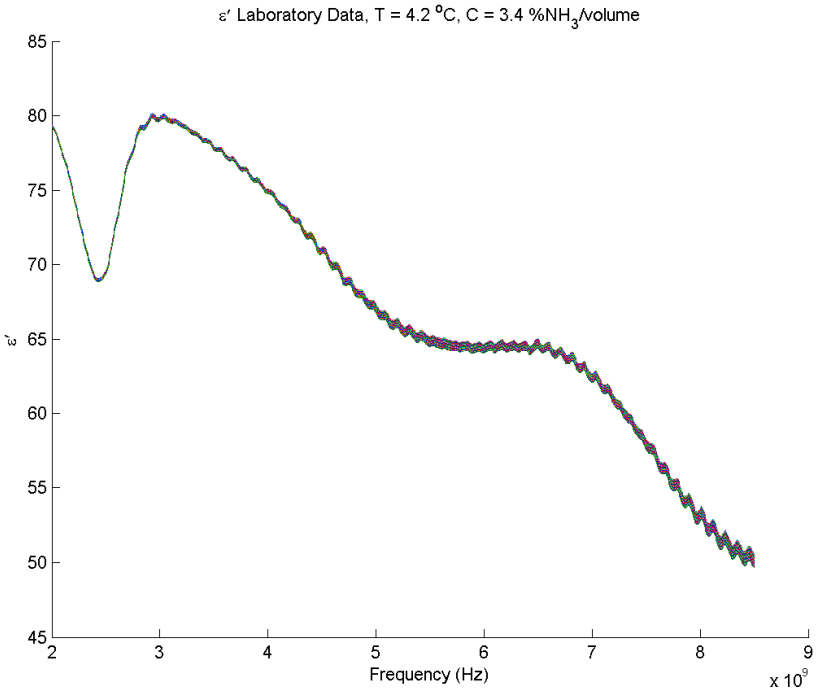

Figure 88. ε" laboratory data set 23 taken on 1/7/2011 - 15:38.

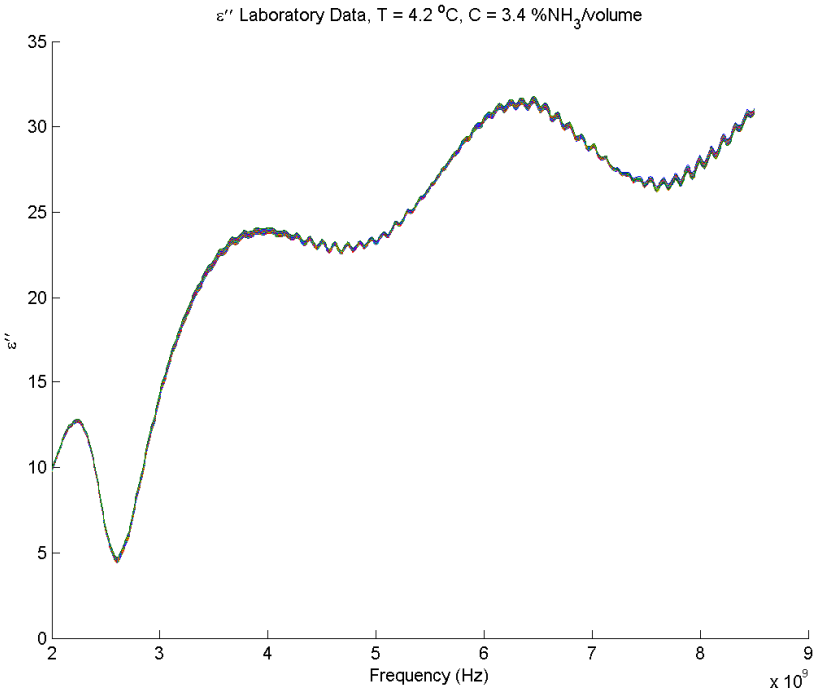

Figure 89. ε' laboratory data set 23 taken on 1/7/2011 - 15:38.

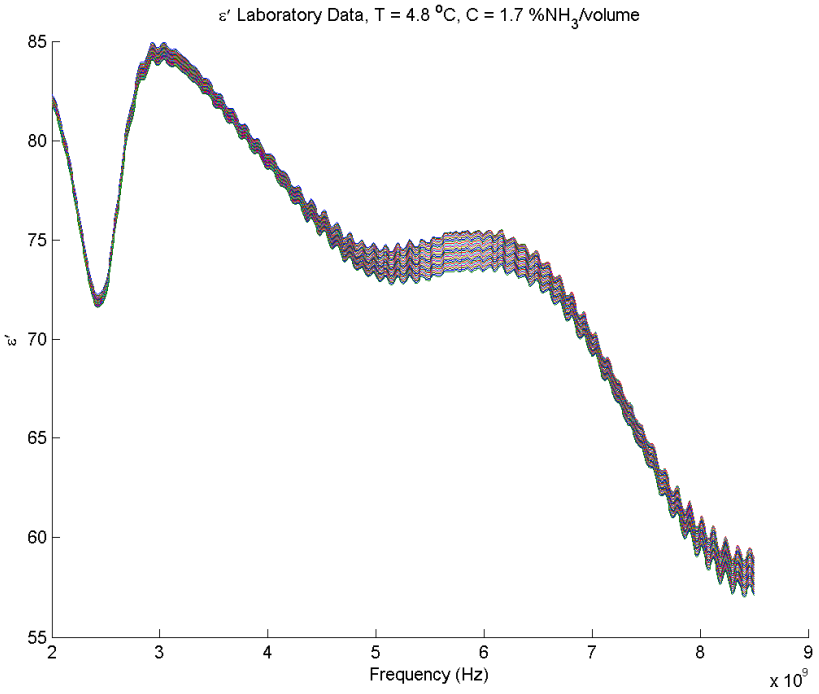

Figure 90. ε" laboratory data set 24 taken on 1/7/2011 - 16:10.

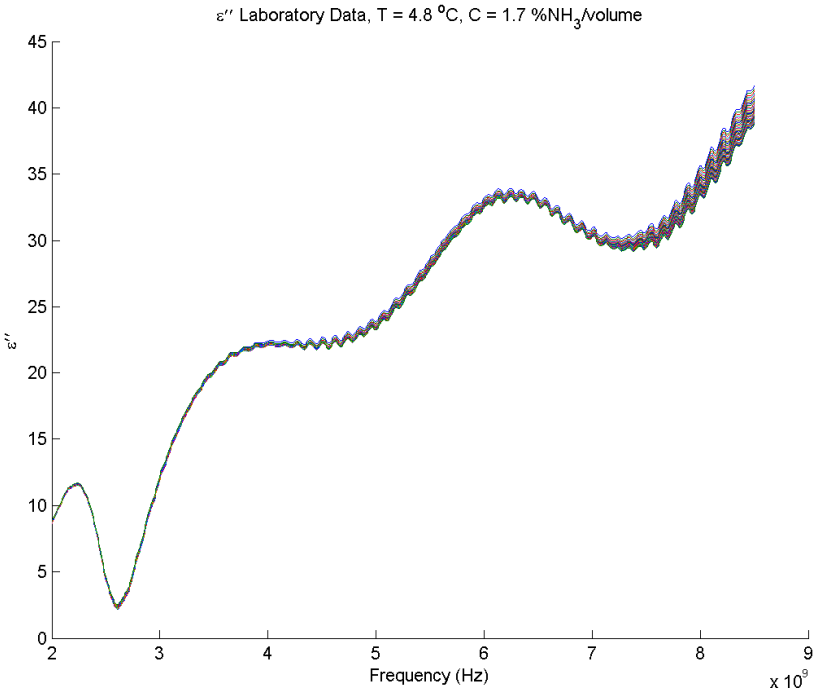

Figure 91. ε' laboratory data set 24 taken on 1/7/2011 - 16:10.

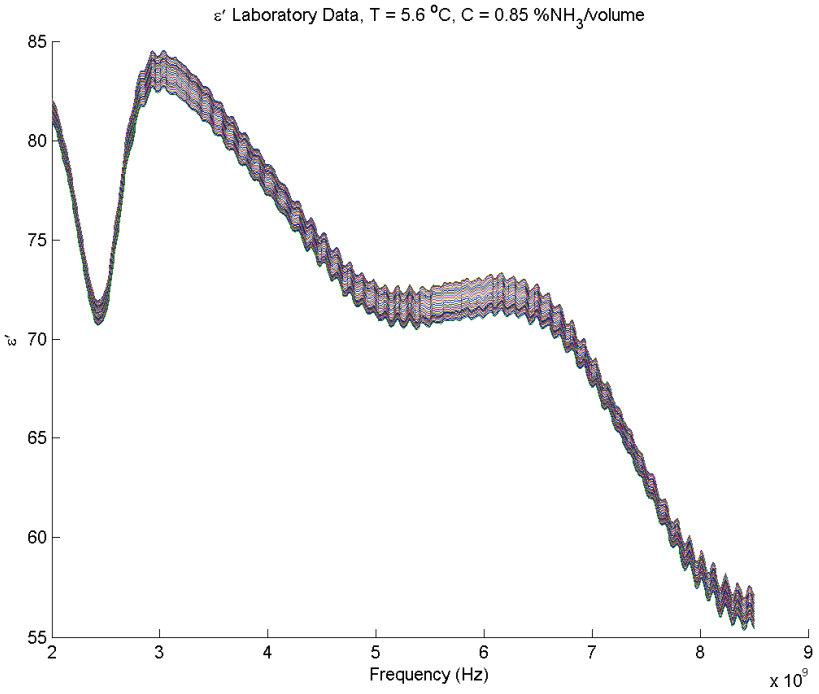

Figure 92. ε" laboratory data set 25 taken on 1/7/2011 - 16:35.

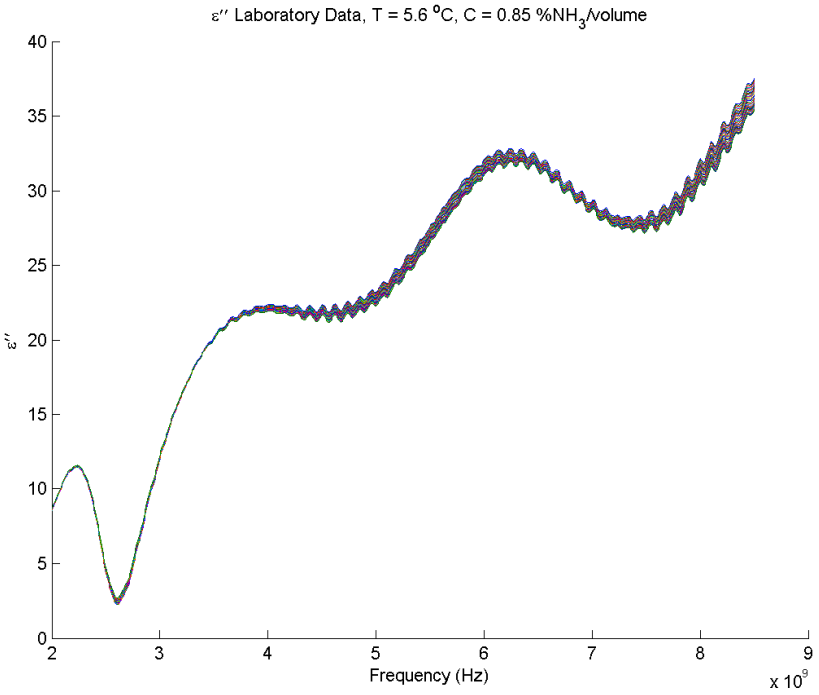

Figure 93. ε' laboratory data set 25 taken on 1/7/2011 - 16:35.

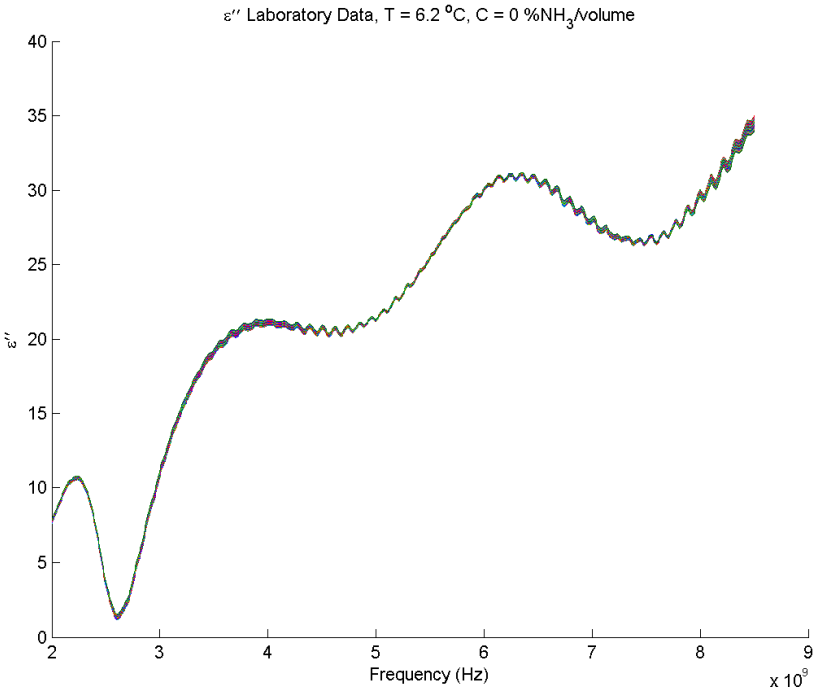

Figure 94. ε" laboratory data set 26 taken on 1/7/2011 - 17:00.

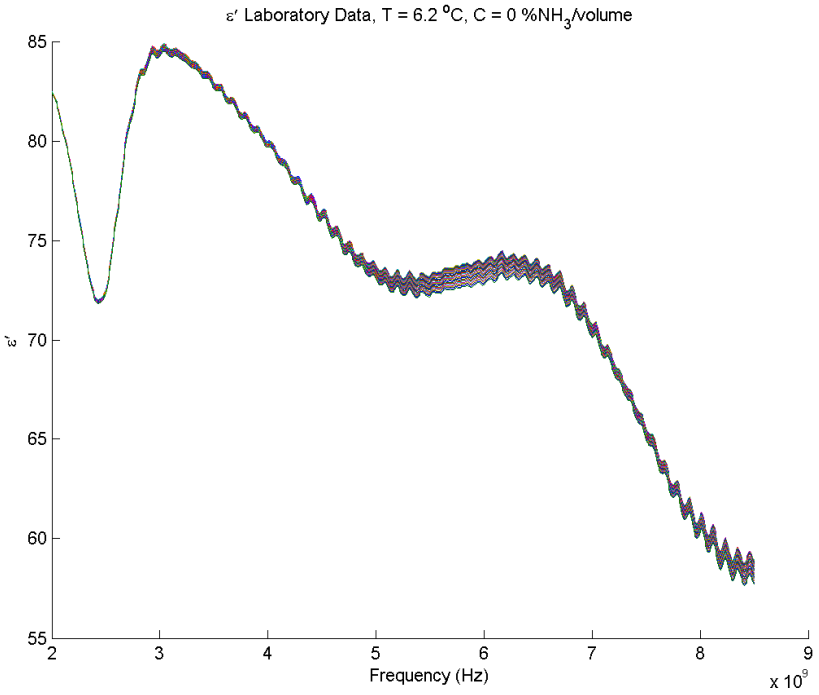

Figure 95. ε' laboratory data set 26 taken on 1/7/2011 - 17:00.

Appendix B

Complete Model Performance

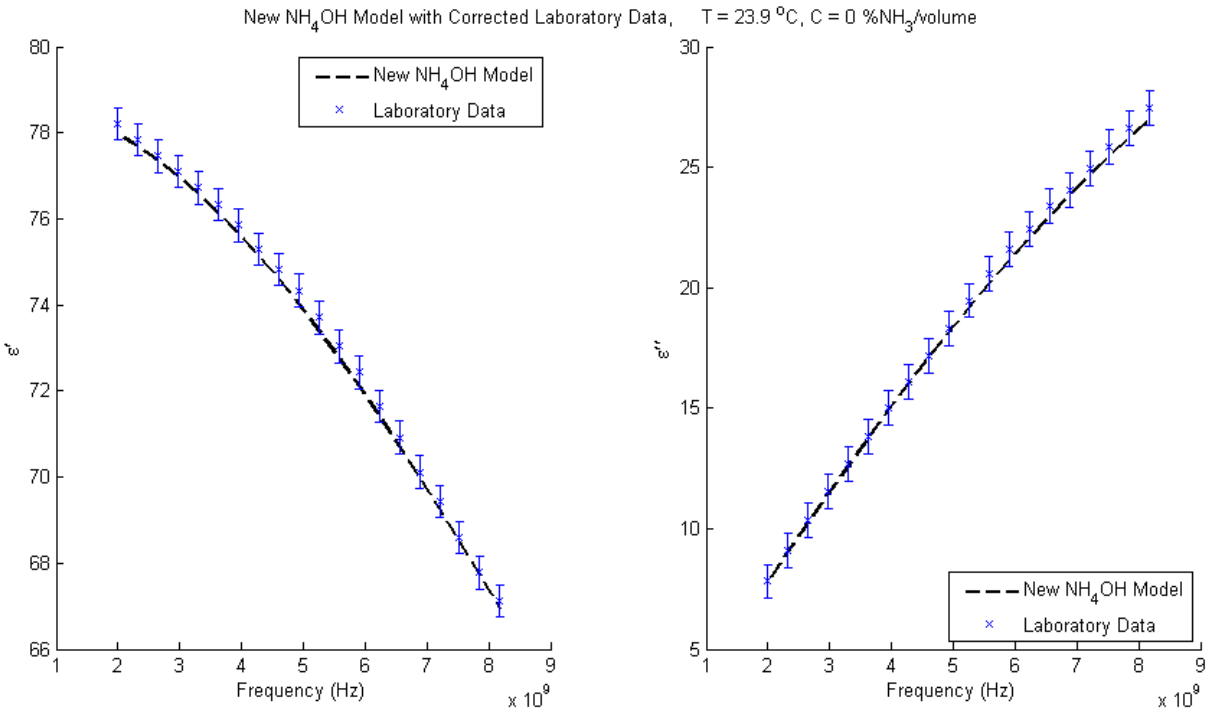

Figure 96. Laboratory data set 1 taken on 7/1/10 - 19:21 with new NH_4OH model.

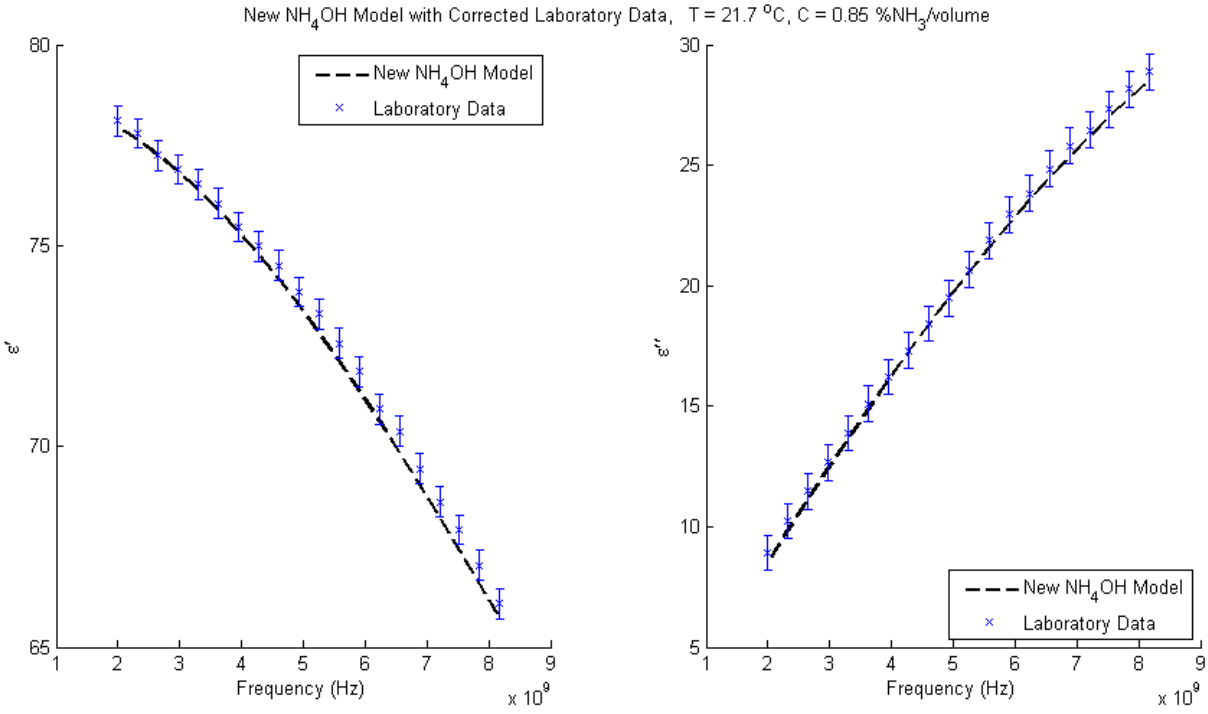

Figure 97. Laboratory data set 2 taken on 7/1/10 - 19:52 with new NH_4OH model.

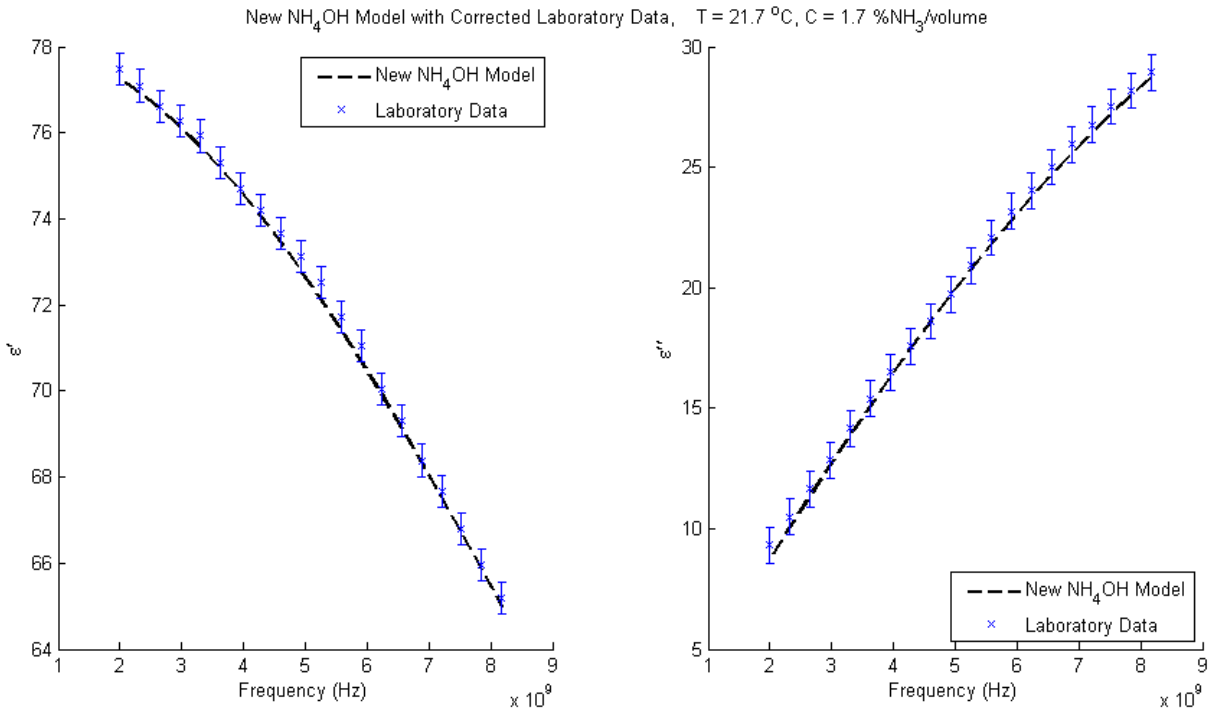

Figure 98. Laboratory data set 3 taken on 7/1/10 - 20:13 with new NH_4OH model.

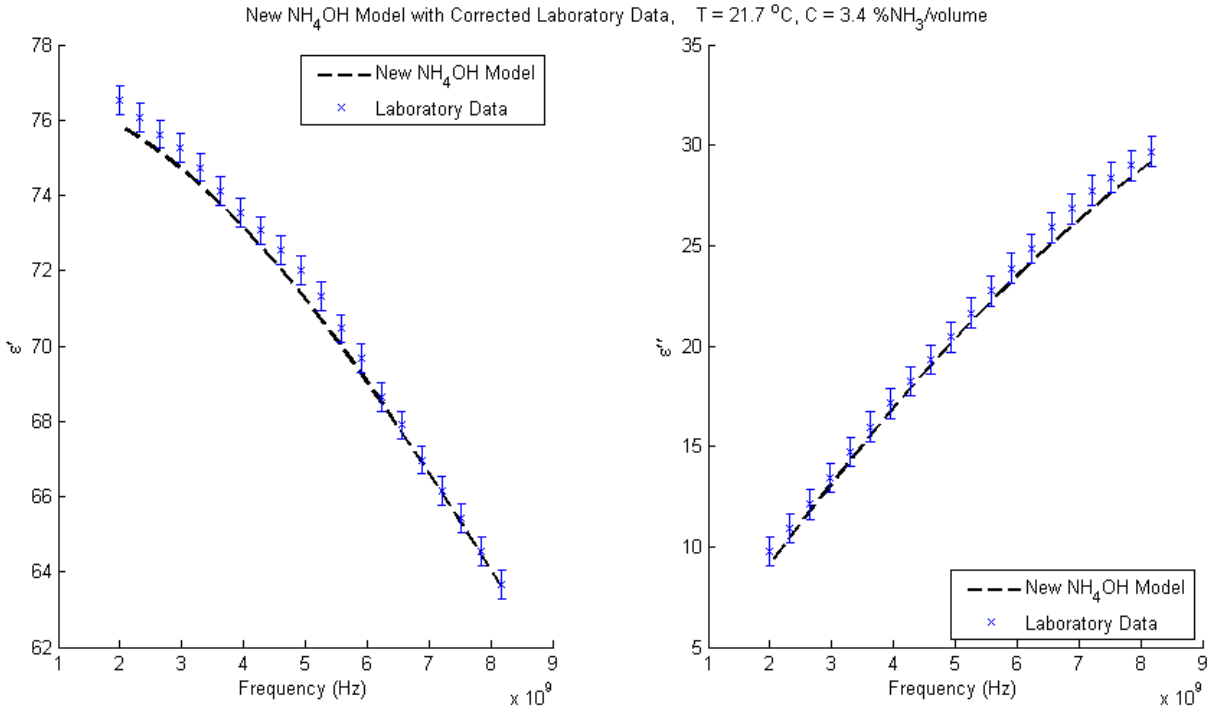

Figure 99. Laboratory data set 4 taken on 7/1/10 - 20:37 with new NH_4OH model.

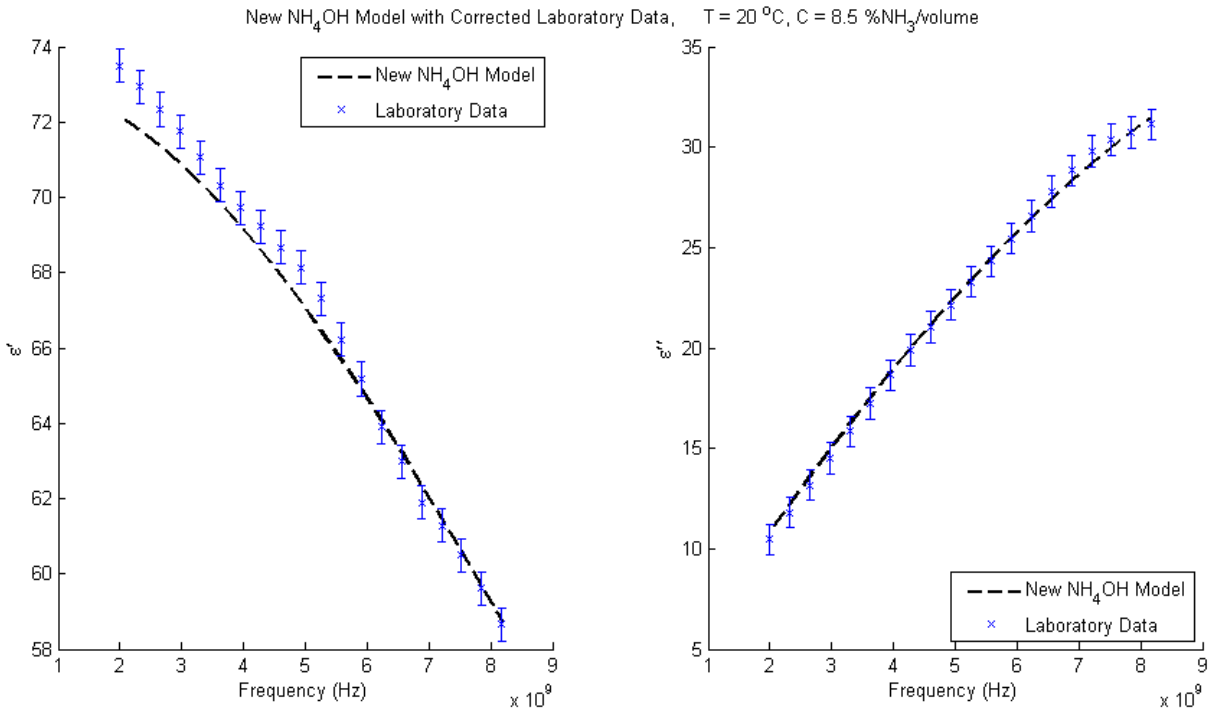

Figure 100. Laboratory data set 5 taken on 7/1/10 - 22:46 with new NH_4OH model.

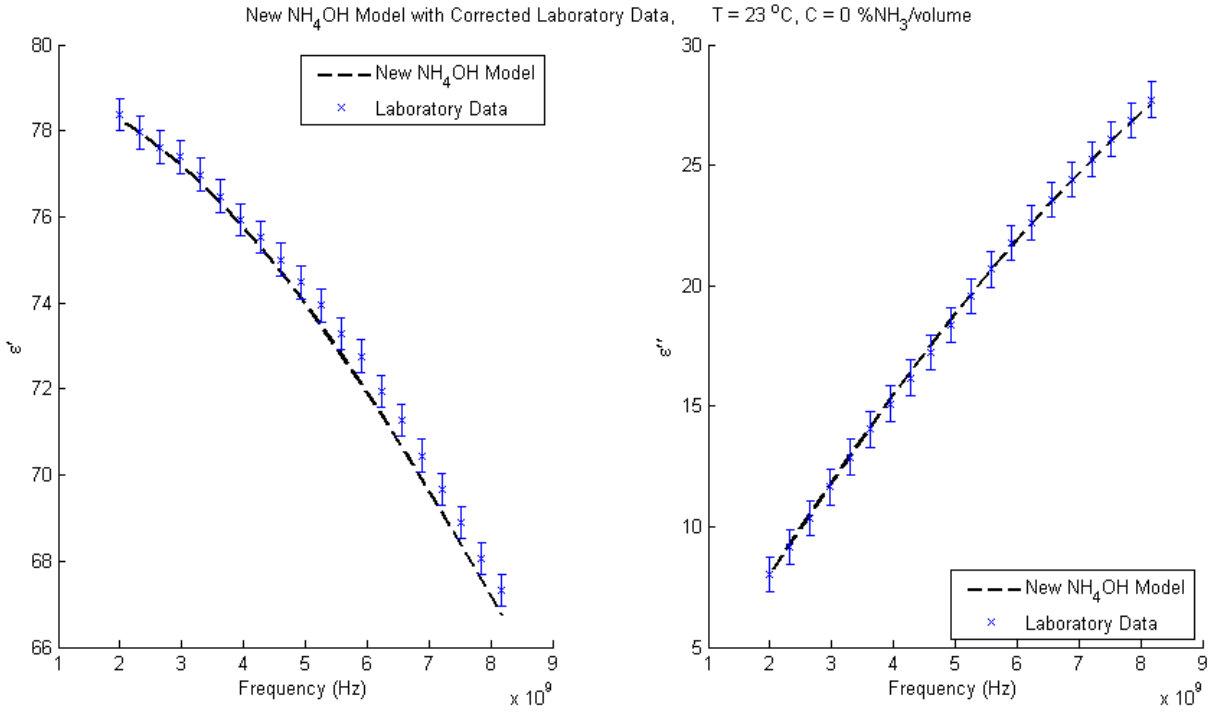

Figure 101. Laboratory data set 6 taken on 7/1/10 - 23:39 with new NH_4OH model.

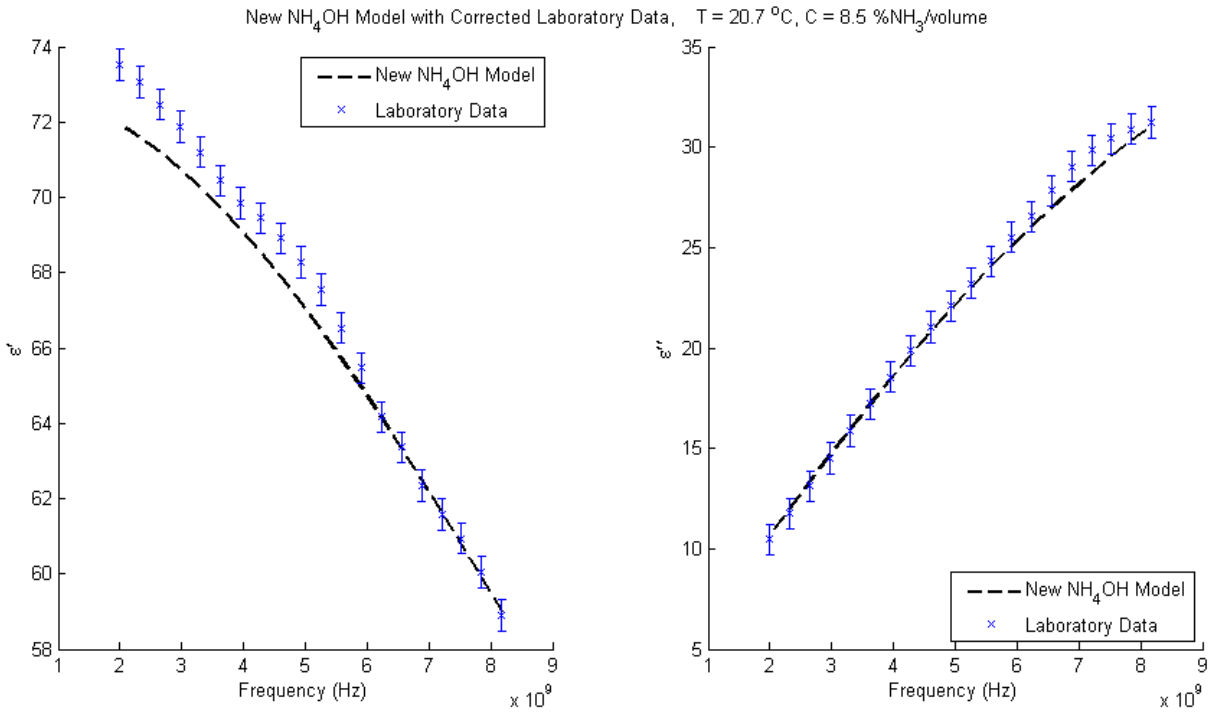

Figure 102. Laboratory data set 7 taken on 7/2/10 - 00:07 with new NH_4OH model.

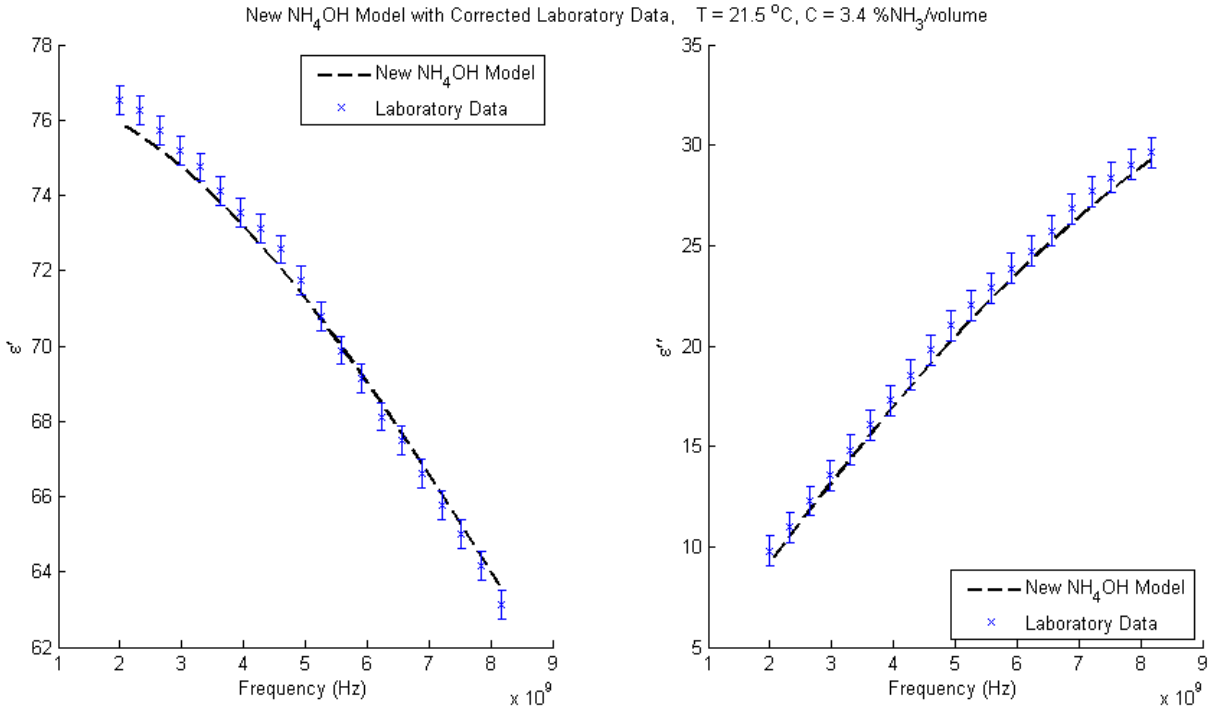

Figure 103. Laboratory data set 8 taken on 7/2/10 - 00:36 with new NH_4OH model.

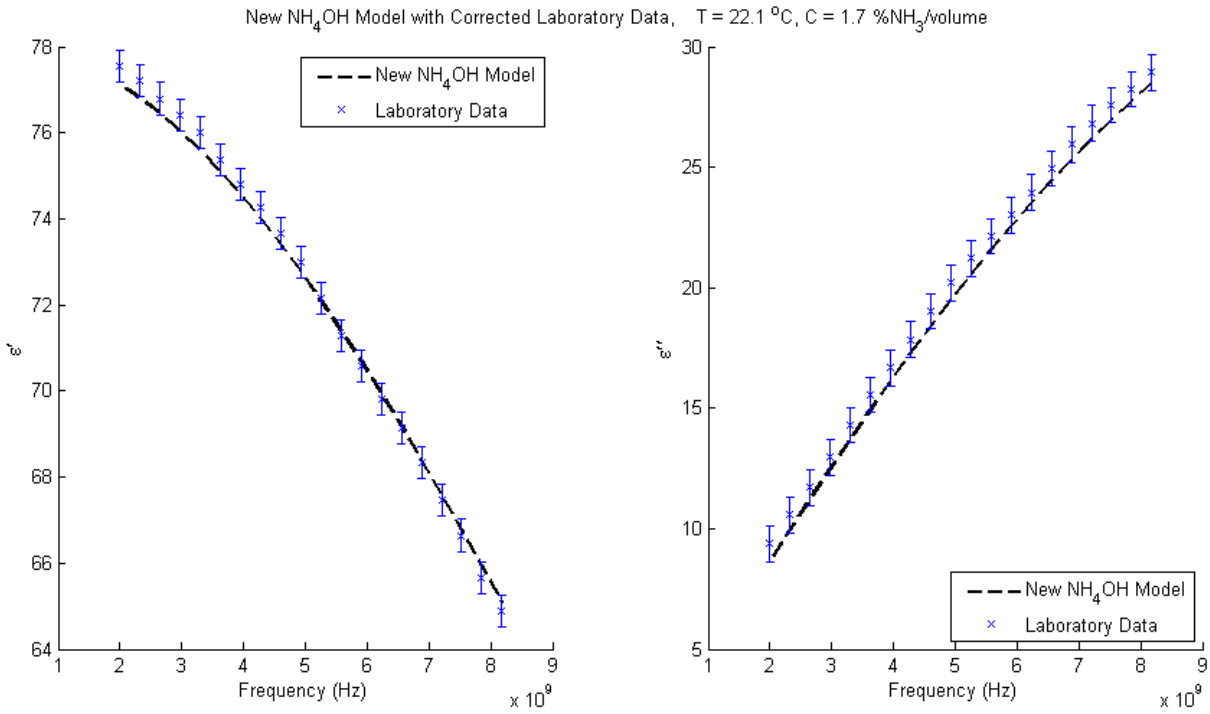

Figure 104. Laboratory data set 9 taken on 7/2/10 - 01:02 with new NH_4OH model.

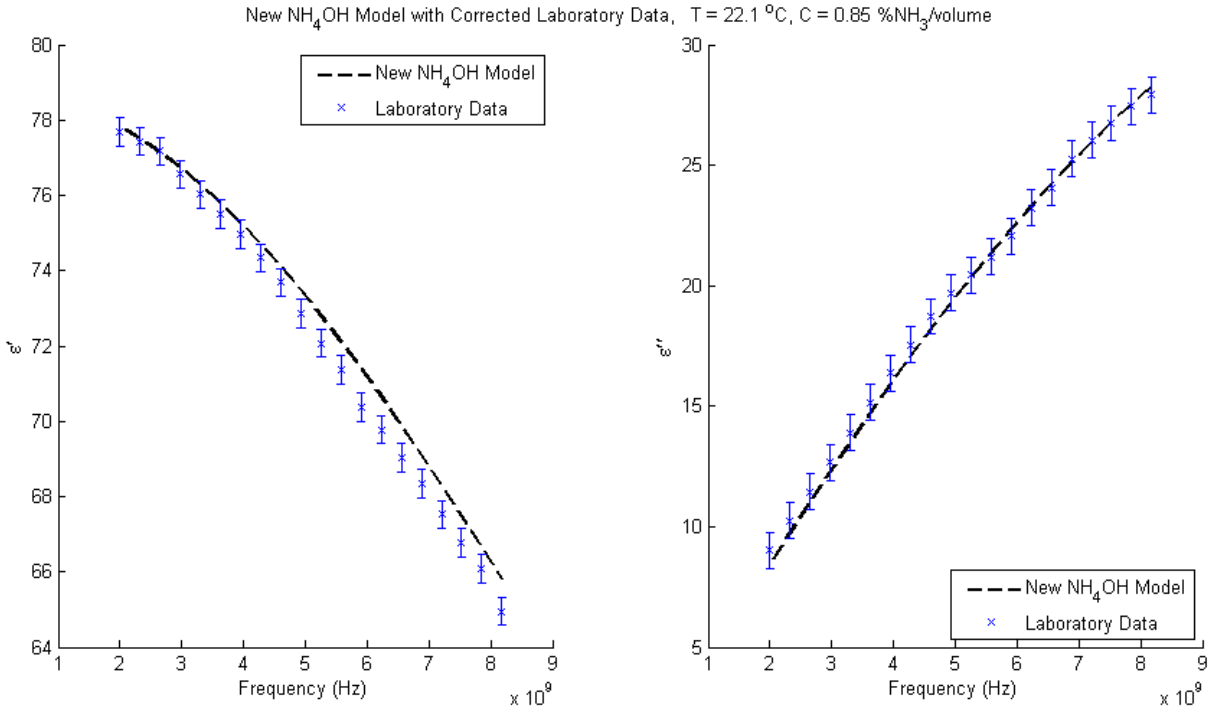

Figure 105. Laboratory data set 10 taken on 7/2/10 - 01:28 with new NH_4OH model.

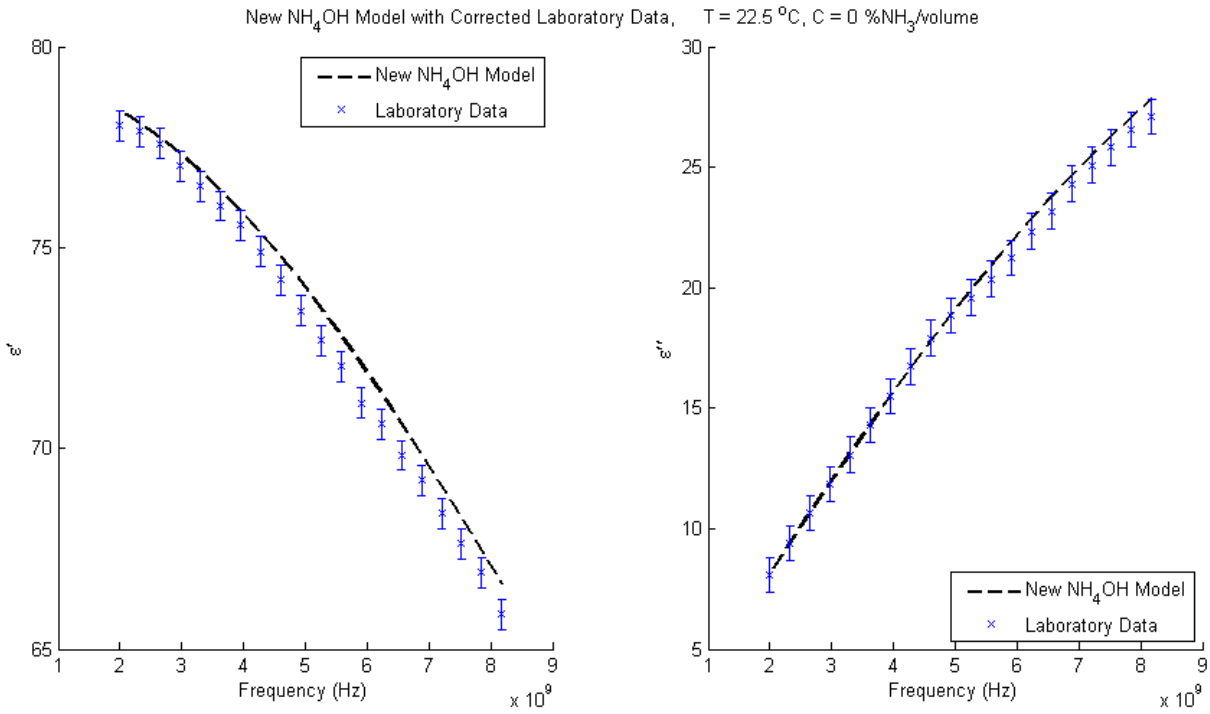

Figure 106. Laboratory data set 11 taken on 7/2/10 - 01:52 with new NH_4OH model.

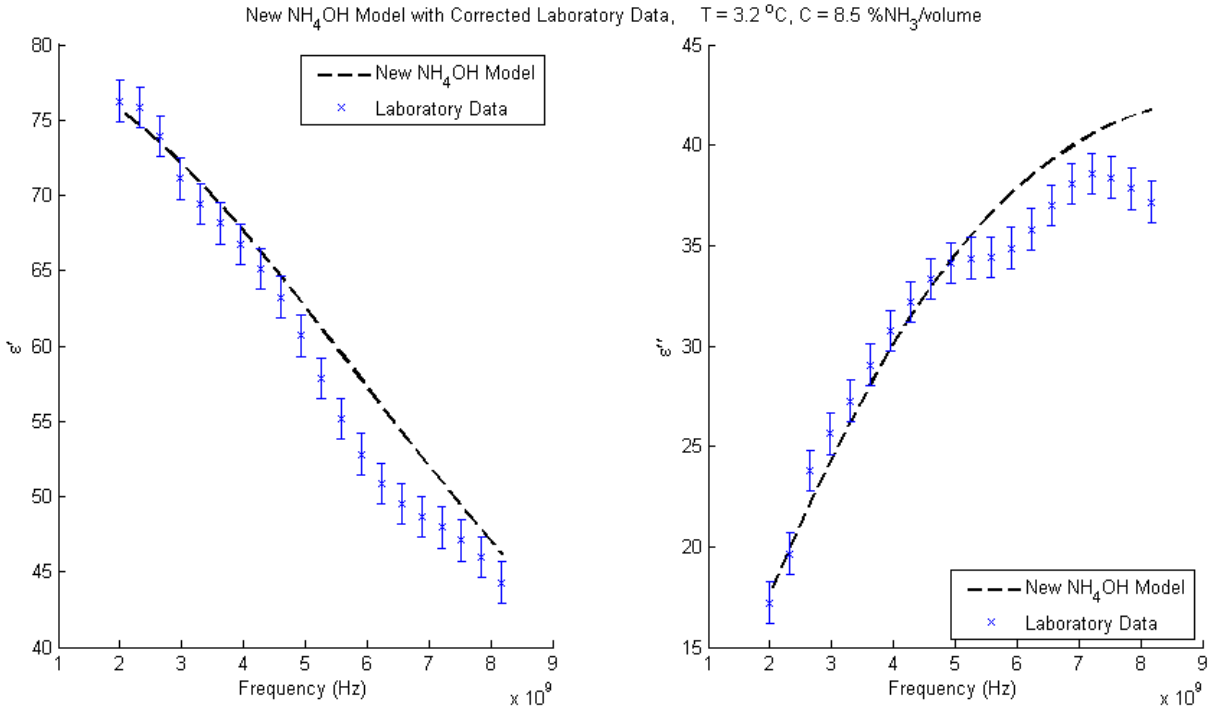

Figure 107. Laboratory data set 12 taken on 1/7/11 - 01:21 with new NH_4OH model.

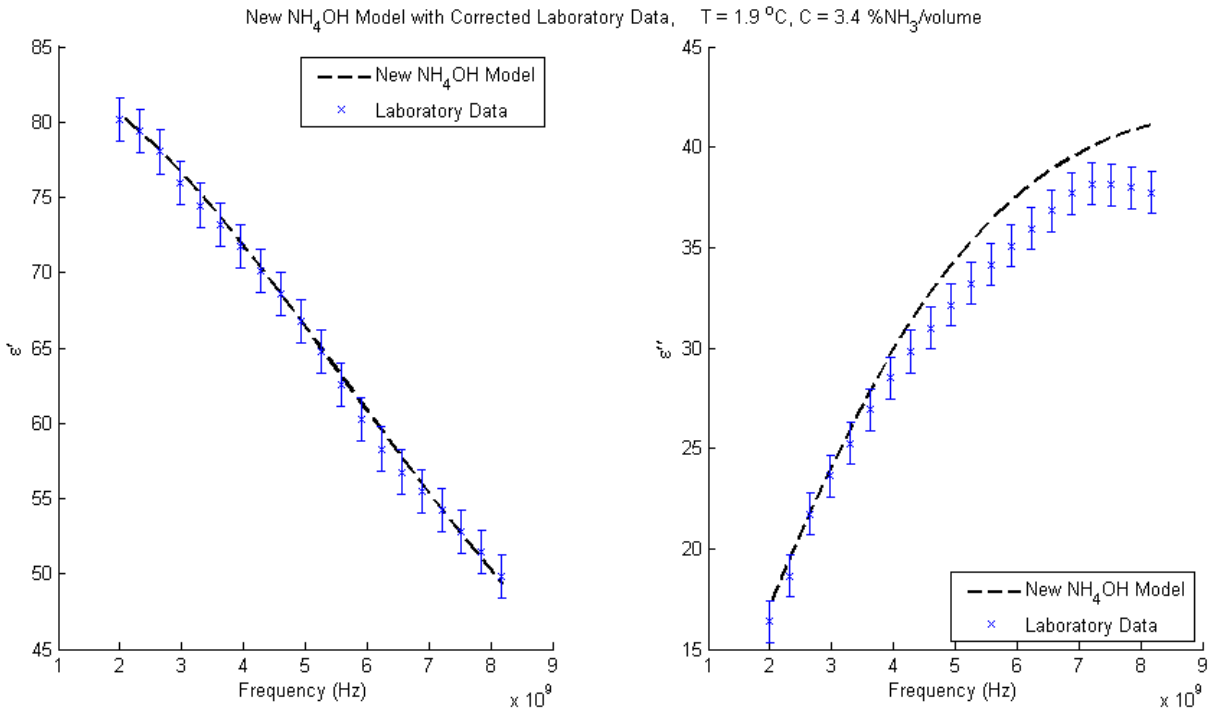

Figure 108. Laboratory data set 13 taken on 1/7/11 - 02:10 with new NH_4OH model.

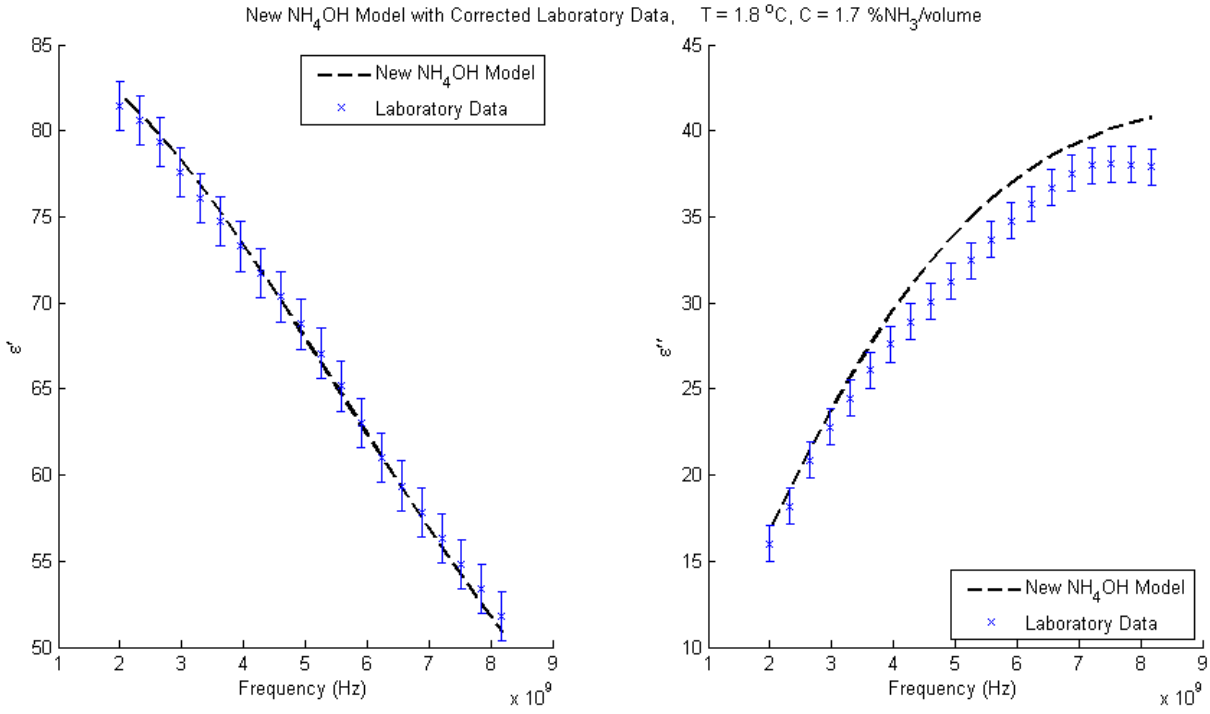

Figure 109. Laboratory data set 14 taken on 1/7/11 - 03:02 with new NH_4OH model.

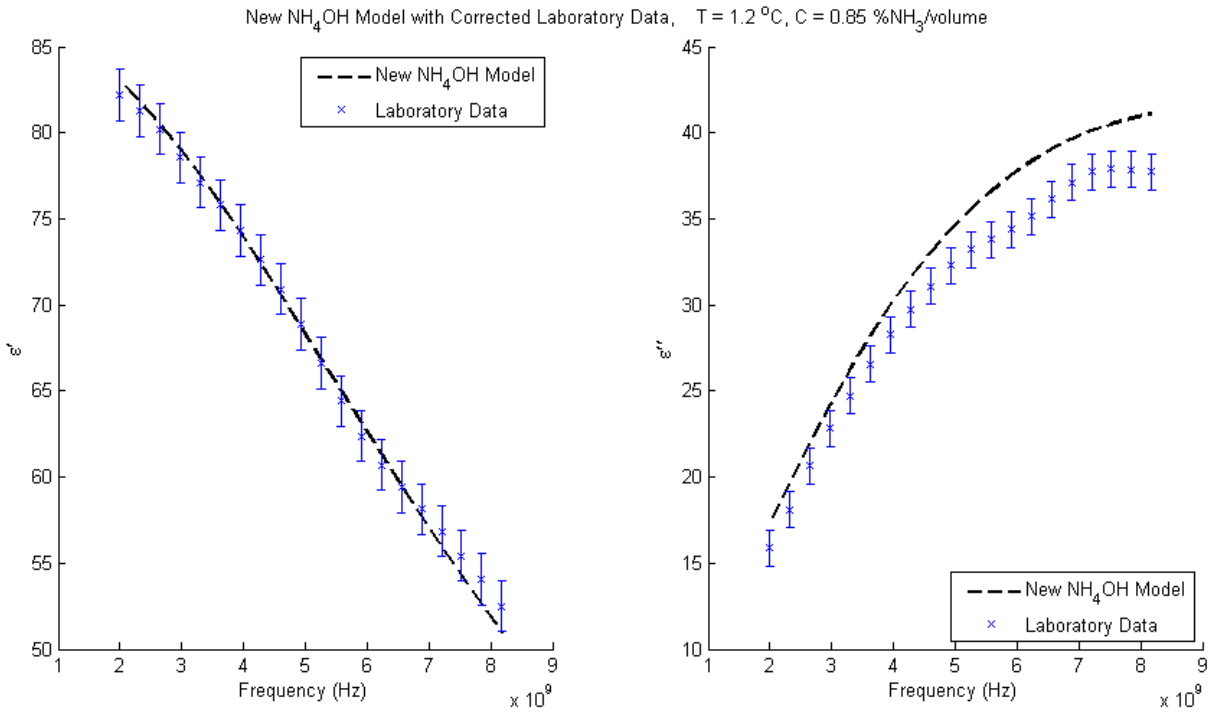

Figure 110. Laboratory data set 15 taken on 1/7/11 - 03:48 with new NH_4OH model.

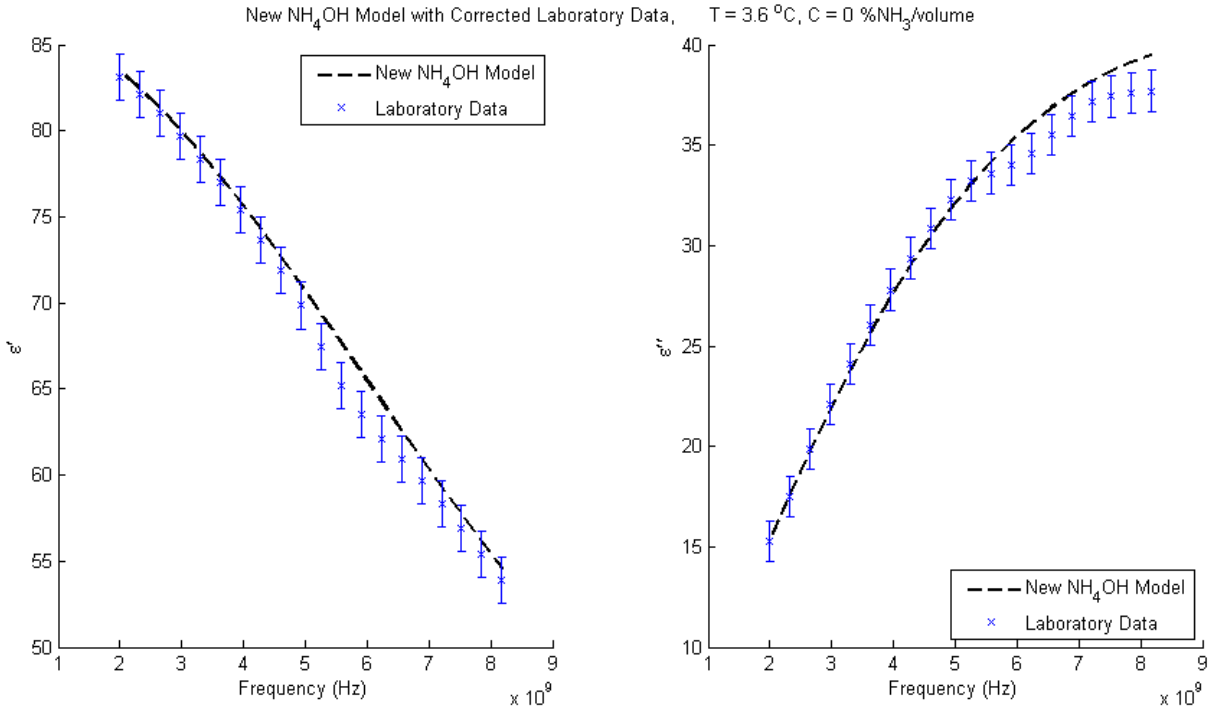

Figure 111. Laboratory data set 16 taken on 1/7/11 - 04:47 with new NH_4OH model.

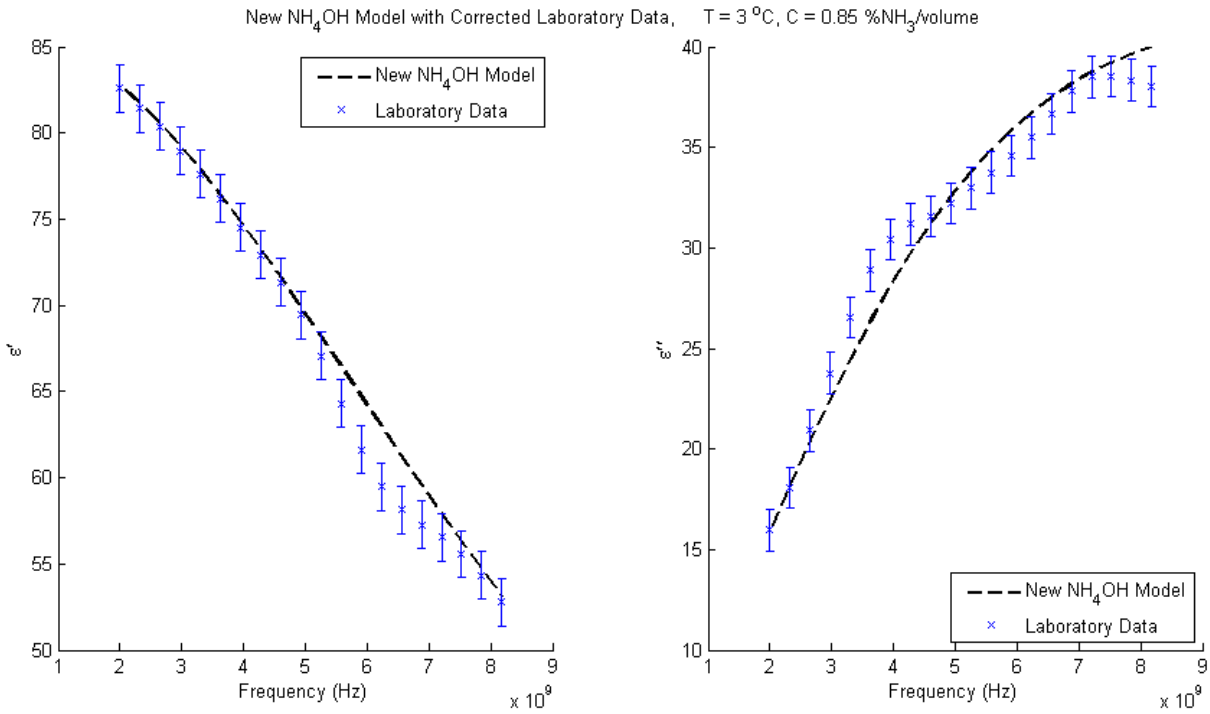

Figure 112. Laboratory data set 17 taken on 1/7/11 - 05:12 with new NH_4OH model.

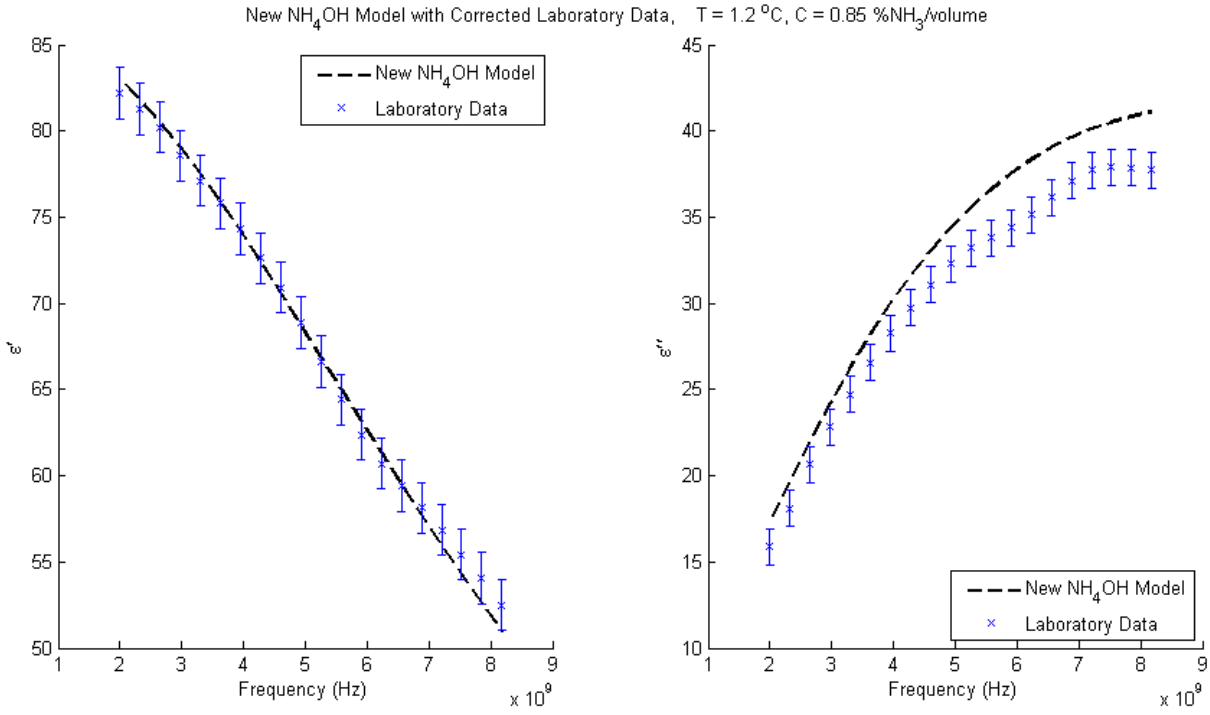

Figure 113. Laboratory data set 18 taken on 1/7/11 - 05:41 with new NH_4OH model.

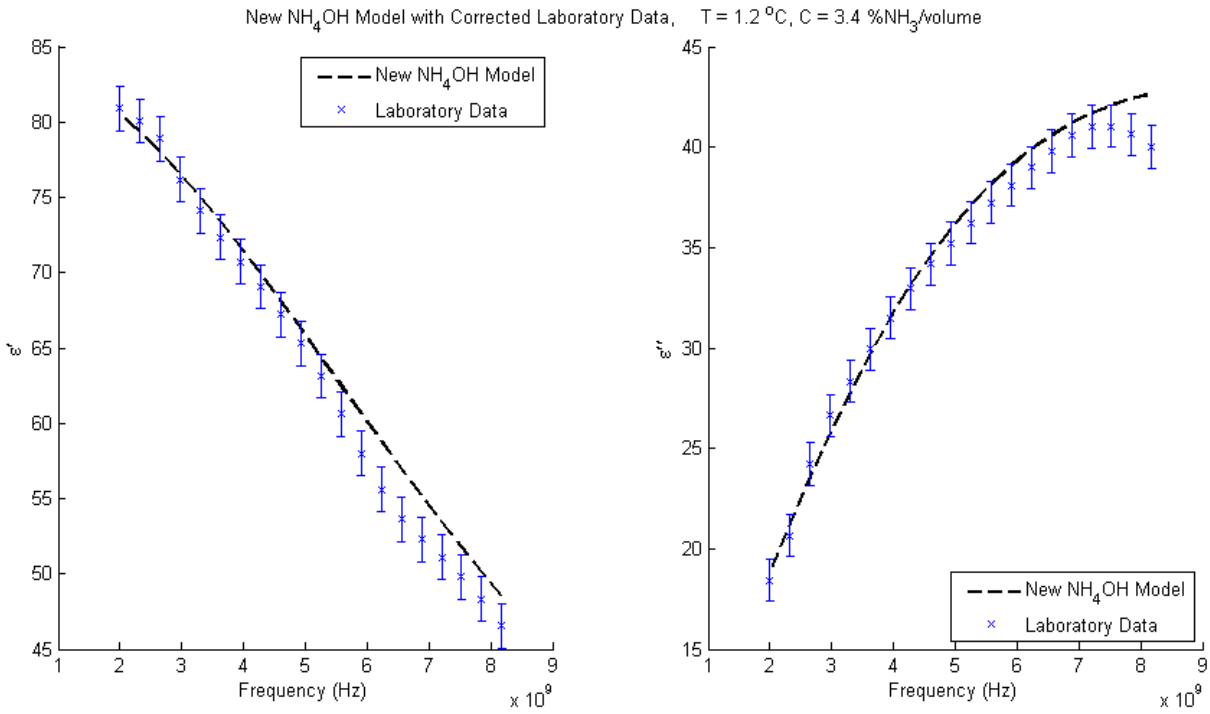

Figure 114. Laboratory data set 19 taken on 1/7/11 - 13:05 with new NH_4OH model.

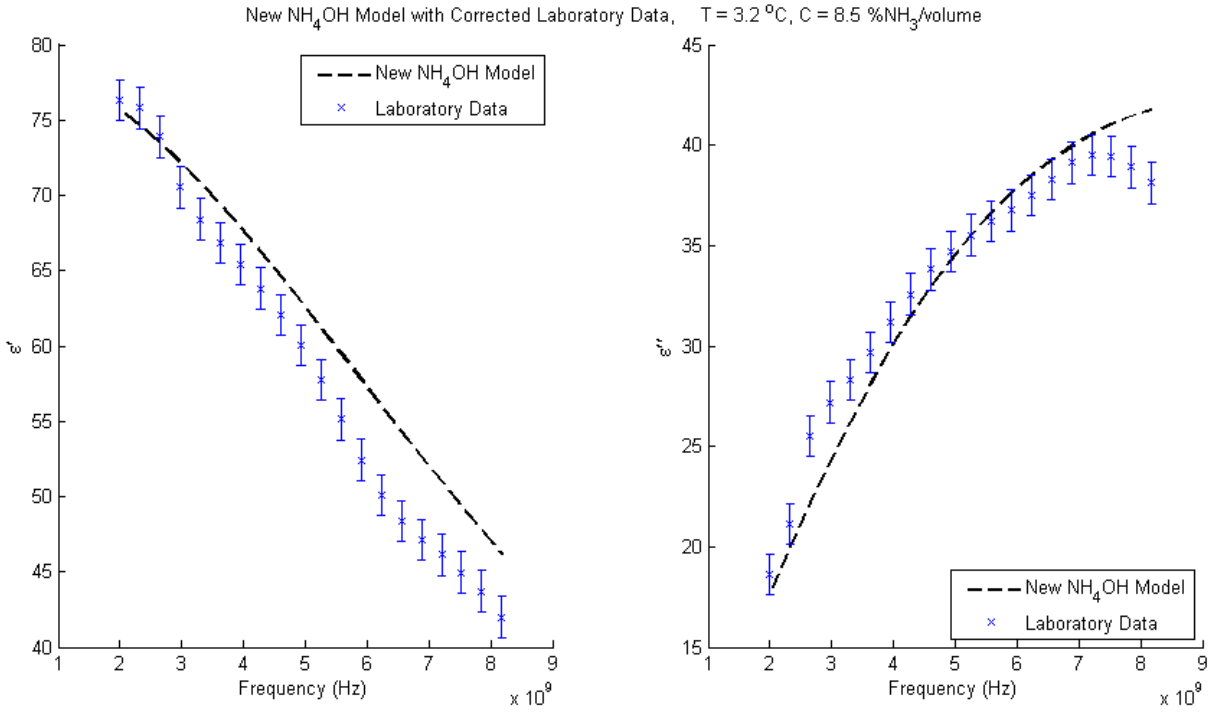

Figure 115. Laboratory data set 20 taken on 1/7/11 - 13:32 with new NH_4OH model.

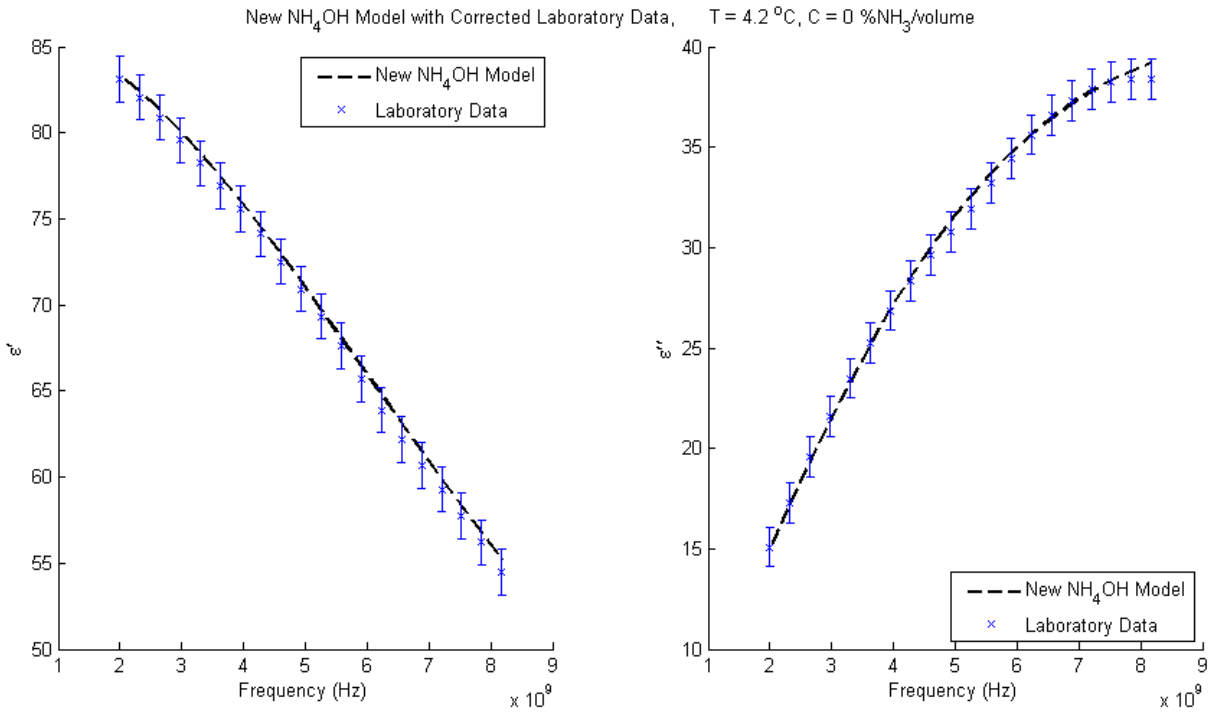

Figure 116. Laboratory data set 21 taken on 1/7/11 - 14:39 with new NH_4OH model.

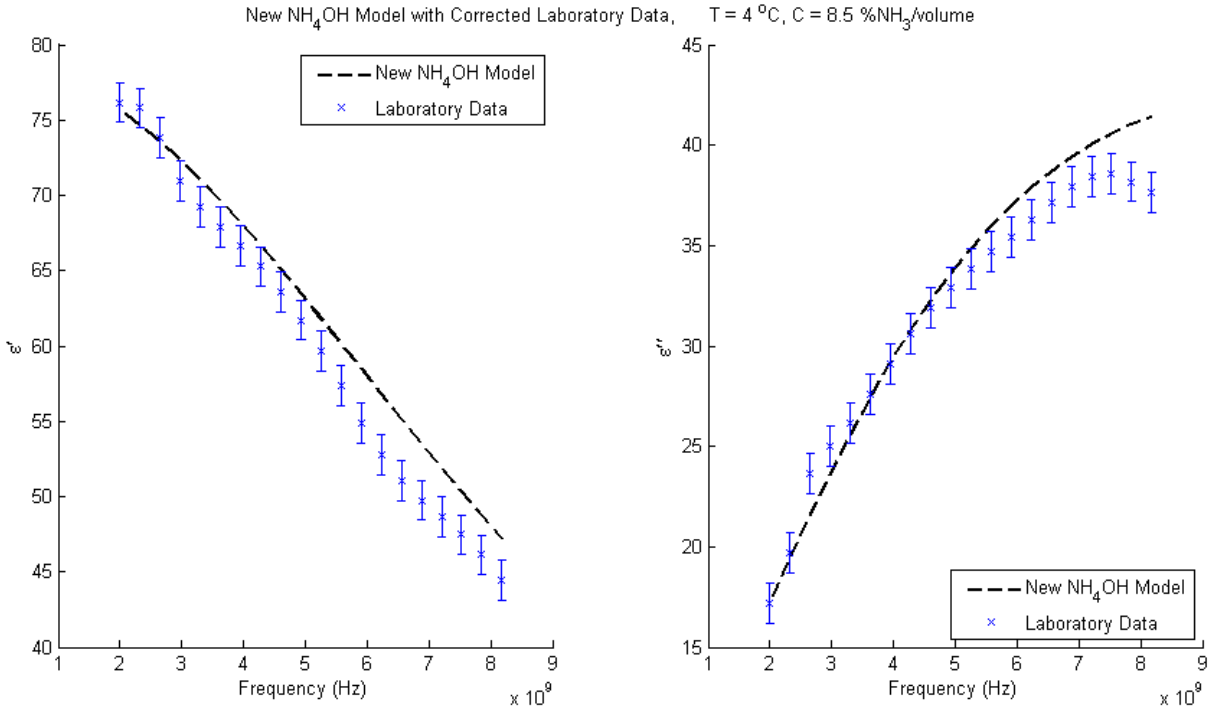

Figure 117. Laboratory data set 22 taken on 1/7/11 - 15:11 with new NH_4OH model.

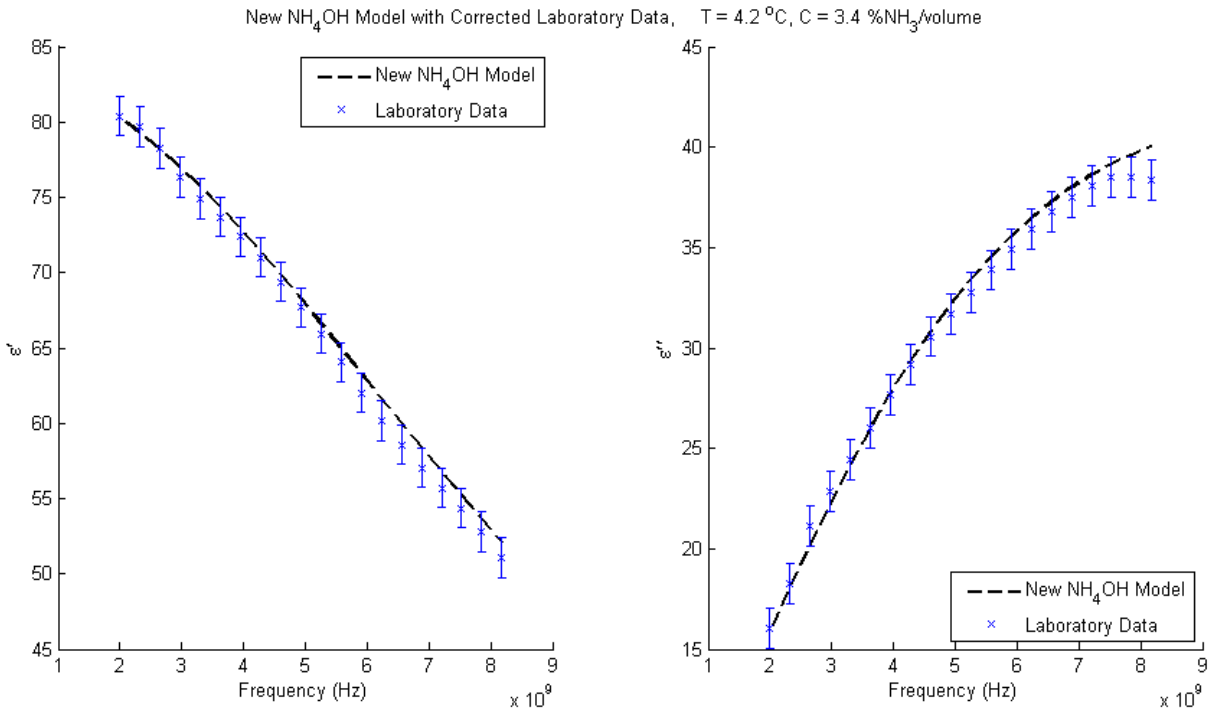

Figure 118. Laboratory data set 23 taken on 1/7/11 - 15:38 with new NH_4OH model.

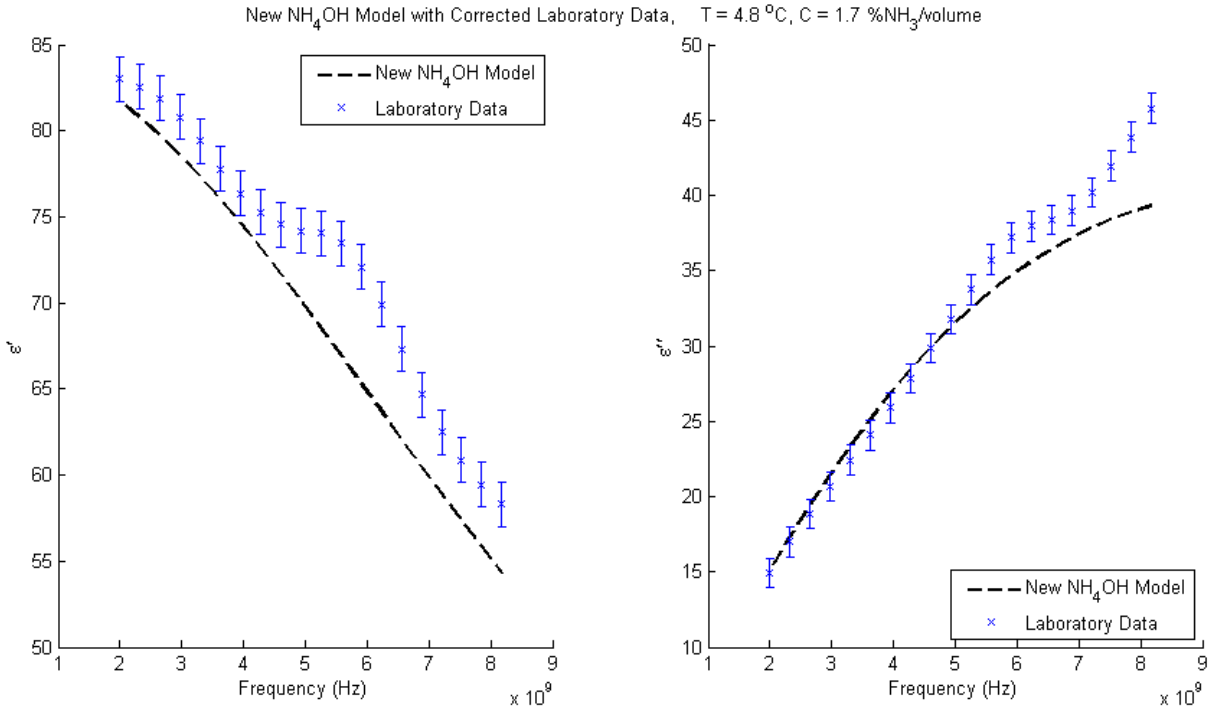

Figure 119. Laboratory data set 24 taken on 1/7/11 - 16:10 with new NH_4OH model.

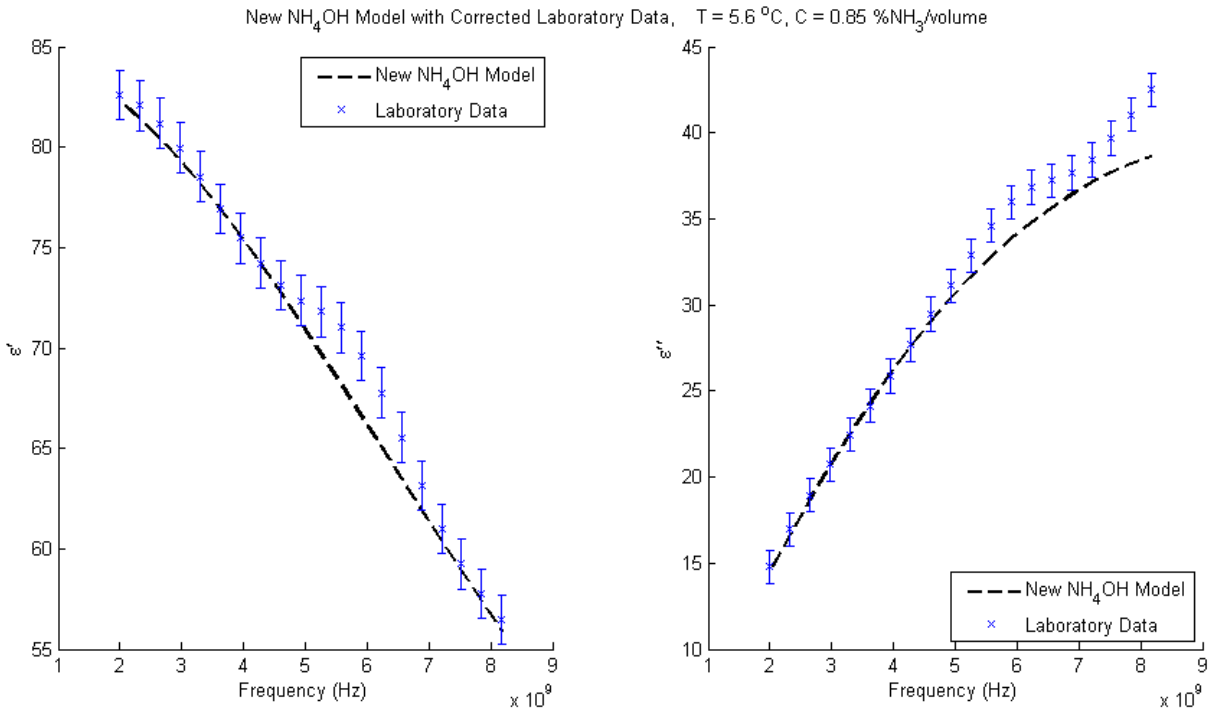

Figure 120. Laboratory data set 25 taken on 1/7/11 - 16:35 with new NH_4OH model.

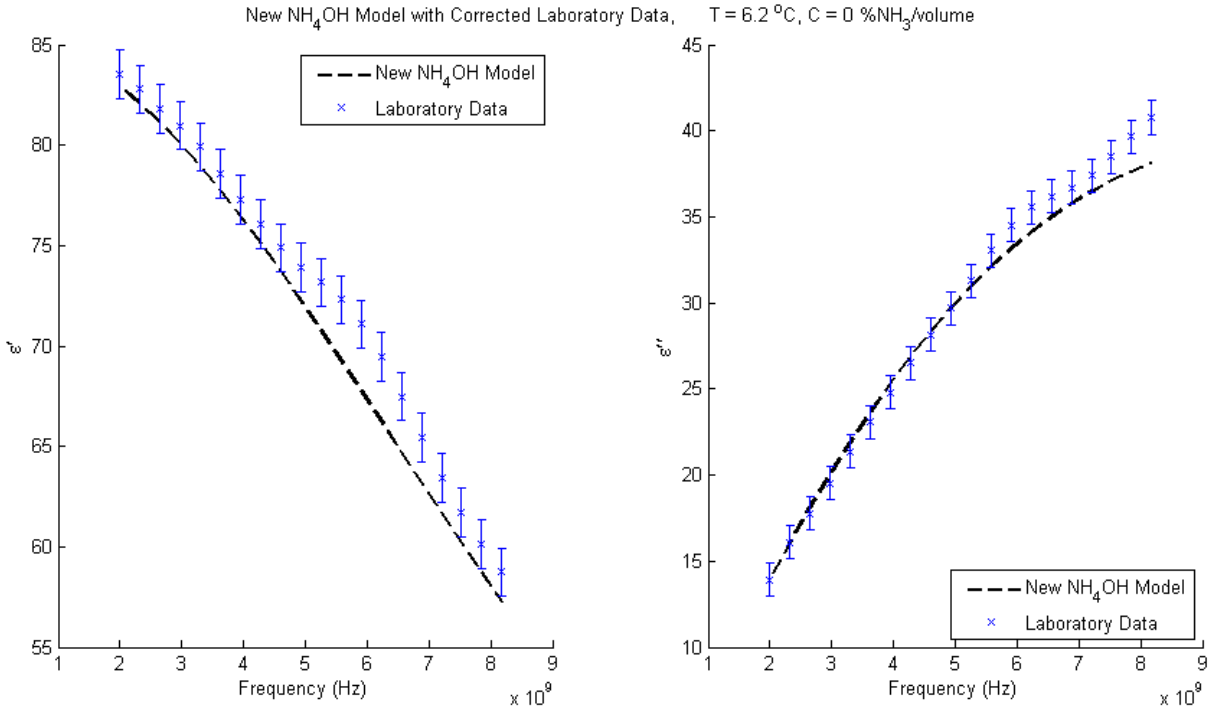

Figure 121. Laboratory data set 26 taken on 1/7/11 - 17:00 with new NH_4OH model.

References

Agilent Technologies (2006), "Agilent Basics of Measuring the Dielectric Properties of Materials", 85070E Application Note.

Battan, L. J. (1973), *Radar observation of the atmosphere*, University of Chicago Press, Chicago.

Budavari, S., M. J. O'Neil, A. Smith, *et al.* (1996). *The Merck Index*, 12th edition. Merck & Co., New Jersey.

Cole, K. S., and R. H. Cole (1941), Dispersion and absorption in dielectrics, *Journal of Chemical Physics, Vol. 9*, 341-351.

de Pater, I., D. DeBoer, M. Marley, R. Freedman, and R. Young (2005), Retrieval of water in Jupiter's deep atmosphere using microwave spectra of its brightness temperature, *Icarus, Vol. 173*, 425-447.

Debye, P. (1929), *Polar Molecules*, The Chemical Catalog Company, Inc., New York.

Devaraj, K., P. G. Steffes, and B. M. Karpowicz (2011), Reconciling the centimeter- and millimeter-wavelength ammonia absorption spectra under jovian conditions: Extensive millimeter-wavelength measurements and a consistent model. *Icarus*, *Vol. 212*, 224-235.

DeBoer, D. R., P. G. Steffes (1996), Estimates of the tropospheric vertical structure of Neptune based on microwave radiative transfer studies, *Icarus, Vol 123*, 324-335.

Fluke (2008), "62 Mini Infrared Thermometer" 62 Mini Infrared Thermometer Datasheet.

Gaiduk V. L. (1999), Dielectric Relaxation and Dynamics in Polar Molecules, *Contemporary Physics, Vol. 8.* World Scientific, London.

Guillou, C., *et al.* (1998), Impact of new permittivity measurements on sea surface emissivity modeling in microwaves, *Radio Science, Vol. 33,* 649-667.

Hanley, T. R. (2007), The microwave opacity of ammonia and water vapor; Application to remote sensing of the atmosphere of Jupiter, Ph.D. thesis, Georgia Institute of Technology.

Hayt, W., and J. Buck (2006), *Engineering Electromagnetics*, 8th edition. McGraw-Hill, New York.

W. W. Hines, D. C. Montgomery, D. Goldsman, and C. Borror (2003), *Probability and Statistics in Engineering*, 4th edition, John Wiley and Sons, New York.

Jacquemoud, S., and S. L. Ustin (2003), "Application of radiative transfer models to moisture content estimation and burned land mapping". *Joint European Association of Remote Sensing Laboratories (EARSeL) and GOFC/GOLD-Fire Program, 4th Workshop on Forest Fires*, University Ghent, Belgium 5—7, June 2003.

Janssen, M. A., M. D. Hofstadter, S. Gulkis, A. P. Ingersoll, M. Allison, S. J. Bolton, S. M. Levin, and L. W. Kamp (2005), Microwave remote sensing of Jupiter's atmosphere from an orbiting spacecraft, *Icarus, Vol. 173*, 477-453.

Karpowicz, B. M. (2010), In search of water vapor on Jupiter: Laboratory measurements of the microwave properties of water vapor and simulations of Jupiter's microwave emission in support of the Juno mission, Ph.D. thesis, Georgia Institute of Technology.

King, R. W. P. and G. S. Smith (1981), *Antennas in Matter: Fundamentals, Theory, and Applications*. MIT Press, Cambridge.

Kirkwood, J. G. (1939), The dielectric polarization of polar liquids, *Journal of Chemical Physics, Vol. 10*, 911.

Klein, L. A. and C. T. Swift (1977), An improved model for the dielectric constant of sea water at microwave frequencies. *IEEE J. Oceanic Eng., Vol. 2.* 104-111.

Lange, N. A. (1973), *Lange's Handbook of Chemistry*, 10th edition. McGraw-Hill, New York.

LeBlanc, J. R., S. Madhavan, and R. E. Porter (1978). Ammonia. *Kirk-Othmer encyclopedia of chemical technology*, 3rd edition. John Wiley & Sons, Inc., New York.

Levenberg, K. (1944), A method for the solution of certain nonlinear problems in least squares. *Quart. Appl. Math.*, Vol. 2, 164-168.

Liebe, H. J., G. A. Hufford, and T. Manabe (1991), A model for the complex permittivity of water at frequencies below 1 THz. *International Journal of Infrared and Millimeter Waves, Vol. 12*, 659-675.

Marquardt, D. (1963). An algorithm for least-squares estimation of nonlinear parameters. *SIAM J. Appl. Math.*, Vol. 11, 431-441.

Matousek, S. (2005). The Juno New Frontiers Mission, *IAC 2005 Conference*, IAC-05-A3.2A.04, Fukuoka, Japan.

Meissner, T., and F. J. Wentz (2004), The complex dielectric constant of pure and sea water from microwave satellite observations, *IEEE Transactions on Geoscience and Remote Sensing, Vol. 42*, 1836-1849.

Omega Engineering, Inc. (2007), "HH-21A, HH-22A, and HH-23A Handheld Microprocessor Thermometers," HH-23A Datasheet.

Omega Engineering, Inc. (2010), "PHH-103 pH/mV/temperature meter," PHH-103 Datasheet.

P. Pingree, *et al.* (2008), Microwave Radiometers from 0.6 to 22 GHz for Juno, A Polar Orbiter around Jupiter. *Proceedings of IEEE Aerospace Conference*, Big Sky, MT.

Ricca Chemical Company (2010), "Material Safety Data Sheet," Ammonium Hydroxide Aqueous Solutions, NH4OH Datasheet.

Stillman, D. (1978). *Galileo At Work*. University of Chicago Press, Chicago.

Wang, J. R. (2002), A comparison of the MIR-Estimated and Model-Calculated Fresh Water Surface Emissivities at 89, 150, and 220 GHz. *IEEE Transactions on Geoscience and Remote Sensing, Vol. 40,* 1356-1365.

Warren, S. G. (1984), Optical constants of ice from the ultraviolet to the microwave, *Applied Optics, Vol. 23*, 1206-1225.

Weast, R. C., and D. R. Lide (Eds.) (1989), *CRC Handbook of Chemistry and Physics*, CRC Press.

Wentz, F. J. (1997), A Well Calibrated Ocean Algorithm for Special Sensor Microwave/Imager, *Journal of Geophysical Research, Vol. 102,* 8703-8718.